# Hydrodynamic instabilities in long-term three-dimensional simulations of neutrino-driven supernovae of 13 red supergiant progenitors

Beatrice Giudici. 1\* Michael Gabler and Hans-Thomas Janka 2

<sup>1</sup>Departamento de Astronomía y Astrofísica, Universitat de València, E-46100 Burjassot (València), Spain

Accepted XXX. Received YYY; in original form ZZZ

#### ABSTRACT

We present long-term three-dimensional (3D) simulations of Type-IIP supernovae (SNe) for 13 non-rotating, single-star, redsupergiant (RSG) progenitors with zero-age-main-sequence masses between 12.5  $M_{\odot}$  and 27.3  $M_{\odot}$ . The explosions were modelled with a parametric treatment of neutrino heating to obtain defined energies, <sup>56</sup>Ni yields, and neutron-star properties in agreement with previous results. Our 3D SN models were evolved from core bounce until 10 days to study how the large-scale mixing of chemical elements depends on the progenitor structure. Rayleigh-Taylor instabilities (RTIs), which grow at the (C+O)/He and He/H interfaces and interact with the reverse shock forming after the SN shock has passed the He/H interface, play a crucial role in the outward mixing of <sup>56</sup>Ni into the hydrogen envelope. We find most extreme <sup>56</sup>Ni mixing and the highest maximum <sup>56</sup>Ni velocities in lower-mass (LM) explosions despite lower explosion energies, and the weakest <sup>56</sup>Ni mixing in the 3D explosions of the most massive RSGs. The efficiency of radial <sup>56</sup>Ni mixing anti-correlates linearly with the helium-core mass and correlates positively with the magnitude of a local maximum of  $\rho r^3$  in the helium shell. This maximum causes shock deceleration and therefore facilitates high growth factors of RTI at the (C+O)/He interface in the LM explosions. Therefore fast-moving <sup>56</sup>Ni created by the asymmetric neutrino-heating mechanism is carried into the ubiquitous RT-unstable region near the He/H interface and ultimately far into the envelopes of the exploding RSGs. Our correlations may aid improving mixing prescriptions in 1D SN models and deducing progenitor structures from observed SN properties.

**Key words:** supernovae: general – stars: massive – hydrodynamics – shock waves – instabilities – convection

# 1 INTRODUCTION

The detection of Supernova SN 1987A in the Large Magellanic Cloud (LMC) on February 23, 1987 marked a groundbreaking event in the history of astronomy. Until now, this core-collapse supernova (CCSN) and its remnant are among the most thoroughly studied objects in modern astrophysics, which reveal the evolution of a massive blue supergiant star from its pre-collapse state through the supernova (SN) explosion into the remnant stage of the gaseous ejecta in extraordinary detail (see e.g., Arnett et al. 1989a; Bethe 1990; McCray 2017; Podsiadlowski 2017). Meanwhile, a growing number of different kinds of observations clearly show the genuinely threedimensional (3D) character of this event (Sinnott et al. 2013; Utrobin et al. 2015; Larsson et al. 2016; Abellán et al. 2017; Alp et al. 2019; Cigan et al. 2019). A new breakthrough was marked by the advent of the James Webb Space Telescope (JWST), which allows observations with unprecedented resolution. Jones et al. (2023) were able to spatially resolve the ejecta, equatorial ring, and outer rings of SN 1987A in the mid-infrared, and Larsson et al. (2023) constructed the emissivity maps of the [Fe I] 1.443  $\mu$ m and [He I] 1.083  $\mu$ m lines. In particular, the [Fe I] line revealed a highly asymmetric morphology of the ejecta and the interaction of Fe-rich material with the reverse

\* E-mail: beatrice.giudici@uv.es

shock. Recently, Larsson et al. (2025) connected the 3D structure of SN 1987A's innermost ejecta with the possible location of the compact remnant. The remnant, which is most likely a neutron star (NS) (Page et al. 2020; Greco et al. 2021, 2022), seems to move towards the observer and to the north-east of the putative explosion centre according to the 3D [Fe I] 1.443  $\mu$ m line map of Larsson et al. (2023), but to the south-east according to the position of the JWST [Ar VI] source discussed by Fransson et al. (2024). The north-east direction would be consistent with conclusions drawn from the 679 GHz emission of a warm dust 'blob' observed with ALMA by Cigan et al. (2019).

Another well studied, young supernova remnant (SNR) is Cassiopeia A (Cas A), whose SN light reached the earth about 350 years ago (Fesen et al. 2006). This remnant is characterized by a reverse-shock heated shell enclosing the unshocked inner volume, a flattened ejecta distribution seen as a tilted thick disk, and two opposing wide-angle, jet-like ejecta structures (DeLaney et al. 2010). See also Isensee et al. (2010) for *Spitzer Space Telescope* infrared observations, Lazendic et al. (2006) for *Chandra X*-ray observations, and Fesen & Gunderson (1996); Fesen (2001) for optical observations, as well as the more recent, highly detailed infrared survey by JWST (Milisavljevic et al. 2024). Studies of such kind can reveal the geometrical distributions of chemical elements in the SN ejecta and have unfolded the morphologies not only of SN 1987A and Cas A,

<sup>&</sup>lt;sup>2</sup>Max-Planck-Institute for Astrophysics, Karl-Schwarzschild-Str. 1, 85748 Garching, Germany

but also of many other remnants of CCSNe (e.g., Aschenbach et al. 1995; Vink 2012, 2017; Holland-Ashford et al. 2017; Katsuda et al. 2018; Larsson et al. 2021; Mayer et al. 2022, 2023).

Time sequences of spectra during the light-curve evolution of SNe are also powerful observational probes of radial mixing, in particular of heavy elements from the innermost into the outermost layers of the exploding stars. The mixing of <sup>56</sup>Ni has important implications for the shapes of the light curves, for example the duration of the plateau (e.g. Nakar et al. 2016; Goldberg et al. 2019) and the shape of the light-curve maximum (e.g., Utrobin et al. 2019, 2021). A fast rise of the observed light curve is related to rapidly expanding <sup>56</sup>Nirich structures, while the width of the emission peak can be related to the total amount of <sup>56</sup>Ni present and when the matter becomes transparent. The shape of the light curve is thus directly related to the distribution of <sup>56</sup>Ni.

After the SN shock has been launched, it propagates through the outer shells of the progenitor, which consist of progressively lighter elements. As shown for a spherically symmetric blast-wave solution (Sedov 1959), the acceleration of the shock wave depends on variations of the density gradient. The shock accelerates where the density gradient is steeper than  $r^{-3}$  and decelerates otherwise. Strong acceleration (deceleration) usually occurs when the shock approaches (moves away from) composition interfaces, e.g. the (C+O)/He and He/H interfaces. This combination can lead to a (locally) positive pressure gradient, while the density gradient remains negative. Consequently, these layers are prone to the growth of Rayleigh-Taylor instability (RTI) (Chevalier 1976). This instability is seeded by asymmetries generated in the innermost part of the ejecta (Kifonidis et al. 2003) and it can cause large-scale radial mixing of heavy elements into the outer layers of the star. In addition, the lighter elements (mostly hydrogen) can be mixed inwards (Fryxell et al. 1991; Müller et al. 1991).

First long-term 2D and 3D simulations investigating the role of RTIs relied on an artificial initiation of the explosion either by a point-like thermal explosion (Arnett et al. 1989b; Hachisu et al. 1990, 1992, 1994; Yamada & Sato 1990; Fryxell et al. 1991; Müller et al. 1991; Herant & Benz 1991, 1992; Herant & Woosley 1994; Iwamoto et al. 1997; Nagataki et al. 1998; Kane et al. 2000), by piston-driven explosions (Hungerford et al. 2003, 2005; Joggerst et al. 2009, 2010a,b), or by injection of thermal and kinetic energy into a given location (Couch et al. 2009, 2011; Ono et al. 2013). As a next step, Ellinger et al. (2012, 2013) performed asymmetric explosions with artificially imposed, global, low-mode asymmetries.

On the theoretical-phenomenological side of SNR modelling, there has been remarkable success in reproducing observed morphological features of SN 1987A (Ono et al. 2020, 2024; Orlando et al. 2020; Nakamura et al. 2022) and of Cas A (Orlando et al. 2016) by relying on specifically defined initial conditions (partially even at shock breakout) with imposed explosion asphericities. Though matching some observations well, this kind of simulations cannot answer the question how the asymmetries are seeded and how they are linked to the SN mechanism. In particular, the growth of hydrodynamic instabilities in the phases preceding the shock breakout is not captured self-consistently.

In a parallel theoretical development, this shortcoming was overcome by long-term simulations where the SN explosion was initiated and powered by neutrino energy deposition in the innermost ejecta, based on the paradigm of the neutrino-driven explosion mechanism, where the stalled SN shock is revived by the interaction of neutrinos radiated by the hot proto-neutron star (PNS) with the still infalling matter of the collapsing stellar core (Colgate & White 1966; Arnett 1966; Bethe & Wilson 1985). Inspired by the radial mixing of core

material into the stellar envelope observed in SN 1987A, it was shown by multi-dimensional simulations that hydrodynamic instabilities develop in the neutrino-heated gain layer behind the stalled shock. Depending on the shock radius, strong convection (Bethe 1990; Herant & Benz 1992; Herant & Woosley 1994; Burrows et al. 1995; Janka & Müller 1995, 1996) and global mass motions by the standing accretion shock instability (SASI) (Foglizzo 2002; Blondin et al. 2003; Blondin & Mezzacappa 2006; Ohnishi et al. 2006; Foglizzo et al. 2007; Scheck et al. 2008; Fernández 2010; Buellet et al. 2023) can occur. Both push shock expansion and therefore increase the volume and mass in the gain layer, thus facilitating easier explosions because more matter in the post-shock region absorbs more energy from neutrinos. Moreover, the joint effect of these instabilities leads to non-radial flows and turbulent mass motions in the neutrino-heated gas and imposes large-scale asymmetries on the SN ejecta already at the onset of the explosion.

Based on the paradigm of the neutrino-driven mechanism, longterm simulations have achieved to connect the final ejecta asymmetries of CCSNe with these early ejecta asymmetries that emerged from the mentioned hydrodynamic instabilities during the neutrinoheating phase. The first such simulations that followed the SN evolution from the onset of the explosion until the breakout of the SN shock from the stellar surface and beyond were performed in 2D by Kifonidis et al. (2003, 2006), who initiated the neutrino-driven blast by a parametric prescription ("light bulb" or neutrino "engine") of the neutrino luminosities that accomplished the energy deposition in the gain layer. Meanwhile, a larger number of 3D simulations of this kind has been performed, including explosions of red supergiant (RSG) and blue supergiant (BSG) progenitors of Type-IIP SNe and of stripped progenitors of Type-IIb and Ib/c SNe (Hammer et al. 2010; Wongwathanarat et al. 2013, 2015, 2017; Utrobin et al. 2015, 2017, 2019, 2021; van Baal et al. 2023, 2024). Some of these simulations have even been continued into the early evolution of the SNRs for hundreds of days up to hundreds of years (Gabler et al. 2021; Orlando et al. 2021, 2022).

Although the shock revival phase by neutrino heating can now be simulated fully self-consistently in 3D (e.g., Kuroda et al. 2012; Takiwaki et al. 2014; Melson et al. 2015a,b; Lentz et al. 2015; Müller et al. 2017, 2019; Burrows et al. 2019; Powell & Müller 2019, 2020; Bollig et al. 2021; Vartanyan et al. 2022; Burrows et al. 2024b; Janka & Kresse 2024; Nakamura et al. 2025), these simulations involve (more or less) elaborate and time consuming treatments of the neutrino transport. Therefore they usually cover periods of at most the first seconds after core bounce with few exceptions where the evolution was followed until shock breakout for ultrastripped progenitors (Müller et al. 2018) and a small sample of RSG progenitors (Stockinger et al. 2020; Sandoval et al. 2021; Vartanyan et al. 2025a,b). Simulations with a rigorous treatment of the neutrino physics over such long periods of time for larger sets of models are still prohibitive because of their enormous demands of computing resources. Only recently, in a study parallel to ours, Vartanyan et al. (2025b) presented a small set of such 3D simulations that were continued into the long-time evolution beyond shock breakout for SNe originating from RSG progenitors.

In our project we will proceed along the lines of the 3D CCSN modelling with neutrino engine-driven explosions mentioned above. In order to reduce the computing time requirements for the complex neutrino physics and transport in the newly formed PNS, the high-density core of the PNS with a neutrino optical depth of more than 10–100 is replaced by a moving inner grid boundary, which mimics the contraction of the cooling compact remnant. At this inner boundary the neutrino luminosities radiated by the PNS are pre-

scribed parametrically such that the explosion energy can be tuned to a chosen value.

In the near-surface layers of the PNS and the neutrino-heating layer behind the SN shock the neutrino-transport equations and neutrino-matter interactions are solved with a grey ray-by-ray approximation (Scheck et al. 2006; Arcones et al. 2007). This approach allows us to perform a larger suite of 3D simulations that capture the fundamental aspects of neutrino-driven explosions and that follow long evolution times with acceptable computational costs. Thus we can investigate a set of 13 RSG progenitors and study how the hydrodynamic instabilities of the shock revival phase act later as seeds of the RTIs at the composition-shell interfaces after the passage of the outward propagating SN shock. This interplay of early and subsequent instabilities is essential to determine the final morphology of the explosion and the large-scale radial mixing of the ejecta, which shape many observational properties of SNe and young SNRs.

The manuscript is organized as follows: In Section 2, we briefly describe the pre-supernova (preSN) models, the numerical methods, and the input physics employed in our simulations. In Section 3 the results for the early phase of the SN explosions up to 2.5 s after core bounce are presented with a focus on the explosion energies, nickel yields, and PNS properties. In Section 4, we discuss the results of our 3D simulations for the evolution until 10 days after shock revival, considering a linear stability analysis for RTIs in 1D models, the radial mixing of the ejecta in 3D, the changes of the 3D morphologies of our models until 10 d, and the asymmetric shock breakout in our 3D RSG explosions. We also generalize a framework developed by Utrobin et al. (2019, 2021) to quantify and characterize the radial <sup>56</sup>Ni mixing in a larger set of BSG explosions to our RSG explosions, and we correlate the degree of mixing with characteristic parameters of the explosion and information obtained from the 1D stability analysis. In Section 5, we go one step further and establish correlations between the extent of the radial <sup>56</sup>Ni mixing and the structure of the progenitor star. Our findings are summarized in Section 6.

# 2 MODEL OVERVIEW AND NUMERICAL SETUP

We investigate the explosion of 13 RSG progenitor models that were generated with the stellar evolution code Kepler (Weaver et al. 1978). These models have been discussed in detail previously (Sukhbold & Woosley 2014; Sukhbold et al. 2016). Therefore, we will summarize their main properties briefly in Section 2.1. In Section 2.2, we describe the Prometheus-Hotb code, which we employ to evolve these models after spherical collapse from the bounce in full 3D. Further details of the setup of the simulations are then given in Section 2.3

# 2.1 Progenitor models

All stellar models are non-rotating stars of solar metallicity and were evolved from the main sequence until the onset of the Fe-core collapse in a self-consistent manner (Sukhbold & Woosley 2014; Woosley & Heger 2015). The calculations included the entire stars with their hydrogen envelopes, using a mass loss prescription (Nieuwenhuijzen & de Jager 1990; Wellstein & Langer 1999; Woosley et al. 2002) and considering a rate of  $^{12}C(\alpha, \gamma)^{16}O$  equal to 1.2 times that of Buchmann (1996), S(300keV) = 146 keVb.

A simple parameter, introduced to characterize the 1D core structure of the pre-collapse star, is given by the compactness (O'Connor

Model	<b>Ĕ</b> 2.5	$R_{ m prog}$ [R $_{\odot}$ ]	$M_{\mathrm{prog}}$ $[\mathrm{M}_{\odot}]$	$M_{ m He}^{ m core}$ $[{ m M}_{\odot}]$	$M_{\mathrm{C+O}}^{\mathrm{core}}$ $[\mathrm{M}_{\odot}]$
		. 0,	. 0,	. 01	. 01
WH12.5	0.039	683.60	11.12	3.36	2.28
SW13.1	0.071	734.85	11.47	3.67	2.53
SW14.2	0.130	788.03	12.32	4.04	2.84
SW16.3	0.161	875.86	13.86	4.82	3.57
SW18.2	0.186	989.20	15.02	5.57	4.27
SW19.8	0.128	1058.01	15.85	6.24	4.88
SW20.8	0.161	1107.33	16.02	6.68	5.30
SW21.0	0.139	1124.55	16.12	6.76	5.37
SW25.5	0.250	1413.83	15.45	8.58	7.21
SW25.6	0.217	1428.27	15.60	8.64	7.28
SW26.2	0.243	1458.76	15.40	8.88	7.51
SW27.0	0.244	1508.21	15.40	9.26	7.92
SW27.3	0.249	1511.77	15.07	9.35	7.99

**Table 1.** Properties of the preSN models. The first column contains the name of the models, where the first two letters indicate the source of the model, WH for Woosley & Heger (2015) and SW for Sukhbold & Woosley (2014), and the number defines the ZAMS mass in solar masses. The second column shows the compactness  $\xi_{2.5}$  as defined in O'Connor & Ott (2011) and equation (1). Columns 3 and 4 contain the radius and the mass of the preSN star, respectively. In columns 5 and 6 we list the He and C+O core masses, measured at the locations where the hydrogen and helium mass fractions, respectively, drop below 50% of their maximum values.

#### & Ott 2011):

$$\xi_M = \frac{M/M_{\odot}}{R(M)/1000 \,\mathrm{km}} \bigg|_{t_{homoso}}$$
 (1)

These authors found that with a higher compactness, the star is less likely to explode. However, this simple criterion turned out not to be perfectly conclusive (e.g., Ugliano et al. 2012; Müller et al. 2016; Ertl et al. 2016; Sukhbold et al. 2016; Ertl et al. 2020), and it is in tension with some of the most recent self-consistent multi-dimensional CCSN simulations as well as 1D explosion modelling that includes post-shock turbulence in a parametrized mixing-length-like treatment (e.g. Wang et al. 2022; Boccioli et al. 2025).

There are substantial differences in the stellar structure between models with masses below  $20\,M_\odot$  and those above that value. The compactness parameter of equation (1), which is an indication of the density structure of the core, increases rapidly in the range of  $12-15\,M_\odot$  and then it remains roughly constant until  $\sim 20\,M_\odot$ . In stellar models with masses of up to about  $20\,M_\odot$ , carbon ignites exoergically and powers convection, creating highly variable preSN core structures (Sukhbold & Woosley 2014).

The stars with masses between 20 and  $30\,M_\odot$ , on the contrary, ignite carbon burning endoergically, thus they are not convective because entropy is radiated away by neutrinos. These more massive models develop extended and dense shells that undergo rapid and intense shell burning. As a result of their more evolved and massive cores, these stars tend to have a higher compactness than lower-mass models.

The ZAMS masses of the preSN models analysed in this paper are in the range between  $12\,M_\odot$  and  $30\,M_\odot$ . The selected models and their basic properties are listed in Table 1. The locations of the (C+O)/He and He/H composition interfaces are defined as the positions at the bottom of the helium and hydrogen layers of the star where the He and H mass fractions, respectively, drop below half of the maximum value in the respective cell (Wongwathanarat et al. 2015). Note, that this is different from the 20% threshold taken in Sukhbold et al. (2016). The difference is minor and affects the C+O

core masses in Table 1 only in the second digit and the He core masses at most on the level of  $\sim 0.1 M_{\odot}$ .

In Fig. 1, we display the density profiles of all the progenitor models analysed in this paper just after core bounce as functions of radius (left) and enclosed mass (right).

In order to perform a larger number of 3D simulations that follow the explosions from core bounce until well after shock breakout with reasonable computational resources, we rely in our treatment of neutrino effects on the approximate neutrino transport scheme of Scheck et al. (2008) and Wongwathanarat et al. (2013) as detailed in the next section. Within this approach, we have the freedom to tune the explosion energy and the timescale for significant neutrino energy deposition by parameters. For our 3D models we chose explosion energies comparable to those obtained by Sukhbold et al. (2016) and Ertl et al. (2020) in their large sets of 1D models. Those models were exploded with a similar, parametric neutrino-engine treatment including the same ray-by-ray description of neutrino transport.

#### 2.2 Numerical setup

We performed the simulations with the code Prometheus (Fryxell et al. 1991; Müller et al. 1991) in its version Proметнеиs-HoтВ (Janka & Müller 1996; Kifonidis et al. 2003, 2006; Scheck et al. 2006; Arcones et al. 2007; Wongwathanarat et al. 2013, 2015, 2017; Gessner & Janka 2018; Stockinger et al. 2020; Gabler et al. 2021). The code is a 3D, explicit finite-volume hydrodynamics scheme that includes a simplified neutrino radiation module, an equation of state (EOS) covering high and low densities including nuclear statistical equilibrium (NSE), and a description of nuclear burning in the form of an  $\alpha$  network when NSE does not apply. The equations of hydrodynamics are solved with the piecewise parabolic method (PPM) (Colella & Woodward 1984) employing the exact Riemann solver for real gases of Colella & Glaz (1985). Different species are evolved via the consistent multifluid advection (CMA) scheme (Plewa & Müller 1999). Inside the grid cells where strong shocks are present, either the Harten-Lax-van Leer-Einfeldt (HLLE) (Einfeldt 1988) or the improved advection upstream splitting method (AUSM+) (Liou 1996) solver are employed in order to suppress numerical artifacts that can arise due to odd-even decoupling. Until shock breakout, we usually use the AUSM+ solver with a static grid. Only later, when following the expanding ejecta with a quasi-Lagrangian computational grid (Gabler et al. 2021), the more diffusive HLLE solver is used to avoid problems with numerical stability.

The computational domain is discretized by means of an axis-free overlapping Yin-Yang grid technique (Kageyama & Sato 2004) implemented into Prometheus-HotB by Wongwathanarat et al. (2010). The Yin-Yang approach avoids numerical artifacts that can arise near the polar axis in a standard spherical grid. It also alleviates the time-step constraints imposed by the Courant-Friedrich-Levy (CFL) condition, which is very restrictive for a spherical polar grid due to the small azimuthal grid step size near the axis. Thus, the Yin-Yang grid allows for larger time steps in the simulations and, hence, for computationally less expensive long-time simulations.

Since we are only interested in the matter that is ejected during the SN explosion but not in the detailed evolution of the PNS, where the CFL limit is particularly small, the computational efficiency of our simulations is further increased by excluding a time-dependent spherical volume around the coordinate centre from the computational grid. This central region is replaced by an inner grid boundary. For the first 2.5 s after core bounce the excised domain contains the high-density core of the PNS and at later times a larger central volume (for details, see below).

Newtonian self-gravity is taken into account by solving the integral form of Poisson's equation with a multipole expansion method optimized for parallel computations (Müller & Steinmetz 1995; Wongwathanarat 2019). The central mass that is not included on our computational grid is taken into account as a point mass in the gravity solver. We also apply general relativistic corrections to the monopole of the potential following Scheck et al. (2006) and Arcones et al. (2007).

During the first 2.5 s we handle neutrino effects by an approximate grey transport treatment based on an analytic solution of the Boltzmann equations for neutrino number density and energy density with a ray-by-ray approach for multi-dimensional simulations. For the basic equations, numerical treatment and input concerning the neutrino rates see Scheck et al. (2006). During this early phase the high-density core of the PNS (up to  $\sim 1.1 \,\mathrm{M}_{\odot}$ ), where the neutrino optical depth typically exceeds 10–100, is excised from the computational domain and replaced by a closed inner grid boundary at radius  $R_{\rm ib}$ . This  $R_{\rm ib}$  is contracted to mimic the shrinking of the new-born PNS due to cooling and deleptonization by neutrino emission. At this inner boundary neutrino luminosities are imposed with a functional behaviour and parameter values given in Section 2.3 and with spectral properties according to local thermal equilibrium with the stellar plasma in the innermost radial grid zone.

Initially, the inner boundary is placed at a radius of  $R_{\rm ib} \gtrsim 60$  km. The first 25 zones in radial direction are equispaced with a  $\Delta r/r \approx$ 0.01, and farther out the distance between radial grid points increases logarithmically. We use a total number of 400 radial grid points. The outer boundary of the radial grid at  $R_{\rm ob} = 4 \times 10^5$  km is treated as an outflow boundary. The final radius of the inner grid boundary after  $2.5 \,\mathrm{s}$  is  $\approx 20 \,\mathrm{km}$ . The angular part of the computational grid covers the entire  $4\pi$  solid angle with the constant resolution of  $\Delta\theta = \Delta\phi = 2^{\circ}$ in both angular directions. In each Yin and Yang patch, we thus have 45 zones in  $\theta$ -direction and 135 zones in  $\phi$ -direction.

We follow the shock-revival phase and shock propagation on this grid until  $t_{\text{map}} = 2.5 \text{ s}$  after bounce. At this point the simulation is remapped to a larger radial domain in order to track the propagation of the explosion shock through the outer stellar layers. The new boundaries are chosen at  $R_{\rm ib} = 500 \, \rm km$  and twice the progenitor radius  $R_{\rm ob} \approx 2 \times R_{\rm prog}$ . The radial grid now contains 1200 points initially and is again logarithmically spaced with the innermost cell having a size of  $\Delta r = 2.5$  km. The angular grid remains unchanged. At this time we describe the inner boundary as an inflow boundary where a neutrino-driven wind is imposed with a functional behaviour and parameters provided in Section 2.3.

During the subsequent long-term simulations, we remove the innermost radial zone whenever  $R_{\rm ib}$  becomes smaller than 1% of the minimum radius of the aspherical SN shock, or when the material in every cell of the innermost layer is falling inward with velocities greater than the speed of sound in the respective cell. This progressively reduces the number of radial grid zones, thus speeding up the simulations. The mass of the excised zones is added to the central

The flow through the inner boundary after the neutrino-driven wind ceases and, to a lesser extent, the successive cutting out of the innermost cells can cause some of the matter to leave our numerical grid. In the most extreme cases (the most massive progenitors) this may add up to the order of one  $M_{\odot}$  which is removed from our simulations. We cannot strictly determine what the fate of this mass will be. It may be accreted to the central NS, possibly causing the formation of a black hole in our simulations, or it may get reaccelerated outwards. However, this "fallback" could be a feature of our parametrized explosion set up and more realistic engine simu-

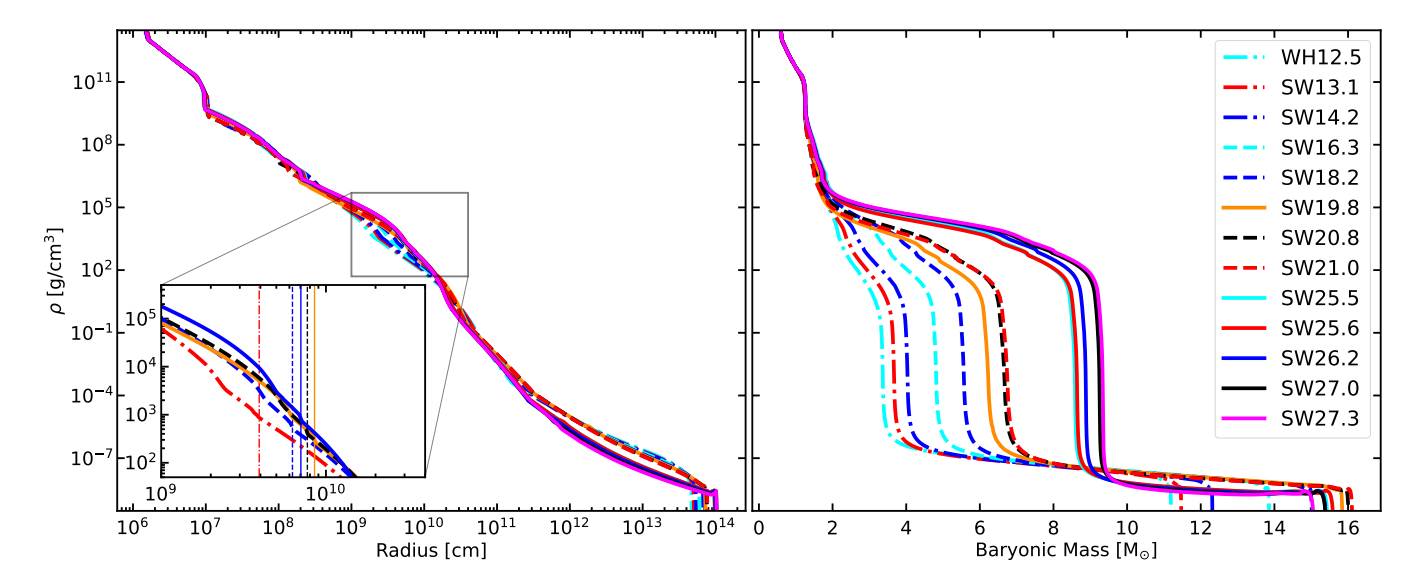


Figure 1. Density profiles as functions of radius (left) and enclosed baryonic mass (right) for all of the considered SN models roughly some 10 ms after core bounce when the shock has reached a radius of  $\sim$ 100 km and an enclosed mass of  $\sim$ 1.3  $M_{\odot}$ . The vertical lines in the inset depict the location of the (C+O)/He composition interface for a selected set of models.

lations may provide a more robust description of the slowest ejecta. Furthermore, we are not interested in what happens to the innermost ejecta, since these are not expected to be prone to RTI.

Once the shock leaves the surface of the progenitor, the grid is moved radially as the SN ejecta expands. This moving mesh relaxes the CFL condition more and more and reduces numerical diffusion through cell boundaries. The grid velocity is set to be linearly proportional to the radius. Depending on the model, the outermost grid cell moves with at most 150% of the maximum fluid velocity, whereas the velocity of the innermost radial grid cell is always set to zero. Between these maximal radial extents, the mesh velocity increases linearly. In some cases, the shock may still expand faster than the such determined maximum grid velocity. To avoid the shock leaving the computational domain during the simulation, we add a new cell to the outer boundary whenever the shock gets closer than 20 cells to the outer boundary of the computational grid (Gabler et al. 2021). At the same time we remove the innermost radial cell to keep the total number of cells constant.

By the end of the simulations, at 10 days after the explosion, the radial grid contains between 400 and 500 zones depending on the model. The ratio of  $\Delta r/R$  is usually of the order of 0.01, and always smaller than 0.05.

# 2.3 Input physics

We performed our simulations with the tabulated EOS LS220 for high densities,  $\rho > 10^{11}\,\mathrm{g}\cdot\mathrm{cm}^{-3}$  (Lattimer & Swesty 1991), and a tabulated EOS by Timmes & Swesty (2000) based on the Helmholtz free energy for intermediate densities. The latter considers arbitrarily degenerate and relativistic Fermi gases for electrons and positrons, photons, and ideal Boltzmann gases for the baryonic matter, taking into account 19 nuclear species: protons, the 13  $\alpha$ -nuclei from  $^4$ He to  $^{56}$ Ni, the beta decay products of  $^{56}$ Ni and  $^{44}$ Ti ( $^{56}$ Co,  $^{56}$ Fe,  $^{44}$ Sc,  $^{44}$ Ca), and a tracer element  $^{56}$ X to represent the production of neutron-rich nuclear species when the electron fraction is  $Y_e < 0.49$ . These nuclei are treated as a mixture of ideal Boltzmann gases that are advected with the flow and can evolve due to nuclear reactions

described by an  $\alpha$ -chain reaction network (Kifonidis et al. 2003; Wongwathanarat et al. 2013) at temperatures  $T < 8 \cdot 10^9$  K, where we assume NSE not to hold.

When the density (temperature) in a zone drops below  $10^{-10} \,\mathrm{g\cdot cm^{-3}}$  ( $10^4 \,\mathrm{K}$ ), which is the lowest value given in the EOS table of Timmes & Swesty (2000), we switch to a simpler EOS taking into account only a set of ideal Boltzmann gases and blackbody radiation. The pressure p and the internal energy e per unit mass are given by

$$p = \frac{1}{3}aT^4 + \frac{k_B}{\mu m_H}\rho T,$$
 (2)

$$e = \frac{aT^4}{\rho} + \frac{3}{2} \frac{k_B}{\mu m_H} T,\tag{3}$$

where a is the radiation constant,  $\rho$  is the density, T is the temperature,  $k_{\rm B}$  is Boltzmann's constant,  $\mu$  is the mean molecular weight, and  $m_{\rm H}$  is the atomic mass unit.

For the early stages of the explosion, when neutrinos are treated by the grey ray-by-ray approximation of Scheck et al. (2006), we follow Wongwathanarat et al. (2013, 2015) in the parametrization of the neutrino luminosities and mean energies imposed at the inner grid boundary. The luminosities  $L_0^{\rm tot}$  are set to remain constant during 1 s and then to decay exponentially with a timescale of 1 s. Their initial values are specified such that our simulations reproduce roughly the 1D explosion energies reported by Sukhbold et al. (2016) and are given in Table 2.

After remapping our simulations at  $t_{\rm map} = 2.5$  s, we account for the ongoing neutrino energy deposition into the ejecta in terms of a neutrino-driven wind. The latter is described as an exponentially decaying, spherically symmetric baryonic mass flow injected through the inner grid boundary with a constant velocity  $v_{\rm w}$  (Wongwathanarat et al. 2015). The time-dependent density  $\rho_{\rm w}(t)$ , specific internal

Model Class	Properties	Reference Model	Model Name	$L_0^{\text{tot}}$ [B s <sup>-1</sup> ]	E <sub>exp</sub> [B]	E <sub>exp</sub> [B]	t <sub>exp</sub> [ms]	$M_{ m NiCoFe0.5X}$ $[{ m M}_{\odot}]$	$M_{ m PNS}$ $[{ m M}_{\odot}]$	v <sub>PNS</sub> [km s <sup>-1</sup> ]	$J_{\rm PNS}$ [10 <sup>46</sup> g cm <sup>2</sup> s <sup>-1</sup> ]	$lpha_{ m sk}$ [°]	T <sub>spin</sub> [s]
LM	Low $M_{ m ZAMS}$	SW13.1	WH12.5 SW13.1 SW14.2	111 108 128	0.74 0.68 0.78	0.70 0.69 0.76	346 358 407	0.061 0.059 0.066	1.40 1.43 1.52	287.54 258.87 632.57	4.27 6.24 6.41	86.5 127.5 37.7	0.23 0.16 0.17
HM-LE	$E_{ m exp}^{ m 3D}$ High $M_{ m ZAMS}$	SW18.2	SW16.3 SW18.2 SW20.8 SW21.0	117 140 133 114	1.15 1.24 0.83 1.13	1.26 1.25 0.83 1.01	215 344 382 201	0.097 0.107 0.076 0.093	1.35 1.59 1.47 1.35	311.67 499.02 680.60 109.13	4.54 10.30 9.09 5.19	126.7 93.3 49.7 113.7	0.21 0.11 0.12 0.19
НМ-НЕ	$E_{ m exp}^{ m 3D}$ High $M_{ m ZAMS}$	SW26.2	SW19.8 SW25.5 SW25.6 SW26.2 SW27.0 SW27.3	131 131 132 112 125 119	1.67 1.30 1.28 1.28 1.26 1.44	1.73 1.45 1.31 1.23 1.42 1.41	209 274 270 245 233 240	0.077 0.107 0.097 0.100 0.110 0.109	1.36 1.60 1.56 1.53 1.46 1.48	58.25 84.64 395.55 216.34 348.20 618.51	7.34 9.29 0.32 2.63 7.92 14.42	103.9 74.3 78.4 45.0 129.7 45.2	0.13 0.12 3.50 0.42 0.13 0.07

Table 2. Properties of the explosions and of the PNSs in the 3D models at  $t_{\text{map}} = 2.5$  s as defined in Section 3.  $L_0^{\text{tot}}$  is the assumed total initial neutrino luminosity at the inner grid boundary, distributed as 25% for  $v_e$ , 15% for  $\bar{v}_e$ , and 60% for  $v_x$ , where  $v_x$  represents the combined contributions from all heavy-lepton neutrino species.  $E_{\text{exp}}^{\text{1D}}$  is the explosion energy in the corresponding 1D models.  $E_{\text{exp}}^{3D}$  and  $t_{\text{exp}}$  are the explosion energy and time in 3D.  $M_{\text{NiCoFe0.5X}}$  is our best estimate for the total yield of  $^{56}\text{Ni}$  computed as the sum of the mass produced by the alpha network as  $^{56}\text{Ni}$  plus half of the mass created as tracer species  $^{56}\text{X}$ .  $M_{\text{PNS}}$  is the baryonic PNS mass in  $M_{\odot}$ .  $v_{\text{PNS}}$  is the hydrodynamic kick velocity of the PNS.  $J_{\text{PNS}}$  is the angular momentum of the PNS.  $\alpha_{\text{sk}}$  is the angle obtained between the direction of  $v_{\text{PNS}}$  and  $J_{\text{PNS}}$ .  $T_{\text{spin}}$  is the spin period of the final NS, calculated by considering the NS as a homogeneous sphere of mass  $M_{\text{PNS}}$  and radius 12 km with angular momentum  $J_{\text{PNS}}$ .

energy  $e_{\rm w}(t)$ , and pressure  $p_{\rm w}(t)$  are given by

$$\rho_{\rm w}(t) = \rho_{\rm w}(t_{\rm map}) \left(\frac{t}{t_{\rm map}}\right)^{-7/2},\tag{4}$$

$$e_{\rm w}(t) = e_{\rm w}(t_{\rm map}) \left(\frac{t}{t_{\rm map}}\right)^{-7/6},$$
 (5)

and

$$p_{\rm w}(t) = \frac{1}{3}e_{\rm w}(t)\rho_{\rm w}(t).$$
 (6)

The choice of the power-law indices in equations (4) and (5) is motivated by extrapolation of the density and internal energy evolution at  $r = 500 \, \mathrm{km}$ . This neutrino-wind boundary condition is applied until fallback sets in and the matter in the innermost radial zone moves inward in all cells. At this point, the inner boundary treatment is switched to a free outflow condition.

Outside of the progenitor at  $r > R_{prog}$  we consider a spherically symmetric, circumstellar medium (CSM) given by

$$\rho_{\rm e}(r) = \max \left\{ 10^{-12} \,\mathrm{g \, cm^{-3}} \left( \frac{R_{\rm prog}}{r} \right)^4, \, \rho_0 \left( \frac{1000 \, R_{\odot}}{r} \right)^2, \right.$$

$$10^{-25} \,\mathrm{g \, cm^{-3}} \right\}, \tag{7}$$

where  $\rho_0=1.46\times 10^{-13}~\rm g\cdot cm^{-3}$  for model WH12.5, and  $\rho_0=1.14\times 10^{-15}~\rm g\cdot cm^{-3}$  for the other models. The same values were used in Sukhbold et al. (2016). We have introduced the first term with the  $r^{-4}$  dependence to avoid numerical problems at too steep density gradients at the stellar surface. For typical wind velocities of 20 km s<sup>-1</sup>, these values correspond to mass-loss rates of  $2.82\times 10^{-4}~\rm M_{\odot}yr^{-1}$  and  $2.19\times 10^{-6}~\rm M_{\odot}yr^{-1}$ , respectively. In the simulations we neglect the small velocities of the stellar wind in the boundary conditions and set the velocity of the CSM to zero.

The temperature of the surrounding medium is chosen to have a

constant temperature of  $T_e = 1.0 \text{ K}$  for model WH12.5, whereas it is given by the relation

$$T_{\rm e}(r) = T_0 \left(\frac{R_{\rm prog}}{r}\right)^3,\tag{8}$$

with  $T_0 = 275 \,\mathrm{K}$  for the other models. These conditions are not realistic for stellar winds of RSGs. But since we are only interested in the ejecta asymmetries and mixing instabilities inside the exploding stars, the detailed conditions in the CSM do not matter for our simulations. The gas is placed around the stars mainly for numerical reasons to permit us extending our simulations beyond the point of shock breakout from the stellar surface. Furthermore, as long as the CSM density remains sufficiently low, its specific structure does not significantly affect the simulation results for timescales up to 1 year. In contrast, higher CSM densities can lead to stronger deceleration of the ejecta that catch up with the forward shock, potentially resulting in more pronounced Rayleigh-Taylor mushroom-like structures. To minimize the impact of the chosen CSM configuration on our results and to focus on the effects of the stellar structure on the RTIs, we adopt a low-density environment.

As is Stockinger et al. (2020) and Gabler et al. (2021), we allow for radioactive  $\beta$  decay of <sup>56</sup>Ni through <sup>56</sup>Co to <sup>56</sup>Fe. The released decay energy is taken into account as described in Gabler et al. (2021) and causes additional heating of the <sup>56</sup>Ni-rich ejecta. In addition to the decay chain of <sup>56</sup>Ni, the radioactive decay of <sup>44</sup>Ti to <sup>44</sup>Sc and then to <sup>44</sup>Ca is implemented into Prometheus-Hotb, but it is irrelevant on the timescales studied in this paper.

# 3 EARLY-TIME EVOLUTION: EXPLOSION AND PNS PROPERTIES

In this section, we discuss the results of the early phase of the explosion when  $t \le t_{\text{map}} = 2.5 \text{ s}$  after bounce.

In the left panel of Fig. 2, the time evolution of the diagnostic or "explosion" energies  $E_{\rm exp}$  of all models is depicted. The energy

 $E_{\rm exp}$  is defined as the sum of internal plus kinetic plus gravitational energy of all grid cells behind the shock where this total energy is positive, but it does not include the negative binding energy of the progenitor star ahead of the shock. At 2.5 s after bounce the latter is very small and  $E_{\rm exp}$  has effectively reached its terminal value as measurable for an observed SN. Once this energy reaches  $E_{\rm exp} \geq 0.005~{\rm B}~(1~{\rm B}=1~{\rm bethe}\equiv 10^{51}~{\rm erg})$ , the model is considered to explode and the corresponding instant defines the explosion time  $t_{\rm exp}$ .

Overall, all models show similar trends: once the explosion sets in, the energy grows very quickly to reach a plateau well before our mapping time  $t_{\rm map}$ . For our less energetic models (WH12.5, SW13.1, SW14.2, and SW20.8) the initial phase of slow shock expansion lasts longer than for our more energetic models (Fig. 2, right panel). In these models the neutrino heating is weaker and it takes more time to build up positive energy behind the shock and to launch the explosion. This extended delay of the explosion creates the perfect conditions for the development of early-time hydrodynamic instabilities, such as Rayleigh-Taylor overturn, convection, and SASI (Foglizzo et al. 2006; Scheck et al. 2008). The values of  $t_{\rm exp}$  and of  $E_{\rm exp}$  at 2.5 s are given in Table 2. The explosion energies at this remapping time lie in the range between 0.69 B and 1.73 B.

As discussed in Wongwathanarat et al. (2013) and Gabler et al. (2021), our simplified neutrino treatment leads to uncertainties in the electron fraction  $Y_{\epsilon}$  of the neutrino-heated ejecta and some of the matter is expelled with slightly neutron-rich conditions ( $Y_e \sim 0.46$ – 0.49). Therefore, a certain fraction of the matter that is assigned to the tracer nuclei <sup>56</sup>X could be, in fact, <sup>56</sup>Ni. Depending on the model, values between 30% and 70% are expected to be reasonable. For simplicity and to be in line with previous literature (Sukhbold et al. 2016; Utrobin et al. 2019), we will assume a representative value of 50%. Therefore, when remapping our simulations at t = $t_{\rm map}$ , we add half of the tracer material to  $^{56}{\rm Ni}$ . Consequently, from here on we will always refer to <sup>56</sup>Ni plus 50% of the tracer <sup>56</sup>X as NiCoFe0.5X, which also includes the decay products <sup>56</sup>Co and <sup>56</sup>Fe. The corresponding yields  $M_{\text{NiCoFe0.5X}}$  produced during the explosion are listed in Table 2. The different time evolutions of the pure <sup>56</sup>Ni mass (right panel) and that of NiCoFe0.5X (left) are given in Fig. 3.

Since the yields depend on how much mass can be heated to high temperatures either by neutrinos or by the outward moving SN shock, it is expected that the total mass of NiCoFe0.5X depends on the explosion energy and on the compactness of the models (e.g., Nakamura et al. 2015; Sukhbold et al. 2016; Burrows et al. 2024b). We plot the dependence of the NiCoFe0.5X mass on  $E_{\rm exp}$  in the left panel of Fig. 4. All models, except model SW19.8, follow a roughly linear correlation. When excluding this outlier model, the fit has a coefficient of determination  $R_{\rm fit}^2=0.95$ . When plotting the NiCoFe0.5X yield as function of compactness (central panel), we do not find any strong outlier, but the scatter increases ( $R_{\rm fit}^2=0.80$ ). The combination of the two parameters into a product,  $E_{\rm exp} \cdot \xi_{2.5}$ , as shown in the right panel of Fig. 4, leads to a slightly lower scatter compared to the linear fit with  $\xi_{2.5}$  alone ( $R_{\rm fit}^2=0.81$ ).

Based on the evolution of the central region of our simulations until  $t_{\rm map}$ , we can estimate the properties of the PNS at this time. The PNS mass  $M_{\rm PNS}$ , defined by the baryonic mass above a density of  $10^{11}\,{\rm g\cdot cm^{-3}}$  (which we consider as the location of the PNS surface), is listed in column 10 of Table 2. In order to compute the kinematic quantities of the PNS, we follow Scheck et al. (2006) and assume conservation of the linear and angular momenta. Since the progenitor star was at rest at the beginning of the simulation, we can estimate the linear momentum and the velocity of the PNS from the interaction with the surrounding matter. While the PNS is forced to stay at the

origin, because the centre of the gravitational potential cannot move out of the centre of the numerical grid, the ejecta are allowed to evolve freely. Therefore, the kick velocity of the PNS due to the asymmetric SN explosion can be computed from the negative of the total linear momentum of the ejecta as

$$\mathbf{v}_{\text{PNS}}(t) = -\mathbf{P}_{\text{gas}}(t)/M_{\text{PNS}}(t),\tag{9}$$

where

$$\mathbf{P}_{\text{gas}}(t) = \int_{R_{\text{PNS}}}^{R_{\text{ob}}} dV \rho \mathbf{v} \tag{10}$$

is the integral of the gas momentum between the PNS radius,  $R_{\rm PNS}$ , and the outer grid boundary,  $R_{\rm ob}$ . We obtain magnitudes of  ${\bf v}_{\rm PNS}$  between several tens of km s<sup>-1</sup> and almost 700 km s<sup>-1</sup> (see Table 2, column 11). These hydrodynamic kick velocities of the PNSs are compatible with those obtained in previous simulations (Wongwathanarat et al. 2013; Coleman & Burrows 2022; Janka et al. 2022; Janka & Kresse 2024; Burrows et al. 2024a). Because of our approximate treatment of neutrino transport with spherical neutrino luminosities imposed at the inner grid boundary, we do not evaluate our models for the PNS kicks associated with anisotropic neutrino emission.

For the computation of the angular momentum, we follow a similar procedure. Since the progenitor models are non-rotating, any angular momentum acquired by the PNS has to be balanced by an equal and opposite angular momentum of the ejected matter. Deviating from the calculation of the kick velocity, where the integration is performed on the entire grid (equations 9 and 10), numerical tests showed that it is recommended to constrain the volume of integration of the angular momentum to the immediate vicinity of the PNS (Wongwathanarat et al. 2013):

$$\mathbf{J}_{\text{PNS}}(t) = -\left[\int_{R_{\text{NS}}}^{r_0} dV \rho \mathbf{j}(t) + \int_0^t dt' r_0^2 \oint_{4\pi} d\Omega \left(\rho \mathbf{j} v_r\right)|_{r_0}\right], \quad (11)$$

where  $\mathbf{j}$  denotes the specific angular momentum,  $\Omega$  is the solid angle, and  $r_0$  is chosen to be 500 km. The first term in equation (11) accounts for the angular momentum contained in the spherical shell bounded by the PNS radius  $R_{\text{PNS}}$  on one side and by the radius  $r_0$  on the other. The second term in the bracket gives the angular momentum that is carried away by the mass leaving the volume of radius  $r_0$  until time t. For all the models of our calculations,  $J_{\text{PNS}}$  stays roughly constant after about 2 s (see, however, Janka et al. 2022 for the possible effects of later fallback and accretion). In addition to  $J_{\text{PNS}}$ , Table 2 also provides the relative angle between spin and kick directions,  $\alpha_{\text{sk}}$  (column 13), and the estimated final NS spin period  $T_{\text{spin}}$  (column 14). The latter is computed by considering the NS as a rigidly rotating, spherical body. The period is thus given by

$$T_{\rm spin} = \frac{2\pi I_{\rm NS}}{J_{\rm PNS}},\tag{12}$$

where  $I_{\rm NS}$  is approximated as the Newtonian moment of inertia of a homogeneous sphere, with final radius of  $R_{\rm PNS}=12\,{\rm km}$ . All but one of the models exhibit high angular momenta of  $J_{\rm PNS}>10^{46}\,{\rm g\cdot cm^2\,s^{-1}}$ . Consequently, the obtained spin periods are on the order of hundreds of milliseconds or below. The only deviation from this trend is model SW25.6, for which the PNS has a very low momentum ( $J_{\rm PNS}=0.32\cdot10^{46}\,{\rm g\cdot cm^2\,s^{-1}}$ ) and, hence, a very long spin period ( $T_{\rm spin}=3.5\,{\rm s}$ ). These values are also compatible with previ-

<sup>&</sup>lt;sup>1</sup> As in Wongwathanarat et al. (2013), we confirmed that the numerical result of the evaluation of equation (11) does not depend sensitively on the exact value of  $r_0$ , as long as it is in the range between  $500 \,\mathrm{km} < r_0 < 1000 \,\mathrm{km}$ .

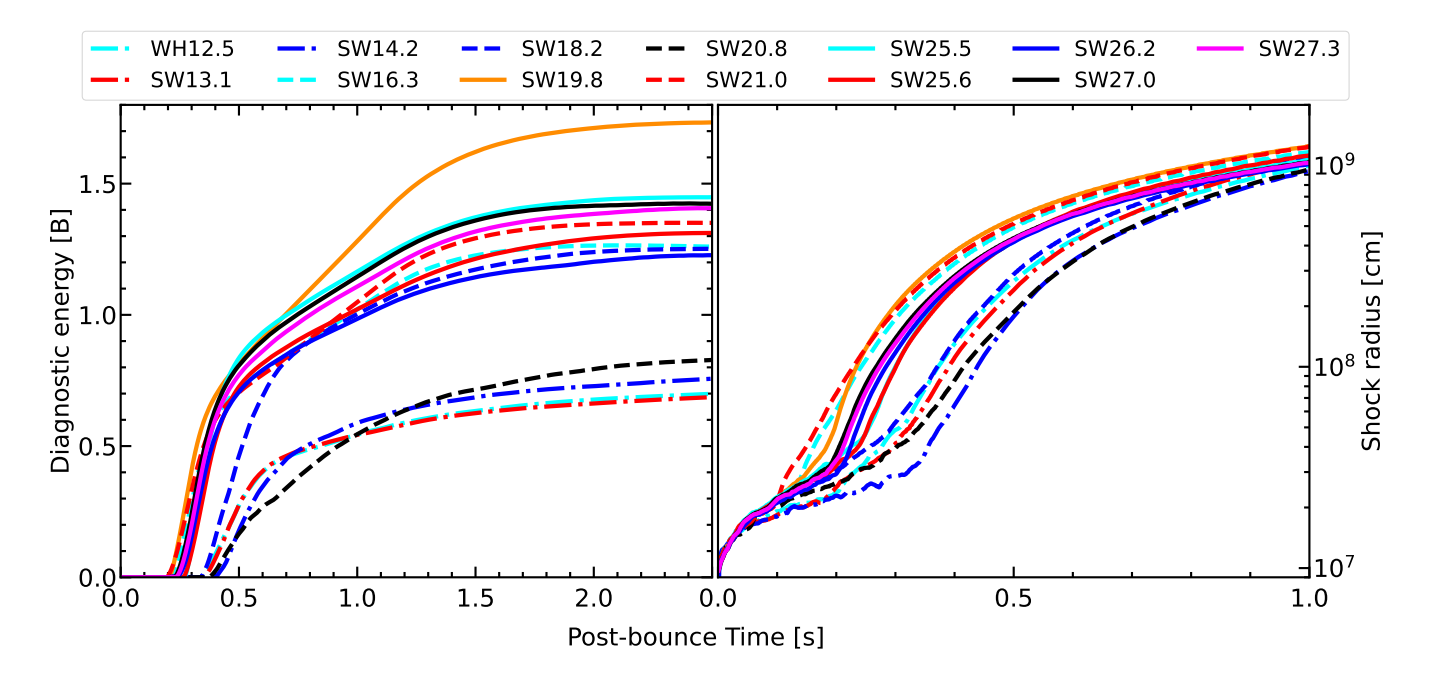


Figure 2. Evolution of the diagnostic (explosion) energies  $E_{\text{exp}}$  (left; as defined in the main text) and of the angle-averaged shock radii (right) for all computed 3D SN models versus post-bounce time. The evolution in the left panel is followed until the remapping time  $t_{\text{map}} = 2.5 \text{ s}$ , after which the diagnostic energies have effectively reached their terminal values. In the right panel, the shock expansion is displayed only until 1 s after bounce for better visibility.

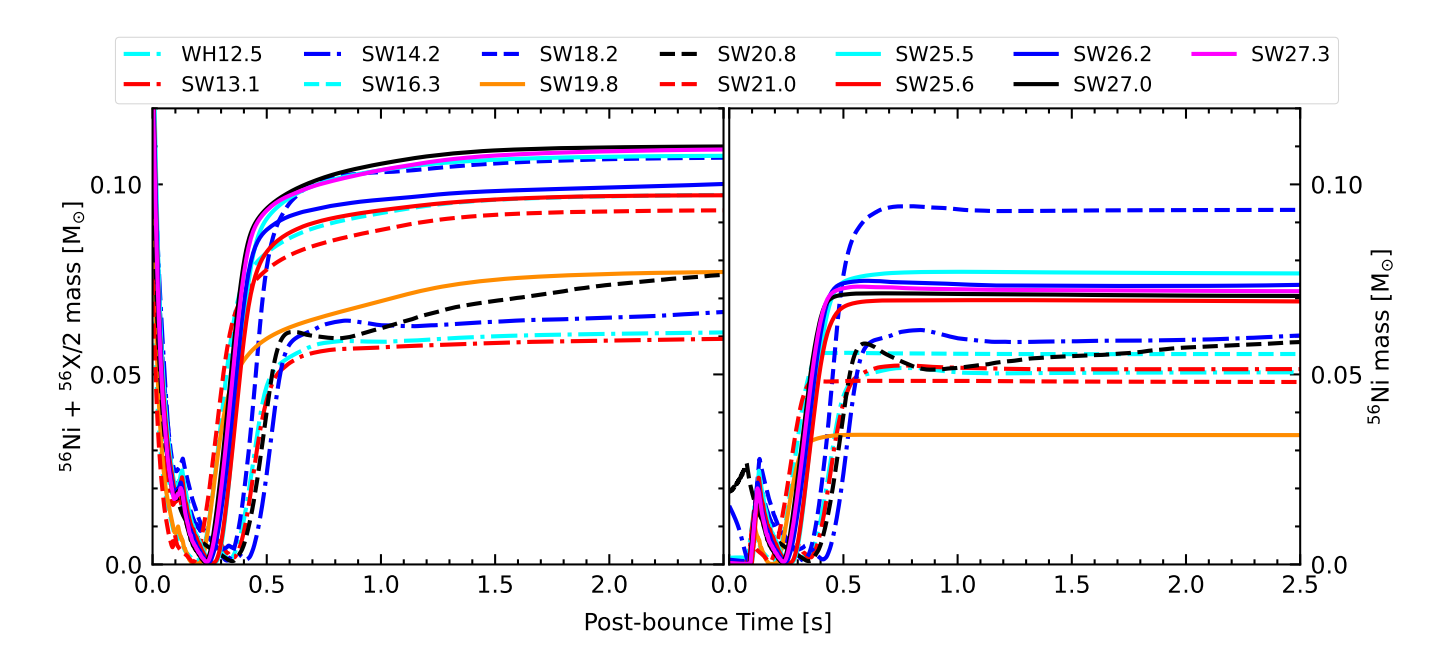


Figure 3. Evolution of the mass of  $^{56}$ Ni plus 50% of tracer  $^{56}$ X (left) and only  $^{56}$ Ni (right) in our 3D SN models. While  $^{56}$ Ni is predominantly synthesized during the first 0.5 s and plateaus after that (right panel), minor amounts of  $^{56}$ X are produced for at least one second longer.

ous studies (see e.g. Janka et al. 2022). We attribute the low angular momentum of the PNS in model SW25.6 to stochastic effects.

The angles  $\alpha_{sk}$  between the directions of PNS spins and kicks are between 37° and 130° and do not indicate any trend towards alignment or anti-alignment of the spin and kick directions.

The morphology of the freshly synthesized, heavy-element ejecta at t = 2.5 s is characterized by big buoyant plumes that are created by convective overturn in the neutrino-heated post-shock layer at the

onset of the explosion and shortly afterwards, see Fig. 5. At the displayed time, the explosion energies have reached their terminal values (see Fig. 2), the <sup>56</sup>Ni nucleosynthesis is effectively finished, and large-scale asymmetries have formed. Already at this early time, we witness differences in the morphologies: Models SW13.1 (Fig. 5 top left panel) and SW18.2 (top right) are more asymmetric with fewer extended plumes in preferred directions, whereas SW26.2 (bottom left) and SW19.8 (bottom right) tend to be more spherical with al-

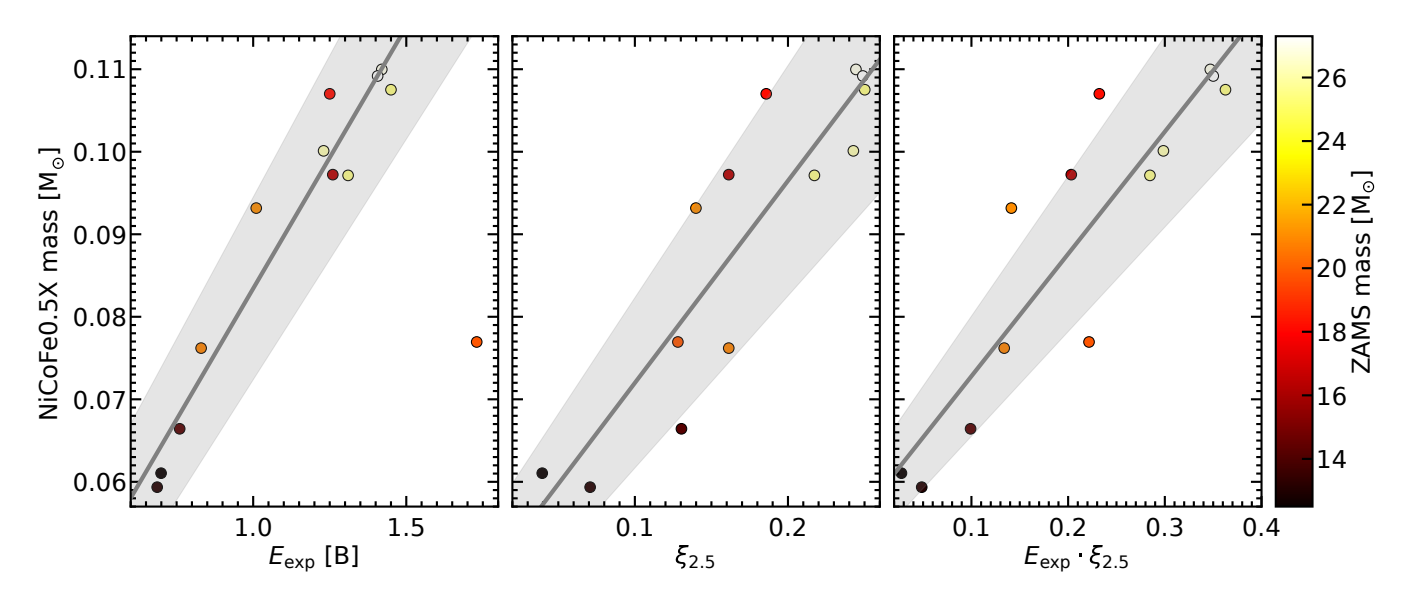


Figure 4. Correlations of the amount of produced NiCoFe0.5X at  $t_{\text{map}} = 2.5$  s with the (diagnostic) explosion energy  $E_{\text{exp}}$  (left panel), compactness  $\xi_{2.5}$  (middle panel), and the product of both (right panel). The grey lines denote linear fits of the points, and the grey-shaded bands are the  $1\sigma$  scatter regions. Note that the fit in the left panel does not include the outlier model SW19.8.

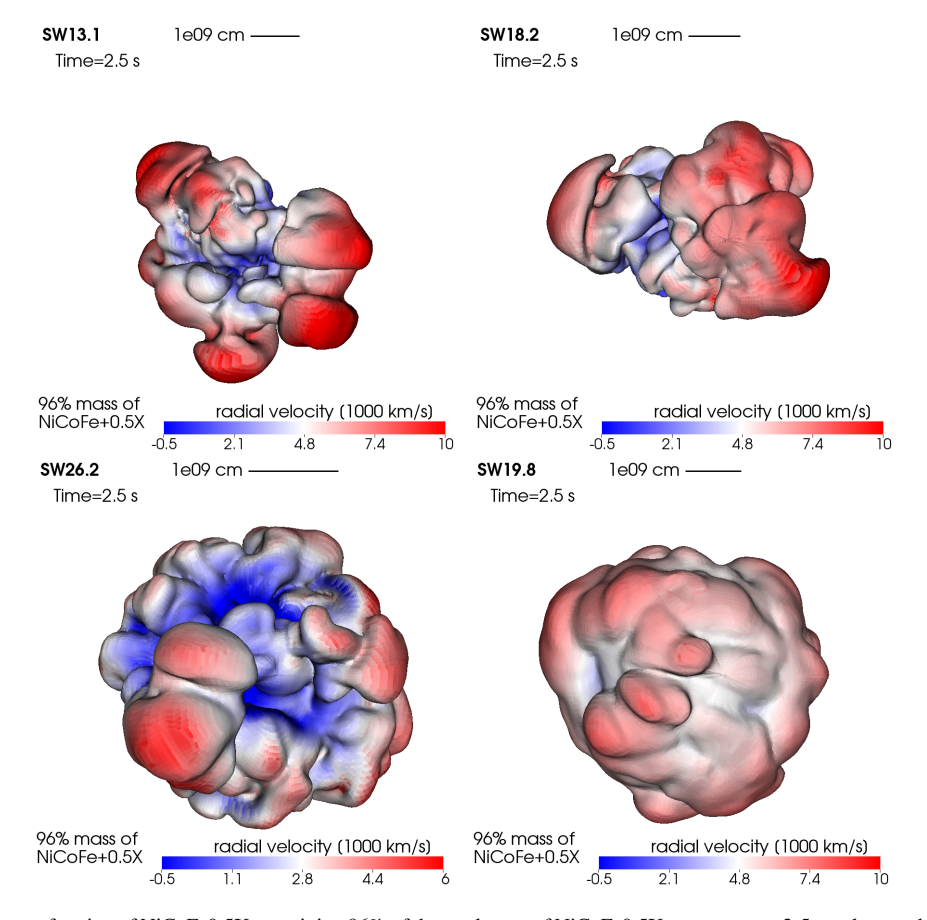


Figure 5. Isosurfaces of mass fraction of NiCoFe0.5X containing 96% of the total mass of NiCoFe0.5X at  $t = t_{\text{map}} = 2.5$  s, colour-coded with the radial velocity. The mass fraction is typically  $X_{\text{NiCoFe0.5X}} \approx 0.11$  for all the models. The models given here, SW13.1, SW18.2, SW26.2, and SW19.8 (from top left to bottom right), are the ones that will be shown throughout the paper.

most isotropically distributed plumes. These initial asymmetries will act as seeds of the extended RT fingers discussed later. The latter therefore retain a long-term memory of the large-scale asymmetries that developed during the earliest stages of the explosion.

# 4 LONG-TIME EVOLUTION: INSTABILITIES AND MIXING

In this section, we discuss the evolution of our 13 SN explosion models from t = 2.5 s post bounce until 10 days later. Before investigating in detail the radial mixing of the heavy elements created near the explosion centre into the outer layers of the star, we study the (linear) stability of the ejecta with respect to RTI in 1D in Section 4.1. We further discuss the morphologies of our 3D simulations and analyse how the mixing can be related to properties of the explosion in Section 4.5.

For the study of the 3D mixing, it turned out that our 13 models can be grouped into three different classes (see Table 2). We will analyse one reference model for each class in detail.

The first class is formed by models with the lowest investigated ZAMS masses (Low  $M_{\rm ZAMS}$ , LM) including WH12.5, SW13.1, and SW14.2. As we will show later, these models are characterized by strong mixing and the presence of two phases of RTI. The corresponding growth factors of the instabilities are highest at the locations of the (C+O)/He and He/H composition interfaces. Our reference model of this group is model SW13.1.

All the other models have higher ZAMS masses,  $M_{\rm ZAMS} > 16 \, \rm M_{\odot}$ (High  $M_{ZAMS}$ , HM) and only one dominant phase of RTI. In contrast to the LM models, the growth factors of the instability at the (C+O)/He interface are small or vanishing, and high growth factors are present only at the location of the He/H composition interface. We split this HM group further into models with lower explosion energies (HM-LE), for which the lighter elements like H and He obtain very high final velocities, and models with higher explosion energies (HM-HE), which develop tails of lower velocities for H and He. Models SW16.3, SW18.2, SW20.8, and SW21.0 belong to the HM-LE class, for which model SW18.2 is chosen as reference model. The third group, HM-HE, consists of models SW19.8, SW25.5, SW25.6, SW26.2, SW27.0, and SW27.3, with SW26.2 as reference model. The grouping into the three classes and the reference model for each class are implemented in Table 2. Note that within these classes, model SW20.8 is a kind of outlier with respect to its relatively low explosion energy of  $E_{\text{exp}} = 0.83 \,\text{B}$ , which is closer to the LM models than to the typical value in the group of HM-LE models. We chose this energy to agree with that obtained in the 1D neutrino-engine modeling by Sukhbold et al. (2016). However, since the stellar structure is closer to that of the HM-LE models, we count model SW20.8 to the HM-LE group.

#### 4.1 1D models: linear stability analysis

For simplicity and clarity, we will investigate the linear growth rates of RTIs first with the aid of 1D simulations. During the propagation of a SN shock wave through the star, the velocity of the shock varies significantly. Depending on the density stratification it encounters, a spherically symmetric blast-wave accelerates whenever the density gradient is steeper than  $r^{-3}$  (i.e.,  $d(\rho r^3)/dr < 0$ ), whereas it decelerates otherwise (Sedov 1959). In stellar progenitors, the density gradients are particularly steep when approaching composition interfaces from the interior and then they become more shallow again in the overlying shell (see Fig. 1). Consequently, the value of  $\rho r^3$ 

varies non-monotonically with the radius (Fig. 6, dotted black lines, and Fig. 7) and the shock velocity increases (decreases) when the SN shock approaches (has passed) a composition interface. Deceleration leads to an accumulation of matter, and, correspondingly, the pressure gradient with respect to the radius can change from negative to positive in the post-shock flow when the shock passes a shell interface. In contrast, the density gradient remains negative during the evolution.

These opposite gradients of pressure and density provide the condition for the growth of RTIs. The criterion for the development of RTIs in incompressible fluids as given by Chevalier (1976); Bandiera (1984); Benz & Thielemann (1990) is

$$\frac{\partial p}{\partial r}\frac{\partial \rho}{\partial r} < 0. \tag{13}$$

To compare the strength of the growth of RTIs in the explosion of different progenitors, we performed 1D SN simulations for all of the RSG models given in Table 1. Each 1D explosion was calibrated such that its energy agrees within 12% (maximum deviation) with that of the corresponding 3D SN model. The growth strength of RTIs can be monitored with the time-dependent growth factor (i.e., the growth rates integrated over time) at fixed Lagrangian mass coordinates (Hattori et al. 1986; Wongwathanarat et al. 2015; Utrobin et al. 2019, 2021),

$$\frac{\xi(t)}{\xi_0} = \exp\left(\int_0^t \sigma_{\rm RT} \, d\tau\right). \tag{14}$$

This quantity describes how much an initial perturbation with amplitude  $\xi_0$  would grow until time t. Here,  $\sigma_{RT}$  is the linear RT growth rate for an incompressible fluid, defined as

$$\sigma_{\rm RT} = \frac{1}{\rho} \sqrt{-\frac{\partial \rho}{\partial r} \frac{\partial p}{\partial r}} \,. \tag{15}$$

This incompressible RTI growth rate is often used as a lower estimate for stratified flows with buoyancy effects, where the actual growth rate may exceed the incompressible prediction (Benz & Thielemann 1990). Therefore, one can conservatively use the incompressible criterion to estimate where RTI may be strongest. However, it may both under- or overestimate the true growth depending on local conditions, which is particularly important in marginally stable regions in some of our models. As we will see later in Section 4.5, our analysis is dominated by the major contribution to the integrated, global growth rate, and subtle local changes will not affect our results significantly.

Fig. 6 displays the growth factors for RTI as a function of the enclosed mass at different times for our three reference models SW13.1, SW18.2 and SW26.2. The red, blue and black lines show the growth factors at the time when the SN shock crosses the (C+O)/He interface ( $t_{\rm CO} \sim 4 \dots 15 \, {\rm s}$ ), the He/H interface ( $t_{\rm He} \sim 120 \dots 500 \, {\rm s}$ ), and when the outermost part of the shock breaks out of the progenitor ( $t_{\rm sb,1} \sim 1 \dots 2.6 \, {\rm d}$ ), respectively (see Table 3 for these times in all of our 3D simulations). The breakout in our RSG models occurs at times roughly one order of magnitude later than those for BSG progenitors. This is due to the fact that RSG stars have, in general, much larger radii than BSG stars with comparable mass (Wongwathanarat et al. 2015; Utrobin et al. 2019; Gabler et al. 2021). In each plot three different areas representing different composition shells are colour-shaded: yellow (C+O shell), purple (He shell), and blue (H envelope).

As expected, the growth factors for model SW13.1 (top panel of Fig. 6) become significant only at the shell interfaces, where strong changes of  $\rho r^3$  are present. At 5.51 s (red line), the shock has just reached the (C+O)/He interface ( $\sim 2.6 \, \mathrm{M}_{\odot}$ ), and, consequently,

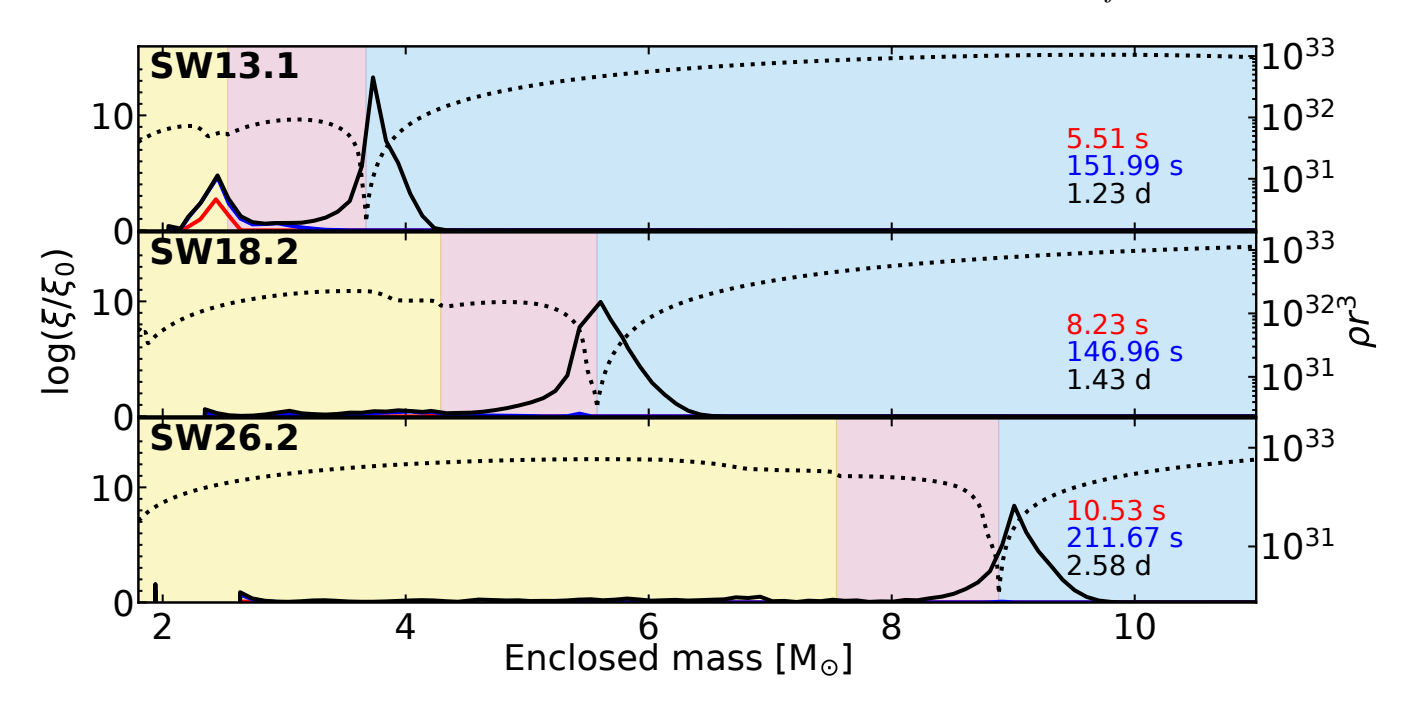
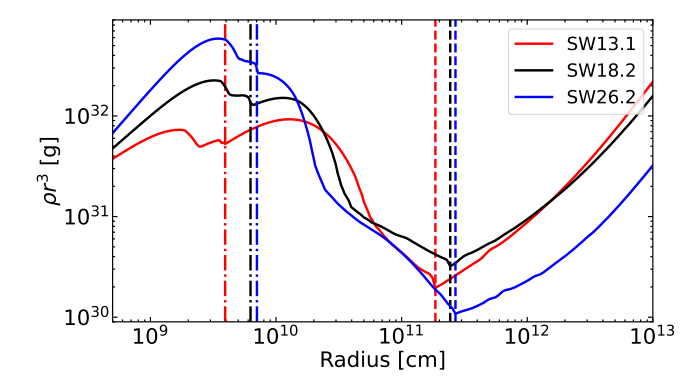


Figure 6. Growth factors (time-integrated growth rates) of RTI as functions of enclosed mass for models SW13.1 (top panel), SW18.2 (middle panel), and SW26.2 (bottom panel). They are shown at the time when the SN shock crosses the (C+O)/He interface (red lines), when it crosses the He/H interface (blue lines) and at shock breakout from the stellar surface ( $t_{sb,1}$ , black lines). The shaded areas indicate the different shells, with the respective interfaces. The yellow area is the C+O shell; the purple area is the He shell; and the blue area depicts the H envelope. The dotted lines depict the function  $\rho r^3$  for each model with the corresponding scale on the right axis. The derivative of  $\rho r^3$  of the most massive model SW26.2 does not change sign around the (C+O)/He interface ( $\sim 7.5 \, M_{\odot}$ ). Therefore, we do not expect significant RTIs in this region.

Model	t <sub>CO</sub> [s]	t <sub>He</sub>	<i>t</i> <sub>sb,1</sub> [d]	$\Delta t_{ m RS}^{ m CO}$ [s]	$\Delta t_{ m RS}^{ m He}$ [s]	$R_{\rm RS}$	$\Delta R_{\rm CO}$ [10 <sup>6</sup> km	$\Delta R_{ m He}$	log(a	ξ / ξ <sub>0</sub> ) He	$v_{\mathrm{XX}}^{\mathrm{CO}}$	$v_{\rm XX}^{\rm He}$ $[10^3]$	v <sub>XX</sub> <sup>10</sup> km s <sup>-1</sup>	$\langle v \rangle_{\rm XX}^{10}$	$X_{ m mix}$	Y <sub>mix</sub>	$M_{ m ej}^{ m 3D}$ $[{ m M}_{\odot}]$
WH12.5	4.4	122	1.09	522	405	5.9	5.8	4.3	2.8	11.5	13.8	9.3	4.8	1.4	13.59	3.53	9.18
SW13.1	5.5	152	1.23	657	511	6.6	6.5	4.8	4.9	13.5	10.5	7.2	4.1	1.0	15.69	3.92	9.17
SW14.2	6.0	182	1.20	663	487	6.6	6.5	4.7	3.3	13.2	11.0	8.7	4.4	1.4	15.44	3.12	10.20
SW16.3	6.3	166	1.33	689	530	6.9	6.8	4.8	1.3	10.0	8.8	6.6	2.6	0.9	8.60	2.79	12.24
SW18.2	8.2	147	1.43	907	768	8.7	8.6	6.2	0.8	10.0	8.5	8.0	3.6	1.3	10.64	2.70	12.12
SW20.8	13.1	260	2.23	1704	1457	11.8	11.7	8.8	0.3	11.9	7.6	7.8	3.8	1.5	15.79	2.54	12.76
SW21.0	11.3	282	1.92	1502	1232	12.0	11.9	8.8	0.4	10.7	6.6	7.2	3.4	1.2	11.13	2.94	13.79
SW19.8	10.2	202	1.74	977	786	9.9	9.8	7.2	0.7	11.4	4.3	4.4	1.7	0.7	5.84	2.47	13.56
SW25.5	10.2	207	2.36	1357	1161	13.0	12.9	10.5	0.1	12.8	4.9	5.5	2.5	1.2	7.89	2.12	11.58
SW25.6	11.2	221	2.25	1275	1066	12.5	12.4	9.7	0.3	10.5	5.0	6.0	3.0	1.2	7.10	2.48	12.08
SW26.2	10.5	212	2.58	1165	964	12.1	12.0	9.4	0.2	8.9	4.3	4.5	2.0	1.0	4.24	2.01	11.12
SW27.0	10.9	430	2.37	2502	2083	24.3	24.2	18.2	0.2	11.6	4.6	5.3	2.5	1.3	7.11	2.00	11.92
SW27.3	10.7	482	2.24	2348	1876	25.5	25.4	17.9	0.6	8.3	5.1	6.0	2.9	1.4	5.56	2.02	11.37

Table 3. Parameters of relevance for the NiCoFe0.5X mixing in our set of 3D explosion simulations of RSG progenitors. The subscript XX means NiCoFe0.5X.  $t_{\rm CO}$  and  $t_{\rm He}$  are the times when the outermost SN shock crosses the (C+O)/He and He/H composition interface, respectively.  $t_{\rm sb,1}$  is the break-out time of the maximum radius of the SN shock.  $\Delta t_{\rm RS}^{\rm CO}$  and  $\Delta t_{\rm RS}^{\rm He}$  are the time intervals between reverse-shock formation and the shock passage at the (C+O)/He and He/H interface, respectively (equations 20 and 21).  $R_{\rm RS}$  is the radius where the reverse shock forms.  $\Delta R_{\rm CO}$  and  $\Delta R_{\rm He}$  are the distances between the formation radius of the reverse shock and the (C+O)/He and He/H interface, respectively. The two columns for  $\log(\xi/\xi_0)$  contain the logarithmic maxima of the growth factors of RTI near the (C+O)/He interface (time-integrated until the SN shock crosses the He/H interface) and near the He/H composition interface (time-integrated until 10 days after the onset of the explosion), computed from corresponding 1D SN simulations.  $v_{\rm NiCoFe0.5X}^{\rm CO}$ ,  $v_{\rm NiCoFe0.5X}^{\rm He}$ , and  $v_{\rm NiCoFe0.5X}^{\rm 10}$ , are the mass-averaged velocities of the fastest 4% of the NiCoFe0.5X at the time when the SN shock passes the (C+O)/He composition interface in the 3D explosion models, when it passes the He/H interface, and 10 days after the onset of the explosion.  $\langle v \rangle_{\rm NiCoFe0.5X}^{\rm 10}$  is the mass-weighted average velocity of the remaining 96% (i.e., of the bulk) of the NiCoFe0.5X at day 10.  $X_{\rm mix}$  is the dimensionless characteristic RTI growth parameter defined in equation (22) and  $Y_{\rm mix}$  the dimensionless NiCoFe0.5X mixing parameter defined in equation (23).  $M_{\rm ej}^{\rm 3D}$  are the hydrodynamically evolved ejecta masses that are still on the 3D computational grid at 10 days.



**Figure 7.** Profiles of  $\rho r^3$  as functions of radius for the models SW13.1 (red), SW18.2 (black), and SW26.2 (blue), respectively. The vertical dash-dotted and dashed lines mark the positions of the (C+O)/He and He/H composition interfaces for the three models.

only there the growth factor has increased significantly. Once the shock reaches the He/H interface (blue line), the growth factor at the (C+O)/He interface has already reached its maximum value and the one at the He/H interface ( $\sim 3.7\,\mathrm{M}_\odot$ ) starts to grow until reaching its maximum before  $t_\mathrm{sb,1}$  (black line).  $\xi/\xi_0$  is larger at the He/H interface, since there the positive and negative gradients of the function  $\rho r^3$  are much more pronounced compared to the (C+O)/He interface. This leads to a much stronger deceleration of the SN shock in the H envelope than in the He shell (see also Section 4.2.1 and figures discussed there). At around shock breakout, the RTI growth factors have reached their saturation values and basically do not change until the end of the simulations. The behaviour in model SW13.1 is representative for models with low progenitor masses up to about  $16.3\,\mathrm{M}_\odot$ .

The growth factors at the (C+O)/He interface for more massive models are much lower or even negligibly small. In the central and bottom panels of Fig. 6 we show models SW18.2 and SW26.2 as examples for such cases. The reason for this marginally unstable, or even stable behaviour is related to the density profile. In the more massive models,  $\rho r^3$  either increases only slightly in the He shell or it is a monotonically decreasing function with radius from the (C+O)/He interface through the He shell until it starts increasing at the He/H interface. This is visible in Fig. 7, where we show the profiles of  $\rho r^3$  as functions of radius. In contrast to the low-mass models, which exhibit a clear maximum of  $\rho r^3$  in the He-shell, only a weak or no maximum is found for models with masses higher than  $16.3~M_{\odot}$ . As a consequence the SN shock hardly decelerates when passing the (C+O)/He interface and travelling into the He shell.

Comparing the HM-LE and HM-HE models, we note that the growth factors of the HM-LE models (see SW18.2 in Fig. 6) have a broader peak at the He/H interface than the HM-HE models (like SW26.2). This could indicate favourable conditions for the development of RTIs in a larger volume of the progenitor.

In some of the models the peak of the time-integrated growth factor does not exactly coincide with the He/H interface but may be slightly shifted into the H envelope (see e.g. model SW26.2 in Fig. 6). This is connected to the location of a pile-up of He-rich matter just behind the SN shock when it decelerates in the H-shell (Kifonidis et al. 2003). This so-called "He wall" pushes against the hydrogen layer without getting unstable to RTIs immediately. The formation of RT unstable conditions is therefore delayed for some time, causing the displacement of the peak of the RTI growth factor away from the He/H interface.

In this section, we have analysed the growth conditions for RTI by considering growth factors based on linear perturbation theory applied to the structure of 1D models at different times. However, once favourable conditions for RTI exist, the instability is expected to grow and to quickly enter the non-linear regime in the 3D case, thus significantly changing the structure of the SN ejecta compared to the 1D case. Therefore the consequences of the instability need to be studied by multi-dimensional simulations.

# 4.2 Radial mixing

We begin our analysis of the radial mixing by considering the normalized mass distributions for different elements ( $^1$ H,  $^4$ He,  $^{12}$ C,  $^{16}$ O,  $^{28}$ Si, and NiCoFe0.5X) at a time shortly after the innermost part of the deformed SN shock has left the radius of the star, such that all of the matter of the progenitor has been shocked. Figs. 8 and 9 display these mass distributions for models SW13.1, SW18.2, and SW26.2 as functions of the radial velocity and enclosed mass, respectively. In general, the ejecta can be divided into a group of light elements ( $^1$ H and  $^4$ He: blue and cyan solid lines in the figures), intermediatemass elements that are partially already present in the progenitor ( $^{12}$ C,  $^{16}$ O, and  $^{28}$ Si: red, black, and blue dashed lines) and heavy, iron-group elements represented by NiCoFe0.5X, which is made in the explosion (red solid line).

At the late stage of the evolution, the former onion-shell structure of the different elements in the progenitor is only partially maintained (Fig. 8). Model SW26.2 (bottom panel) has the least mixing and the high-velocity tails of the distributions reproduce the expected order of the elements best: farthest outside are the lighter elements ( $v \leq 5500 \,\mathrm{km}\,\mathrm{s}^{-1}$ ), followed by intermediate elements  $(v \leq 4500 \,\mathrm{km \, s^{-1}})$  and NiCoFe0.5X is located at the lowest velocities ( $v \leq 3000 \,\mathrm{km}\,\mathrm{s}^{-1}$ ). Note that apparent discrepancies in the fraction of mass per velocity bin can appear due to different total masses. It seems that oxygen is located further inside than carbon or silicon (bottom panel). However, this is an artifact of the rescaling by the total mass of the respective element and the distributions of silicon, oxygen and carbon are actually strongly related. This connection is represented by the same shape of the distribution, not necessarily by the same amplitude. In particular, the massive O-layers of the progenitors imply that smaller fractions of the total O masses are mixed or accelerated to high velocities. This reduces the amplitude of the corresponding high-velocity tails of the displayed normalized distributions. In the other models, SW18.2 (central panel) and SW13.1 (top panel) the mixing of heavy and intermediate mass elements is much more effective and manifests itself in NiCoFe0.5X (red solid lines) reaching or even overtaking the fastest oxygen (black dashed lines).

We now discuss the different models in more detail. The velocity distribution of the freshly synthesised NiCoFe0.5X in model SW13.1 (top panel of Fig. 8) is characterized by a maximum around  $\approx 950 \, \mathrm{km \, s^{-1}}$ . The distributions of intermediate-mass and low-mass elements peak at successively higher velocities up to a maximum of  $\approx 2000 \, \mathrm{km \, s^{-1}}$  for H. All elements have high-velocity tails reaching up to velocities well above  $4000 \, \mathrm{km \, s^{-1}}$ . Table 4 provides additional quantitative information. There, we give the values of the mass-weighted average velocities of the fastest 4% of NiCoFe0.5X,  $\nu_{\mathrm{NiCoFe0.5X,4\%}}$ , and of the bulk of NiCoFe0.5X,  $\nu_{\mathrm{NiCoFe0.5X,bulk}}$ . The bulk refers to the 96% of the mass that remains after excluding the fastest 4%. In addition, the velocities of the peaks of the distributions are given. These data are taken at  $t = t_{\mathrm{sb,2}}$  in 3D, and at the time of shock breakout for the 1D quantities. The strong mixing, in particular, of the heavy elements from deep inside into the outer layers of

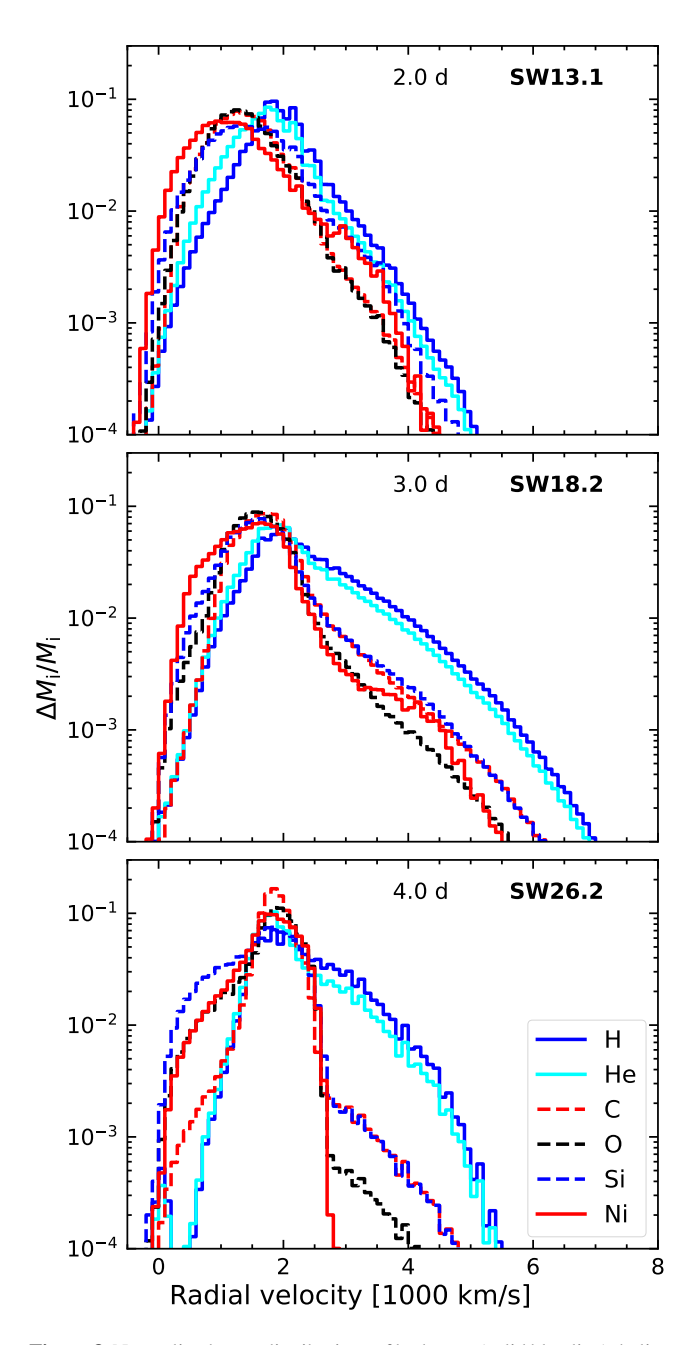


**Figure 8.** Normalized mass distributions of hydrogen (solid blue line), helium (solid cyan line), carbon (dashed red line), oxygen (dashed black line), silicon (dashed blue line), and NiCoFe0.5X (Ni in the legend, solid red line) versus radial velocity for models SW13.1, SW18.2, and SW26.2 shortly after complete shock breakout. The radial velocity bins have a width of  $\Delta v_r = 100 \, \mathrm{km \, s^{-1}}$ .

the progenitor occurs in the form of extended finger-like structures, which also contain intermediate-mass elements, see Fig. 10, where we plot NiCoFe0.5X isosurfaces at different times for the three representative models. In the mass distribution in Fig. 8, one can notice a slight overabundance of heavier elements like NiCoFe0.5X and  $^{28}\mathrm{Si}$  compared to the intermediate-mass elements  $^{12}\mathrm{C}$  and  $^{16}\mathrm{O}$  for velocities in a wider interval around  $\sim 3000\,\mathrm{km\,s^{-1}}$ . Since each of the plotted distributions is normalized by the total mass of the corresponding chemical element, this overabundance just means that a larger fraction of the total mass of the element has been mixed into this range of velocities, as mentioned above. In addition, the lighter

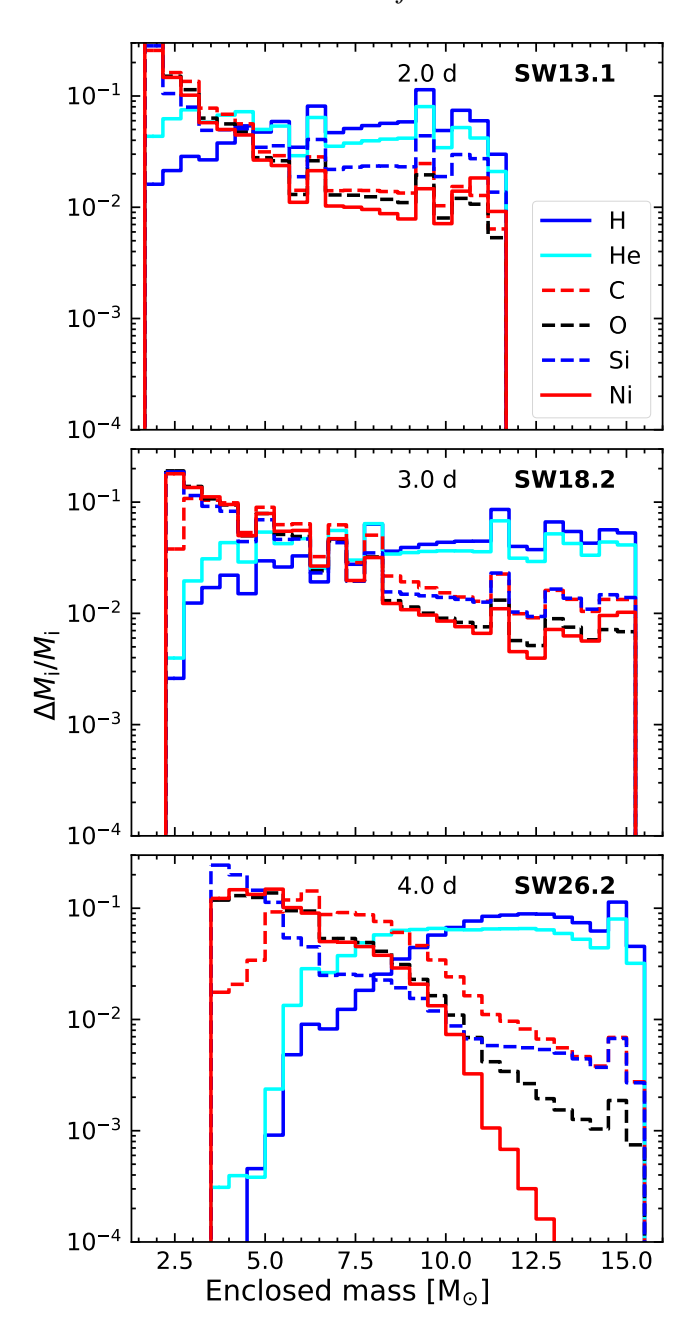


**Figure 9.** Normalized mass distributions of hydrogen (solid blue line), helium (solid cyan line), carbon (dashed red line), oxygen (dashed black line), silicon (dashed blue line), and NiCoFe0.5X (Ni in the legend, solid red line) versus enclosed mass for models SW13.1, SW18.2, and SW26.2 shortly after complete shock breakout. The mass bins have a width of  $\Delta M=0.4\,M_\odot$ . Since some of the low-velocity matter has left the numerical grid through the inner boundary during the simulation, the lines start at enclosed masses that are larger than the PNS masses in Table 2.

elements H and He mix towards low velocities, even negative ones. These negative velocities are a consequence of the interaction of inner He and H ejecta with the reverse shock (see Section 4.2.1). Later, these ejecta (or a part of them) may be re-accelerated outwards, owing to additional energy input by the  $\beta$  decay of radioactive NiCoFe0.5X as well as a possible self-reflection of the reverse shock at the centre (Gabler et al. 2021). Unfortunately, we cannot track the matter in the innermost regions to study potential fallback onto the compact rem-

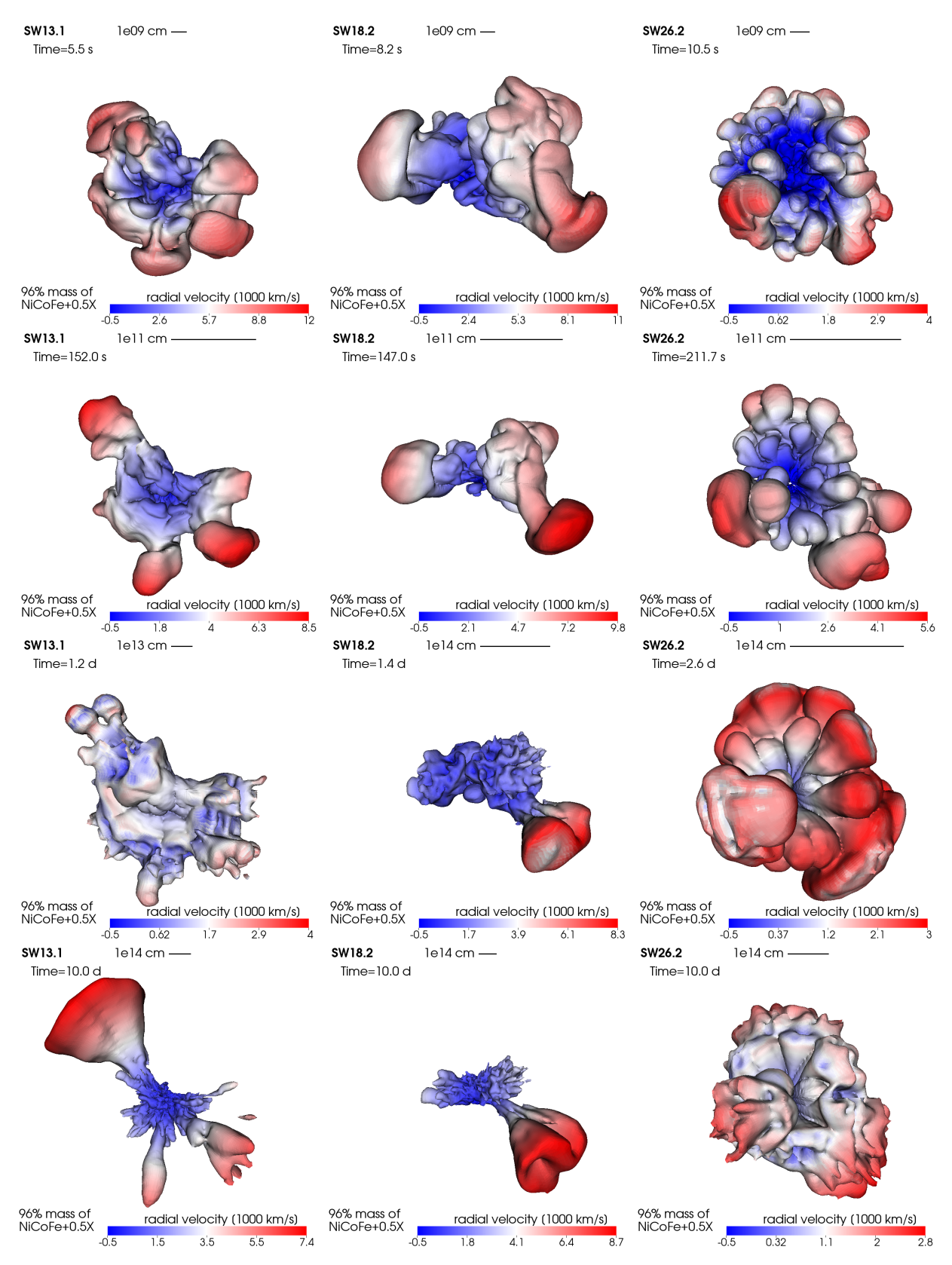


Figure 10. Isosurfaces of mass fraction of NiCoFe0.5X that contain 96% of the total mass of NiCoFe0.5X. The mass fractions typically lie in the interval  $0.006 \leq X_{\rm NiCoFe0.5X} \leq 0.10$ . The 3D plots are given for the representative models SW13.1, SW18.2, and SW26.2 (left, middle, and right column, respectively). The orientation, i.e., viewing direction, is the same as in Fig. 5. Colours show the radial velocities of the material in units of  $1000 \, \rm km \, s^{-1}$ . The four selected times correspond to the time when the SN shock crosses the (C+O)/He interface  $t_{\rm CO}$  (top row), approximately to the times when it crosses the He/H interface  $t_{\rm He}$  (second row) and when the maximum of the shock passes the surface of the star  $t_{\rm sb,1}$  (third row), and to the end of the simulations at 10 d (bottom row). Model SW13.1 is the most asymmetric one with the most extended RTI fingers after 10 days, whereas the ejecta of the most massive model end up with a less extreme deformation. The action of the reverse shocks is visible by bluish patches ahead of deep-red surface regions in the two rightmost panels of the third row, and the bluish region behind the red tips of the RT-fingers in the left plot of the same row. MNRAS 000, 1–29 (2025)

Model	v <sub>XX,4%</sub>	v <sub>XX,4%</sub>	v <sub>XX,bulk</sub> [km s	v <sub>XX,bulk</sub>	v <sub>peak</sub> <sup>3D</sup>	$v_{\rm peak}^{\rm 1D}$
WH12.5	3538	741	1499	591	1450	729
SW13.1 SW14.2	2949 3541	1184 1169	1372 1523	984 919	1150 1750	953 1036
SW16.3	2686	2470	1796	1866	1750	1727
SW18.2 SW20.8	3139 2947	1874 1950	1750 1661	1661 1824	1850 1650	1657 1950
SW21.0	2713	2127	1741	1833	1850	2127
SW19.8 SW25.5	2917 3004	3106 1749	2144 2155	2835 1484	2350 2150	3004 1743
SW25.6	3128	1872	2184	1591	2350	1872
SW26.2 SW27.0	2905 3209	2137 1456	2002 2220	1809 1174	2250 2550	2010 1327
SW27.3	3528	2130	2378	1856	2550	2125

**Table 4.** Different characteristic velocities of NiCoFe0.5X distribution (XX=NiCoFe0.5X) for 3D and 1D explosions at the time of shock breakout (in the 3D case this is when the minimum radius of the deformed shock breaks out  $t = t_{\rm sb,2}$ ). Columns 2 (3) contain the mass-weighted average velocities of the entire fastest 4% of the NiCoFe0.5X ejecta,  $v_{\rm NiCoFe0.5X,4\%}$ , and columns 4 (5) the mass-weighted average velocities of the bulk,  $v_{\rm NiCoFe0.5X,bulk}$ , for the 3D (1D) simulations, respectively. In columns 6 and 7, we list the velocities at the peaks of the distributions,  $v_{\rm peak}$ , in 3D and 1D, respectively.

nant, because we have to cut out the central part to increase numerical efficiency. The other models with low ZAMS masses, WH12.5, and SW14.2 exhibit qualitatively similar velocity distributions.

In model SW18.2 (Fig. 8, central panel) we find very fast-moving ejecta reaching 6000 km s<sup>-1</sup> and more. The much faster ejecta at early times compared to model SW13.1 can usually not be explained by the higher explosion energies of the HM-LE models, because the energy differences between LM and HM-LE models are relatively small and the ejecta velocities scale only with the square root of this energy. The main reason for the higher velocities is therefore the later times at which the results are evaluated for the HM-LE models, because the breakout of the minimum shock radius  $(t_{sh,2})$  happens much later in these models. Therefore, the ejecta can re-accelerate after they were slowed down by the reverse shock. In Fig. 11, we see that the ejecta of the LM models at 10 d have comparable or even higher velocities than those of the slightly more energetic HM-LE models, because bigger ejecta masses reduce the expansion velocities  $(v_{\rm ei} \propto \sqrt{E_{\rm exp}/M_{\rm ei}})$  and because the LM models have a more efficient RT-caused acceleration.

As for the mixing, it is important to inspect the differences between different chemical elements in a given model at a given time. Similar to the results for model SW13.1, all elements are mixed up to very high velocities, and we find NiCoFe0.5X up to 5500 km s<sup>-1</sup>, for example. However, in contrast to the LM model, where all elements are distributed over very similar velocity ranges, we see that H and He, in particular, extend to considerably higher velocities. Moreover, also larger relative fractions of these elements (i.e., higher values of  $\Delta M_{\rm H}/M_{\rm H}$  and  $\Delta M_{\rm He}/M_{\rm He})$  can be found at velocities higher than the peaks of the distributions. These lighter elements also do not mix as efficiently to lower or negative velocities as in the discussed LM case. Model SW18.2, similar to model SW13.1, has well-developed RT fingers that extend far out from the bulk of the element distributions (see panels in the central column of Fig. 10). However, since model SW18.2 has only one region of RTI growth at the He/H interface, the inward mixing of He and H into the C+O core is reduced and the outwards rising fingers are slightly less pronounced at 10 days. Similar properties are also observed in models SW16.3, SW20.8, and SW21.0.

Our third mixing case is represented by model SW26.2. For this model, the peaks of the distributions of the heavy elements at  $\approx 2000 \, \mathrm{km \, s^{-1}}$  are both the most pronounced and found at the highest velocities among the different model classes. These high bulk velocities are caused by the high explosion energies of the HM-HE class. Similar to model SW18.2, the (C+O)/He interface is not RT unstable, and the morphological features in the right panels of the top and second rows of Fig. 10 originate from initial asymmetries during the shock revival phase. Their structures are present since these very early post-bounce times and hardly change in shape during the subsequent evolution over timescales of hundreds of seconds, indicating that these structures are not related to secondary RTIs at the (C+O)/He interface. In contrast to model SW13.1, the velocities of the maxima of the distributions of intermediate-mass and high-mass elements are almost identical. These similar bulk velocities indicate inefficient mixing of NiCoFe0.5X into the outer H and He layers. The ejecta rather stay mostly unmixed, but a fair fraction of the material of the outer progenitor layers has been slowed down by the reverse shock such that it expands with velocities similar to the explosively synthesized inner ejecta. This implies that there is a clear separation of the freshly synthesized higher-mass and intermediate-mass species from the intermediate-mass elements and much of the light elements of the progenitor. The steep drops of the mass distributions of all heavy and intermediate-mass elements at around  $v_r \sim 2500 \,\mathrm{km \, s^{-1}}$ marks the contact region between the explosively synthesized and reprocessed ejecta and the pre-existing progenitor material. There is essentially no mixing beyond  $v_r \sim 2500 \,\mathrm{km}\,\mathrm{s}^{-1}$ . This interpretation is also supported by the mass distributions of different chemical elements as functions of enclosed mass for model SW26.2 in the bottom panel of Fig. 9, where one can see that NiCoFe0.5X is mixed outward only up to  $\sim 12\,M_\odot$  and the original progenitor composition is present outside of this mass coordinate. At 12 M<sub>☉</sub> there is a sharp drop in NiCoFe0.5X and a small hump in the other elements, indicating some kind of pile-up of the material. The outermost  $\approx 3 \, \mathrm{M}_{\odot}$ contain effectively no NiCoFe0.5X. In contrast, we find NiCoFe0.5X mixed outwards into the outermost layers of the progenitor in model SW13.1 and, for a slightly lower fraction of the total mass, also in model SW18.2 (top and middle panel of Fig.9). This difference can be understood by the fact that the reverse shock in model SW26.2 forms well outside of the NiCoFe0.5X-rich ejecta and does not allow for significant amounts of NiCoFe0.5X to be included in the RTI fingers that grow at the He/H interface. Therefore, no efficient large-scale radial mixing of NiCoFe0.5X occurs. Consequently, the final geometry of the NiCoFe0.5X ejecta is much less deformed and looks more spherical than that in models SW13.1 and SW18.2 (see bottom right panel of Fig. 10). Also, the inward mixing of lighter elements in model SW26.2 is much less significant, and within the innermost 3 M<sub>☉</sub> there is basically no hydrogen and only very little helium (bottom panel of Fig. 9). The presence of central helium in regions where there is no hydrogen in this model may be a relic of the nucleosynthesis in the neutrino-heated ejecta. A significant fraction of the alpha particles from the nuclear freeze-out phase may not be able to combine to heavier elements due to the fast expansion of the innermost ejecta. In the lighter models, we see a significant increase of the mass fraction of the <sup>1</sup>H and <sup>4</sup>He at low enclosed mass over time, clearly indicating the inwards mixing of these elements from the outer shells of the progenitors.

In Fig. 11, we show the mass distributions of the NiCoFe0.5X ejecta as functions of velocity at 10 days for a selection of models to highlight the different behaviours encountered at the same late time.

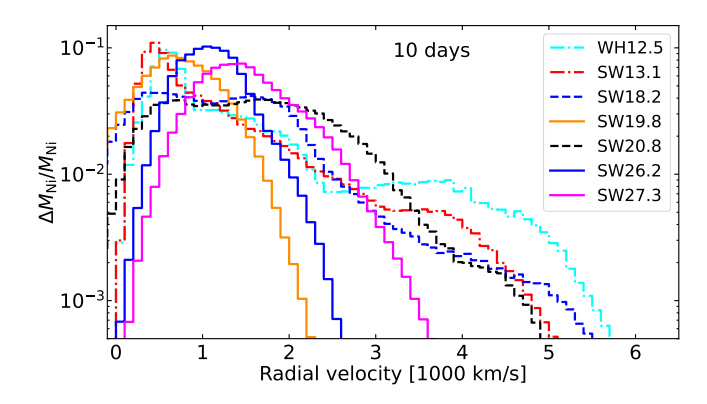


**Figure 11.** Normalized mass distributions of NiCoFe0.5X versus radial velocity at 10 days after the explosion for different models.

The LM models (WH12.5 and SW13.1) have the sharpest and most narrow peaks of their distributions at the lowest velocities, but their NiCoFe0.5X ejecta also reach the highest velocities in the tails of the distributions. The HM-HE models (SW19.8, SW26.2, and SW27.3) have the overall most narrow distributions with the most prominent peaks at higher velocities and the lowest maximum velocities. And the HM-LE models (SW18.2 and SW20.8) possess the overall flattest distributions with two less pronounced peaks < 2000 km s<sup>-1</sup> and with tails that tend to lie between those of the other two groups.

#### 4.2.1 Interaction with the reverse shock from the He/H interface

Figs. 12 and 13 show the evolution of the angle-averaged positions and velocities of the forward (SN) shock (solid red lines) and the reverse shock (dashed red lines) that is formed when the forward shock passes the He/H interface and gets strongly decelerated in the H envelope of our three sample models. In addition, the radius outside of which 4% of the total NiCoFe0.5X mass are located as well as the mass-weighted average velocity of these outermost 4% of the NiCoFe0.5X ejecta are plotted by blue solid lines in the respective figures. It is important to note that these outermost 4% of the NiCoFe0.5X reside at the largest distances away from the explosion centre at a given time, but they are not necessarily the fastest NiCoFe0.5X ejecta at this instant. The outermost NiCoFe0.5X ejecta may be slowed down by the interaction with the reverse shock, and transiently, some of the NiCoFe0.5X located deeper in the interior may exhibit higher speeds.

The outermost 4% of the NiCoFe0.5X in SW13.1 (top panel in Fig. 12) have a very high initial velocity. At the earliest times, these ejecta even seem to be located outside of the angle-averaged forward shock. This impression, however, is just caused by the different ways to compute the angle-averaged radii, because in each direction NiCoFe0.5X is fully embedded in ejecta behind the SN shock. The corresponding evolution of the velocity is given in the top panel of Fig. 13. The initially very fast NiCoFe0.5X ejecta (blue line) slow down to velocities much slower than the averaged forward shock velocity (red solid line) well within the He shell, and then reach similar velocities compared to this shock at later times ( $t \geq 3000 \,\mathrm{s}$ ) when the SN shock is strongly decelerated in the H envelope. Therefore, when the SN shock has passed the He/H interface (dotted grey line) the outermost NiCoFe0.5X ejecta still follow the average forward shock rather closely. Shortly after this time, the reverse shock forms just slightly in front of the fastest NiCoFe0.5X. Since this NiCoFe0.5X quickly crosses the reverse shock, it is not slowed down

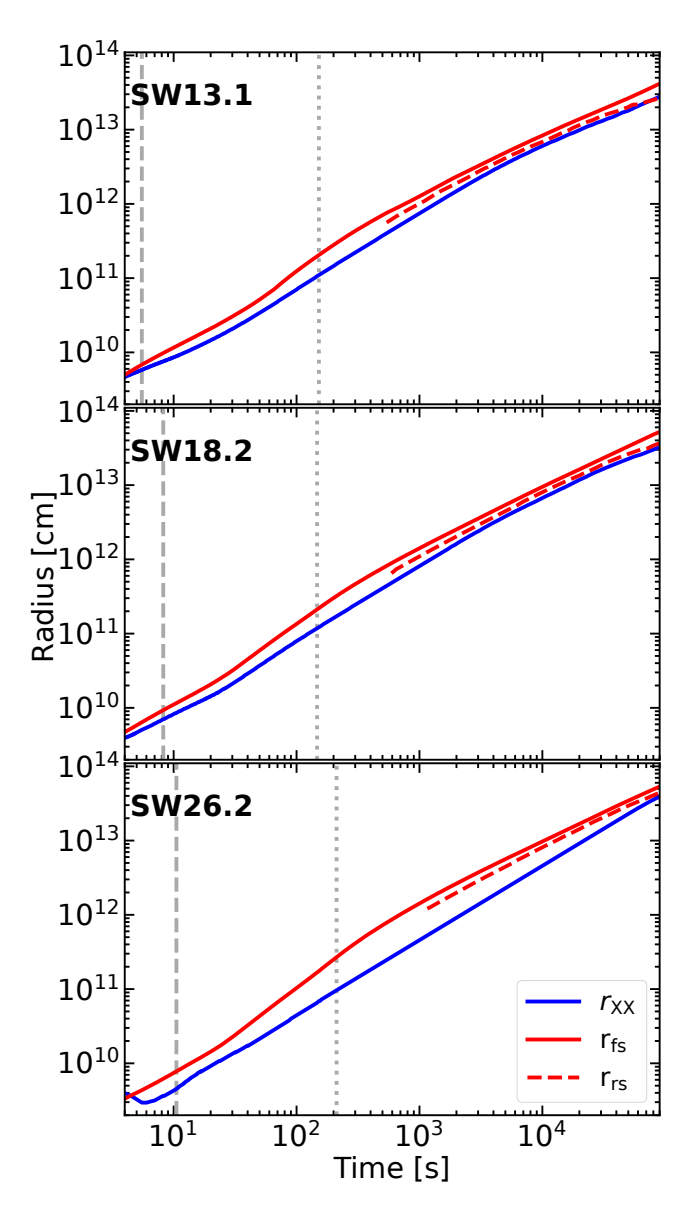


**Figure 12.** Time evolution until about one day of the angle-averaged radius of the forward SN shock,  $r_{\rm fs}$  (solid red line), angle-averaged radius of the reverse shock formed by the deceleration of the SN shock in the H envelope  $r_{\rm rs}$  (dashed red line), and of the inner boundary of the outermost 4% of NiCoFe0.5X,  $r_{\rm XX}$  (XX = NiCoFe0.5X, solid blue line), in models SW13.1, SW18.2, and SW26.2. The vertical dashed and dotted grey lines indicate the times when the SN shock passes the (C+O)/He and the He/H interfaces, respectively. Model SW26.2 is the only model among the three in which the shocks and the 4%-NiCoFe0.5X surface are not very close throughout the entire evolution.

significantly, and the reverse shock is considerably faster than the outermost NiCoFe0.5X ejecta only for a short period of time after it has formed. As a result, the fast NiCoFe0.5X-rich matter is involved in the growth of RT fingers, which carry NiCoFe0.5X into the H+He envelope of the progenitor with maintained high velocities, not affected by significant deceleration in the surrounding medium (left panels of the bottom two rows of Fig. 10). The tips of these RT fingers get compressed and correspondingly flattened when they reach the forward shock and get slowed down substantially.

The evolution of model SW18.2 is very similar. Also here the outermost NiCoFe0.5X remains rather close to the average forward

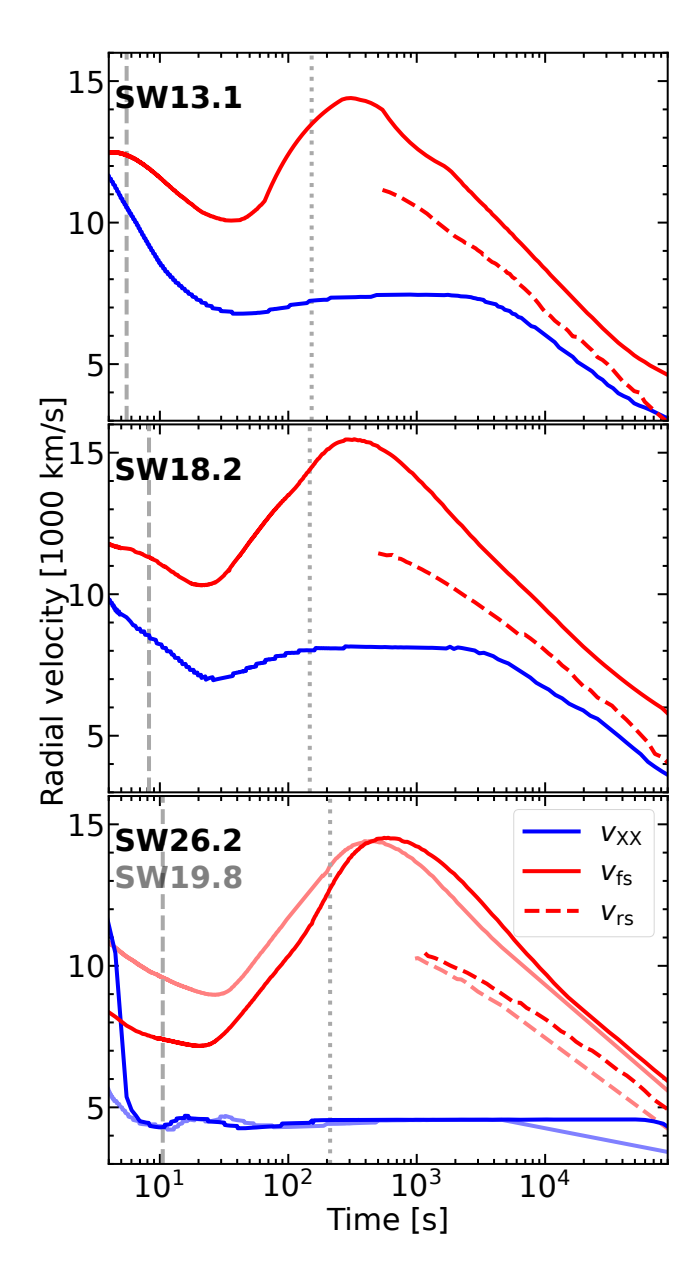


**Figure 13.** Time evolution until about one day of the velocities of the angle-averaged SN shock,  $v_{\rm fs}$  (solid red line), of the angle-averaged reverse shock,  $v_{\rm rs}$  (dashed red line), and of the mass-weighted average velocity  $v_{\rm XX}$  (XX = NiCoFe0.5X, solid blue line) at the inner boundary  $r_{\rm XX}$  of the outermost 4% of NiCoFe0.5X (see Fig. 12) for models SW13.1, SW18.2, and SW26.2. The vertical dashed and dotted grey lines indicate the times when the SN shock passes the (C+O)/He and the He/H interfaces, respectively. In the bottom panel the results of model SW19.8 are also plotted with light-coloured lines. Note that for this additional model the vertical grey lines are not plotted since they are very similar to the respective times for model SW26.2 (see Table 3). The extreme deceleration of the ejected NiCoFe0.5X in the C+O shells of models SW26.2 and SW19.8 is caused by particularly shallow density profiles in these layers (for more details, see Section 4.2.1).

shock all of the time. Once the reverse shock is formed and the outermost NiCoFe0.5X interacts with it, the tips of the fingers containing 96% of the ejected NiCoFe0.5X mass experience visible flattening (Fig. 10, middle column, third row).

In the case of model SW26.2 the situation is different. The outermost 4% of the NiCoFe0.5X ejecta always stay well behind the forward shock (Fig. 12, bottom panel) and expand with a much lower

average velocity (Fig. 13, bottom panel). Consequently, the reverse shock forms far outside of these ejecta and the latter approach the shock only after several 10<sup>4</sup> s. Accordingly, the velocities of the two shocks are several 1000 km s<sup>-1</sup> higher than the average velocity of the outermost 4% of the NiCoFe0.5X-rich ejecta until about  $5 \times 10^4$  s (Fig. 13). For this reason even the outermost NiCoFe0.5X ejecta are not significantly involved in the growth of the RTI at the He/H composition interface, and most of the slow-moving NiCoFe0.5X gets stuck in the dense shell of He (the He wall mentioned in Sect. 4.1) that piles up at the base of the H envelope when the material of the He shell is decelerated by the reverse shock. This pile-up of matter leads to the local peak in the mass distributions at about  $15 \, M_{\odot}$  in the bottom panel of Fig. 9, which also shows that there is hardly any mixing of NiCoFe0.5X beyond this local peak into the H+He envelope of the progenitor. The weak growth of RTI fingers including NiCoFe0.5X can also be recognized in Fig. 10, see the third and fourth rows in the right column there.

In the bottom panel of Fig. 13 we also display the results for model SW19.8 by light-coloured lines. Both the velocity of the shock and the average velocity of the outermost 4% of the NiCoFe0.5X behave similarly to those in model SW26.2. In particular, the NiCoFe0.5X in both models is strongly decelerated in the very early phase of the explosion ( $t \leq 5$  s). This efficient deceleration is caused by the NiCoFe0.5X interaction with the C+O core, which is much more massive and has a shallower radial density distribution in these models compared to the case of SW18.2 and, in particular, of model SW13.1 (see inset in Fig. 1). Once the fastest NiCoFe0.5X ejecta have been decelerated to velocities around 5000 km s<sup>-1</sup>, they are not able to re-accelerate later on but keep on moving with an almost constant velocity (bottom panel of Fig. 13). Correspondingly, also in model SW19.8 the mixing of NiCoFe0.5X into the H+He envelope is inefficient and the final distribution of NiCoFe0.5X is rather spherical with only small-scale structures associated with weakly developed RT fingers (Fig. 14). These similarities further justify our inclusion of model SW19.8 in the class of HM-HE models.

# 4.2.2 The effects of multi-dimensional instabilities

In general, the velocity distributions of the chemical elements in the CCSN ejecta are determined by the explosion energy (setting the overall scale), the density gradients in the progenitor star (allowing for deceleration or acceleration), the  $\beta$  decay of radioactive elements (further accelerating NiCoFe0.5X-rich ejecta, see Gabler et al. 2021, for a detailed discussion), and the development of non-linear and non-radial hydrodynamic instabilities. While the first three effects can be studied to a certain extent in 1D, the genuinely multi-dimensional instabilities affecting the motion and mixing of the ejecta, including in particular NiCoFe0.5X, require full 3D simulations for a reliable assessment of their consequences. To better understand the impact of RTIs, we thus compare our 3D models to 1D simulations.

RTIs affect especially the mixing of the fastest of the heavy and intermediate-mass elements. Therefore, we expect the most prominent differences between 1D and 3D to occur in the tails and wings of the mass distributions of these elements, e.g., of NiCoFe0.5X, for models that show particularly strong mixing. The corresponding normalized distributions of the mass fraction of NiCoFe0.5X as functions of radial velocity for our reference models at different times are shown in Fig. 15.

For model SW13.1 (top panel) the peaks of the distributions in 3D and in 1D coincide roughly at all selected times. However, the distributions are much wider and the fastest NiCoFe0.5X is significantly faster in 3D. Initially (when the SN shock passes the He/H interface),

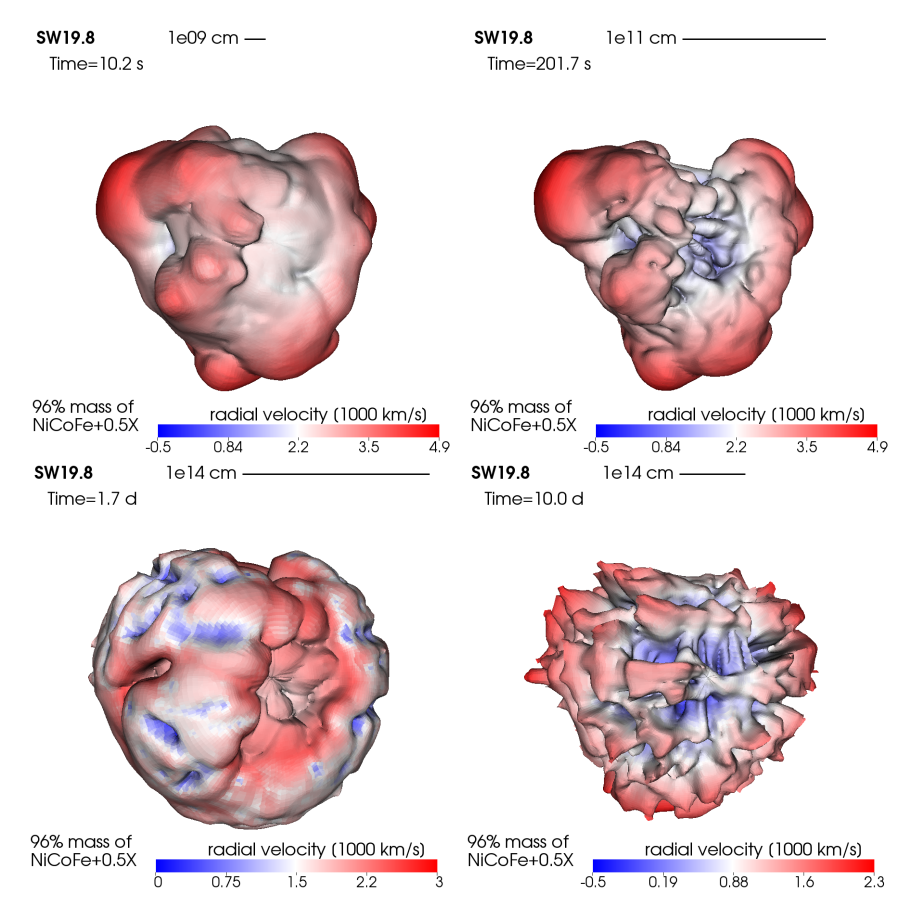


Figure 14. Isosurfaces of mass fraction of NiCoFe0.5X containing 96% of the total mass of NiCoFe0.5X for model SW19.8. The displayed times are selected analogue to Fig. 10 and the sequence runs from top left to bottom right. The colour coding represents the radial velocity. The orientation, i.e., viewing direction, is the same as in Fig. 5. The mass fractions of the first three images of the sequence lie in the range  $0.007 < X_{\text{NiCOFe0.5X}} < 0.08$ , and for the last image at 10 d the mass fraction is  $X_{\text{NiCOFe0.5X}} \approx 0.007$ 

the NiCoFe0.5X-rich ejecta have a very wide velocity distribution reaching up to more than  $4000\,\mathrm{km\,s^{-1}}$  ( $\gtrsim 8000\,\mathrm{km\,s^{-1}}$ ) in 1D (3D). During the outward expansion and the interaction with the reverse shock, the ejecta are slowed down significantly until shock breakout ( $t_{\mathrm{sb,2}}$ , blue lines), resulting in a much narrower velocity distribution, in particular in 1D. The wider spread of the velocities on both sides of the distribution maximum and the much higher maximum velocities in 3D indicate very strong radial mixing. Note that the high-velocity tail of the distribution of model SW13.1 in 3D (in contrast to 1D) experiences a considerable acceleration from shock breakout up to 10 d, because a substantial fraction of the NiCoFe0.5X has been mixed into the outermost layers of the progenitor.

As in model SW13.1, the peaks of the normalized mass distributions in model SW18.2 (central panel of Fig. 15) in 3D and 1D are at about the same velocities, but they are much flatter in 3D and the distributions are correspondingly much wider. This is compatible with the strong mixing that occurs also in model SW18.2. Compared to model SW13.1, however, the distribution maxima of the 3D version of SW18.2 are much broader at late times and even develop a double-peak structure. The 1D maximum lies right between these peaks. Similarly to SW13.1, the tail of the distribution in the HM-LE model SW18.2 displays a significant change between shock breakout and 10 d.

Different from the other two models, the peak and width of the distributions of model SW26.2 evolve only very little with time in 1D (bottom panel of Fig. 15), mainly because of the lack of significant

shock deceleration in the He shell (Fig. 13, bottom panel), where the gradient of  $\rho r^3$  is negative in the progenitor (Fig. 7). In the corresponding 3D simulations, the peak changes its position from about  $\sim 3000\,\mathrm{km\,s^{-1}}$  at the time the SN shock crosses the He/H interface to  $\sim 1000\,\mathrm{km\,s^{-1}}$  at  $t=10\,\mathrm{d}$ . The spread of the distributions is larger in 3D compared to 1D, but the extended tails at high velocities are absent, compatible with the weak mixing of NiCoFe0.5X into the H envelope in model SW26.2.

Therefore, in contrast to the 1D simulations, 3D models with efficient RT mixing exhibit some acceleration of the fastest NiCoFe0.5X from  $t = t_{\rm sb,2}$  to 10 d. Such a late-time acceleration can be caused by four effects: acceleration in a steep density gradient of the CSM around the progenitor star, heating due to <sup>56</sup>Ni decay, re-acceleration by the self-reflected reverse shock from the He/H interface and ongoing RTI growth. While the first three effects are also present in 1D and, in particular,  $\beta$  decay and self-reflected shock acceleration should affect more the bulk of the ejecta, late-time acceleration due to RTI is the most likely cause of the velocity increase of the fastest ejecta. This reasoning is supported by the last two rows of panels for models SW13.1 and SW18.2 in Fig. 10. There, we see an increase in the maximum velocity of the colour scale with increasing time, and the RT fingers extend much further after shock breakout. Since the NiCoFe0.5X-rich matter in model SW26.2 does not show strong RTI, the absence of late-time acceleration in this model is consistent with this line of argument.

In Table 4 we provide the characteristic velocities computed from

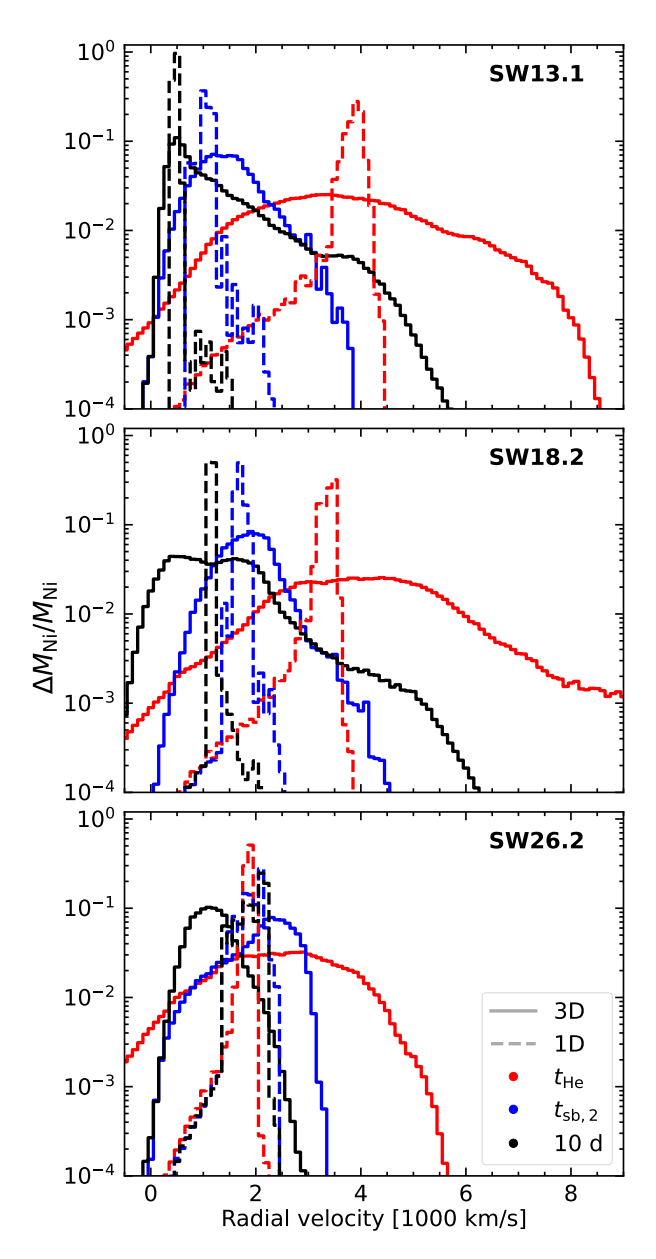


**Figure 15.** Normalized mass distributions of NiCoFe0.5X versus radial velocity at different times in 1D (dashed lines) and 3D (solid lines) for our reference models. The distributions are plotted when the SN shock passes the He/H composition interface ( $t_{\rm He}$ , red lines), at the time when the minimum radius of the shock breaks out of the progenitor star ( $t_{\rm sb,2}$ , blue lines), and at the end of the simulation (black lines). The specific values of these times can be found in Table 3. The 1D data are rescaled by  $\sqrt{E_{\rm exp}^{\rm 3D}/E_{\rm exp}^{\rm 1D}}$ , where  $E_{\rm exp}^{\rm 1D}$  and  $E_{\rm exp}^{\rm 3D}$  are given in Table 2.

the mass distributions of NiCoFe0.5X for the 1D and 3D versions of all of our models at the time when the shock (minimum radius of the shock,  $t_{\rm sb,2}$ ) breaks out from the star in 1D (3D): the mass-weighted average velocities of the fastest 4% of the NiCoFe0.5X,  $v_{\rm NiCoFe0.5X,4\%}$ , the mass-averaged bulk velocities of the remaining 96%,  $v_{\rm NiCoFe0.5X,bulk}$ , and the velocities of the peaks of the mass distributions,  $v_{\rm peak}$ . In particular, for the 1D simulations, the LM models display a trend to lower bulk velocities than the HM-LE and HM-HE models. In 3D, the bulk velocities of LM models are considerably higher than in 1D due to the strong mixing, and the

separation to the HE models does not appear as extreme. Among the 3D HM models the HM-HE tend to have higher velocities of the bulk and of the peak of the distributions than the HM-LE models. While there are some exceptions, like the low  $v_{\rm peak}^{\rm 1D}$  of model SW27.0, these trends are slightly clearer for the peak velocity compared to the bulk velocities. Almost all LM and HM-HE models show higher peak and bulk velocities in 3D compared to 1D, while the HM-LE models show comparable 1D and 3D velocities without a clear trend towards faster (bulk) ejecta in 3D.

In 1D, there is a clear correlation between the bulk velocity and  $v_{\rm NiCoFe0.5X.4\%}^{\rm 1D}$ . The LM models have the lowest velocities for both, and the velocities of HM-LE models are significantly faster. The absolute velocities of the HE-HM models show a larger dispersion, however, the correlation between  $v_{\text{NiCoFe0.5X,bulk}}^{\text{1D}}$  and  $v_{\text{NiCoFe0.5X,4\%}}^{\text{1D}}$ remains. In 3D, this correlation does not hold. The LM models have still the lowest bulk velocities, while, in contrast, their  $v_{\text{NiCoFe0.5X.4\%}}^{\text{3D}}$ are amongst the highest. Due to their stronger mixing, the LM models exhibit very high velocities of the fastest NiCoFe0.5X. Though some of the models (e.g. SW16.3) show similar velocities of the distribution peaks in 1D and in 3D, other models do not agree that well, and the differences between the velocities of the peaks of the distributions in 3D and 1D are generally comparable to the differences between the corresponding bulk velocities. Therefore, we will continue our analysis with the bulk velocities as reference values. In addition,  $v_{\text{NiCoFe}0.5\text{X,bulk}}^{\text{3D}}$  was also considered by Utrobin et al. (2019) and Utrobin et al. (2021), whose discussion we partly extend to RSGs

We point out somewhat larger differences between the 3D and 1D results of model SW27.0 compared to our other simulations for progenitors with similar masses. This peculiarity of model SW27.0 is connected to a strong initial expansion of the stalled shock, which breaks down because of insufficient push by neutrino heating and is followed by a contraction phase before the explosion of the 1D model ultimately sets in. Such a dynamical behaviour of the shock with one or more transient expansion and contraction episodes preceding the final explosion is a feature that is witnessed quite often in 1D models (see, e.g., Buras et al. 2006; Ertl et al. 2016) but occurs very rarely in 3D. As a consequence, the explosion of model SW27.0 in 3D sets in earlier than its 1D counterpart and its explosion energy becomes about 10% higher than that of model SW27.0 in 1D (Table 2). Although the long-term evolution of the shock velocity and of the outer ejecta is similar in the 1D and 3D simulations, the region where most of the NiCoFe0.5X forms is located at slightly smaller radii in the 1D simulation of SW27.0. During the later evolution this leads to considerably lower NiCoFe0.5X velocities in the 1D case despite the fact that the total kinetic energy of all ejecta of the two models is comparable. Since the explosion dynamics of SW27.0 in 3D resembles that of the other progenitors with comparable masses, the results for the NiCoFe0.5X velocities of these 3D models are more similar to the other models of comparable mass.

# 4.3 Evolution of 3D morphologies

Fig. 10 shows snapshots of the time evolution of the isosurfaces that contain 96% of the total NiCoFe0.5X mass with the highest mass fraction in our representative models SW13.1, SW18.2, and SW26.2. The mass fractions enclosing 96% of the mass are typically lower for later times and reach from  $X_{\text{NiCoFe0.5X}} \sim 0.1$  at 2.5 s (Fig. 5) to about  $X_{\text{NiCoFe0.5X}} \gtrsim 0.005$  at 10 d. This decrease is related to the expansion and mixing of the NiCoFe0.5X-rich ejecta and stalls once the expansion is homologous. The colour coding represents the radial velocities of the matter on this surface.

20

The NiCoFe0.5X morphology at the times when the SN shock crosses the (C+O)/He shell interface (top row of panels in Fig. 10) still reflects the 3D NiCoFe0.5X distribution shortly after the onset of the explosion when <sup>56</sup>Ni nucleosynthesis is finished (see Fig. 5). The subsequent changes of the geometry of the chosen surface are affected by the shock deceleration and acceleration phases in the stellar composition shells, the RTIs at the composition-shell interfaces, and the reverse shock that is formed when the SN shock is decelerated upon travelling though the extended RSG envelope. When the SN shock slows down in the He shell, the most elongated initial NiCoFe0.5X plumes can transiently get compressed before they grow again by RTIs at the (C+O)/He interface. This can be seen when comparing the morphology at subsequent times in the different rows of Fig. 10. The time increases from top to bottom.

In model SW13.1, the most extended NiCoFe0.5X fingers are clearly connected to the largest initial NiCoFe0.5X plumes, but their shapes change over time. At the time when the shock crosses the He/H interface (second row of panels in Fig. 10), these large plumes have already undergone one phase of RTI growth and extend farther from the central ejecta. The initial mushroom-head-like structures are less clearly defined. In contrast, in models SW18.2 and SW26.3 the NiCoFe0.5X plumes at about the same time (roughly 150 s–220 s post bounce) are still more similar to those at the earlier times in the top row. The mushroom-like NiCoFe0.5X fingers have actually become more stretched and possess more prominent mushroom heads, because these characteristic features could grow (nearly) unaffected by the effects of SN shock deceleration in the He shell and by the growth of RTI at the (C+O)/He interface, both of which are weak in these two models (Section 4.1).

At  $t \sim t_{\rm sh,2}$  (third row in Fig. 10) the global asymmetries imprinted on the NiCoFe0.5X distribution by the generically anisotropic explosion mechanism can still be witnessed in all cases, but the effects of the RTI at the He/H interface and that of the reverse shock building up between  $\sim 500 \,\mathrm{s}$  and  $\sim 1000 \,\mathrm{s}$  (see Fig. 12) are clearly visible now. The most prominent NiCoFe0.5X mushrooms exhibit clear signs of fragmentation to smaller structures and of corrugation due to a second phase of RT growth in all three models. Mushroom "splitting" occurs in models SW13.1 and SW18.2 and mushroom merging and surface roughening is visible in model SW26.2. Moreover, the biggest NiCoFe0.5X plumes in SW26.2 are particularly strongly affected by compression due to the fact that the reverse shock forms far ahead of the outermost NiCoFe0.5X (see Section 4.2.1 and Fig. 12). In model SW18.2, the reverse shock has massively decelerated the weaker and initially slower of the two most prominent initial NiCoFe0.5X fingers (at the 9 o'clock position in the middle panel of the third row in Fig. 10), whereas in model SW13.1, the reverse shock has only just started to interact with the matter behind the most extended NiCoFe0.5X plumes. Some of these plumes have already penetrated into the H envelope through the growth of RTI at the He/H interface, while others still exhibit deceleration at the tips of their heads with faster moving matter pushing from below (see also top panel in Fig. 12). We note that the fastest NiCoFe0.5X finger in model SW18.2 at the 5 o'clock position contains extremely little mass (compatible with Figs. 8, 9, and 15), which explains why its velocity is still nearly 8000 km s<sup>-1</sup> at shock breakout, although the fastest 4% of the NiCoFe0.5X in this model should have much lower velocities at this time when extrapolating the velocity evolution seen in Fig. 13.

At 10 days (bottom row in Fig. 10), prominent, very elongated fingers have reappeared in models SW13.1 and SW18.2 in the directions of the largest NiCoFe0.5X plumes existing at the earliest times (top row). These structures have grown again because of the action of RTI at the He/H interface and possibly partial acceleration of the

outermost NiCoFe0.5X by radioactive heating though the decay of  $^{56}\mathrm{Ni}$  to  $^{56}\mathrm{Co}$ . At the same time the reverse shock has compressed the central ejecta such that the RT fingers stick out even more pronounced. The outermost NiCoFe0.5X in models SW13.1 and SW18.2 reaches the SN shock, which deforms the caps of these fingers into anvil-like shapes. This effect is not visible in model SW26.2, where NiCoFe0.5X is only weakly mixed into the H envelope (Section 4.2 and Fig. 9). The strong compression and deceleration by the reverse shock have led to a more spherical shape of the NiCoFe0.5X ejecta at 10 d in this model, although their global geometry is still preserved from the early times. Considerable fragmentation has taken place due to the RTI at the He/H boundary and has created fine structure and smaller clumps in the final NiCoFe0.5X distribution.

These effects observed in model SW26.2 are even more extreme in model SW19.8 (Fig. 14). In this latter model, NiCoFe0.5X is similarly strongly decelerated to maximum velocities of only around 5000 km s<sup>-1</sup> when the SN shock slows down while propagating through the (C+O) layer (Fig. 13). In this very early and energetic explosion, the initial NiCoFe0.5X plumes are more isotropically distributed than in the other discussed reference models, and the overall shape of the NiCoFe0.5X isosurface therefore looks more spherical (Fig. 5). In the absence of very prominent seed asymmetries and due to the lack of substantial RTI growth at the (C+O)/He interface, no extended NiCoFe0.5X fingers form until ~200 s (upper right panel of Fig. 14) and the ejecta display a less extreme asphericity than in the other models at about the same time (Fig. 10). Subsequently, after the SN shock has entered the H envelope and once again experiences a phase of deceleration, the reverse shock forms far ahead of the slowly moving NiCoFe0.5X (Figs. 12 and 13). The reverse shock is particularly strong because of the energetic explosion of model SW19.8. After about 1 day it begins to directly interact with the outermost NiCoFe0.5X and compresses the heads of the mildly developed <sup>56</sup>Ni-rich RT mushrooms. This is visible as the slower whitish-bluish NiCoFe0.5X ahead of faster, red-coloured material deeper inside in the lower left panel of Fig. 14. The massive He wall that builds up at the base of the H envelope and the late growth of RTI at the He/H interface, which takes place quite deep inside the H shell in this model, does not permit efficient NiCoFe0.5X mixing into the outer layers of the progenitor. The final NiCoFe0.5X surface in Fig. 14 (lower right panel) is therefore closer to a sphere that is nearly isotropically perturbed only by small NiCoFe0.5X fingers of roughly the same size in all directions.

# 4.4 Asymmetric shock breakout

Early-time observations of a growing number of different kinds of CCSNe have been able to capture the shock-breakout phase (e.g., Garnavich et al. 2016; Barbarino et al. 2017; Förster et al. 2018; Huang et al. 2018; Singh et al. 2019; Soumagnac et al. 2019; Xiang et al. 2019) and thus provide important insights into the near-surface structure of the progenitors and of their immediate surroundings, which were shaped by the mass loss that had taken place shortly before the stars collapsed (e.g., Dessart et al. 2017; Rubin & Gal-Yam 2017; Bersten et al. 2018; Kozyreva et al. 2020). Effects associated with the intrinsically 3D structure of fully convective RSG envelopes (e.g., Chiavassa et al. 2011, 2024, and references therein) and the lower-density "halo" of material outside of the traditional photosphere in corresponding 3D models (Goldberg et al. 2022) as well as inhomogeneities in the close circumstellar environment (Fryer et al. 2020) can have an important impact on the rise time, duration, luminosity, and direction dependence of the shock-breakout signal and on conclusions that can be drawn on the stellar radius. A similarly

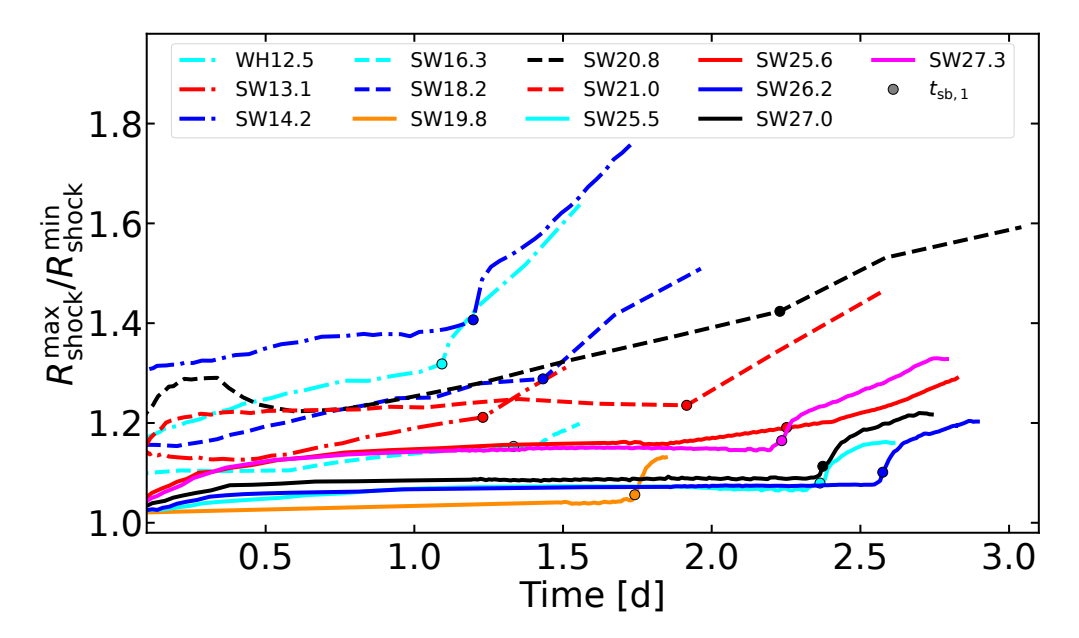


**Figure 16.** Asymmetry of the forward shock in all 3D SN models as function of time, expressed by the dimensionless ratio of the maximum shock radius and the minimum shock radius. The coloured bullets mark the times when the maximum shock radius reaches the surface of the stars, corresponding to the times  $t_{\rm sb,1}$  given in Table 5. All lines stop at the times when the minimum shock radius arrives at the surface of the progenitors ( $t_{\rm sb,2}$  in Table 5).

Model	$t_{\rm sb,1}$	$t_{\text{sb,2}}$ [d]	$\Delta t_{\mathrm{sb}}$	$\Delta t_{\rm sb}  t_{\rm sb,1}^{-1}$
WH12.5 SW13.1	1.09 1.23	1.56 1.51	0.47 0.28	0.43 0.23
SW14.2	1.20	1.75	0.55	0.46
SW16.3	1.33	1.53	0.20	0.15
SW18.2	1.43	1.96	0.53	0.37
SW20.8	2.23	3.04	0.81	0.36
SW21.0	1.92	2.58	0.66	0.34
SW19.8	1.74	1.84	0.10	0.06
SW25.5	2.36	2.61	0.25	0.11
SW25.6	2.25	2.83	0.58	0.26
SW26.2	2.58	2.89	0.31	0.12
SW27.0	2.37	2.73	0.36	0.15
SW27.3	2.24	2.79	0.55	0.25

**Table 5.** Shock breakout times (in days) in all models listed in column 1, for the maximum radius of the forward shock ( $t_{\rm sb,1}$ , column 2), the minimum radius of the forward shock ( $t_{\rm sb,2}$ , column 3), and the difference between the two ( $\Delta t_{\rm sb}$ , column 4). The last column gives the ratio of the columns 4 and 2.

important role can be expected for the asphericity of the SN shock due to the generically asymmetric explosions (Stockinger et al. 2020; Kozyreva et al. 2022; Vartanyan et al. 2025a).

For this reason we provide the times (in days) for the breakout of the deformed shocks in all of our 3D SN simulations in Table 5, specifically the breakout times of the maximum radius of the forward shock,  $t_{\rm sb,1}$ , those of the minimum radius of the forward shock,  $t_{\rm sb,2}$ , and the differences between these two instants,  $\Delta t_{\rm sb}$ . In all models the outermost parts of the shock arrive at the stellar surface within  $1 \, {\rm d} < t_{\rm sb,1} < 3 \, {\rm d}$ , which is in line with previous findings for energetic explosions of RSGs (Wongwathanarat et al. 2015; Gabler et al. 2021; Vartanyan et al. 2025a), and the slowest parts of the shock reach the surface between 0.1 d and ~0.8 d later.

Generally, the breakout times of our models tend to correlate with

the progenitor masses in Table 5. Two competing aspects influence this behaviour. On the one hand, the explosion energies of our 3D models vary by up to a factor ~2.5 (between 0.69 B and 1.73 B; Table 2) between LM and HM-HE cases, and the average shock velocity scales roughly with the square root of the explosion energy. On the other hand, the progenitor stars of the LM cases possess smaller radii (Table 1) and the shocks reach the stellar surfaces more quickly. Therefore our LM models typically possess smaller breakout times than the models with higher masses, but because of the two opposing effects the correlation is not perfect. For example, model SW20.8 has a significantly larger breakout time than models with similar masses and radii (e.g., SW19.8 and SW21.0), because the explosion energy of SW20.8 is particularly low (Table 2).

Moreover, models whose explosion starts extremely asymmetrically and which retain the large degree of asymmetry of the NiCoFe0.5X distribution in the H envelope due to efficient NiCoFe0.5X mixing into the outer stellar layers, also show the highest spread of the shock-breakout times  $t_{sb,1}$  and  $t_{sb,2}$ . Since the fast, extended NiCoFe0.5X fingers reach to the shock and push it from behind, they foster the development of most extreme shock deformation at the time of shock breakout. This is evident from Fig. 16, which displays the time evolution of the ratio of the maximum to the minimum shock radius as a measure of the shock asphericity. All models explode asymmetrically, although the degree of initial asymmetry can be more or less extreme (Figs. 5, 10, and 14). However, even models that have very large, asymmetrically distributed NiCoFe0.5X plumes initially are not guaranteed to preserve a strong asymmetry of the shock until the latter reaches the progenitor surface. Only in those cases where efficient mixing of NiCoFe0.5X at the He/H interface takes place, the ratio of  $R_{\rm shock}^{\rm max}/R_{\rm shock}^{\rm min}$  is still high after the shock has entered the H envelope (i.e., at early times in Fig. 16, where the time axis starts at  $t \sim 10^4$  s). It then generally remains high or even grows noticeably until the maximum radius of the shock breaks out from the stellar surface. In contrast, in the 3D explosions of the more massive progenitors, where the NiCoFe0.5X mixing at the He/H interface is much weaker (Sections 4.1 and 4.2; Figs. 6, 9, 12, and 13), the ratio  $R_{\rm shock}^{\rm max}/R_{\rm shock}^{\rm min}$  is closer to unity at  $t \sim 10^4$  s (Fig. 16) and stays nearly constant or increases only little when the shock continues to propagate through the H envelope until  $t_{\rm sh,1}$ . Model SW19.8 has a particularly low SN shock asymmetry (radius ratio near 1) because of its quite roundish ejecta morphology already before the shock crosses the (C+O)/He interface (see Fig. 14). After first shock breakout, the ratio  $R_{\rm shock}^{\rm max}/R_{\rm shock}^{\rm min}$  begins to rapidly rise in all the models, because the slower parts of the shock still travel in the H envelope, whereas the outermost sections of the shock are already accelerating in the steep density decline outside of the star which connects the surface of the pre-collapse progenitor model to the CSM assumed around the progenitor.

#### 4.5 The link between 3D mixing and RTIs

As discussed in Section 4.2.2, the velocity of the fastest 4% of NiCoFe0.5X and its relation to the bulk velocity of the NiCoFe0.5X can be used to characterize the degree of chemical-element mixing that takes place in hydrodynamic 3D explosion models. This measure was considered by Utrobin et al. (2019) and Utrobin et al. (2021) to link the NiCoFe0.5X mixing to the growth of RTIs in a larger set of 3D SN simulations of BSG progenitors. Here, we extend the discussion of those papers to SNe of RSG progenitors and generalize the relations found for the explosions of BSGs. The values of model-specific quantities needed in our analysis of the present section are listed in Table 3.

Let v be the maximum velocity of NiCoFe0.5X. The contribution of the growth of RTIs to the evolution of the velocity can be roughly described by the following differential equation:

$$\frac{dv}{dt} = \beta \sigma_{\rm RT} v_0 \,, \tag{16}$$

where  $\beta$  is an empirical buoyancy coefficient,  $v_0$  is the initial radial velocity of NiCoFe0.5X, and  $\sigma_{RT}$  is the linear RT growth rate defined in equation (15). The solution of equation (16) is given by

$$v(t) = \beta v_0 \int_0^t \sigma_{RT}(\tau) d\tau = \beta v_0 \ln \left( \frac{\xi(t)}{\xi_0} \right), \tag{17}$$

where  $\xi(t)/\xi_0$  is the time-integrated RTI growth factor defined in equation (14). Depending on the model, we have up to two main phases of the growth of RTIs. In order to estimate the total effect on the velocity evolution, we split the integral in equation (17):

$$v(t) = \beta v_0 \left( \int_0^{t_{\text{He/H}}} \sigma_{\text{RT}}^{\text{CO}}(\tau) d\tau + \int_{t_{\text{He/H}}}^t \sigma_{\text{RT}}^{\text{He}}(\tau) d\tau \right)$$
$$= \beta v_0 \left[ \ln \left( \frac{\xi(t_{\text{He/H}})}{\xi_0} \right)^{\text{CO}} + \ln \left( \frac{\xi(t)}{\xi_0} \right)^{\text{He}} \right], \tag{18}$$

where  $t_{\rm He/H}$  is the time when the shock passes the He/H interface,  $\sigma_{\rm RT}^{\rm CO}$  and  $\sigma_{\rm RT}^{\rm He}$  are the RTI growth rates at the respective interfaces, and  $(\xi/\xi_0)^{\rm CO}$  and  $(\xi/\xi_0)^{\rm He}$  the respective RT growth factors. Since the contribution to  $\xi(t)/\xi_0$  from the (C+O)/He interface saturates roughly when the shock passes the He/H interface, we can limit the first integral to that time. Given that there is no growth of RTIs at the He/H interface before the shock passes this interface, we further approximate the second term by

$$\int_{t_{\rm LO, UI}}^{t} \sigma_{\rm RT}^{\rm He}(\tau) d\tau \approx \int_{0}^{t} \sigma_{\rm RT}^{\rm He}(\tau) d\tau \,. \tag{19}$$

Thus we can directly employ the values of the analysis in Section 4.1 at the respective interfaces in the current analysis. For the calculations

in this section, only the RTI growth factors are computed from the 1D counterparts of the 3D SN simulations. All other quantities relevant for the NiCoFe0.5X mixing such as the velocities of NiCoFe0.5X and the times at which the (outermost) part of the SN shock passes the different composition interfaces, are computed from the 3D data.

The interaction with a reverse shock can hinder the mixing of NiCoFe0.5X that is facilitated by the growth of RTIs, potentially even completely suppress such mixing (Wongwathanarat et al. 2015). As we have seen in Figs. 12 and 13, the reverse shock usually forms below the He/H interface in the expanding SN ejecta after the forward shock has entered the hydrogen envelope. Therefore it can strongly affect the transport of NiCoFe0.5X into the RT unstable region at the He/H composition interface. The strength of this influence depends on the ratio of two different timescales (Utrobin et al. 2019, 2021), namely the time it takes for the reverse shock to form and the time needed by the fastest NiCoFe0.5X to arrive at the location where the reverse shock builds up. The larger this ratio is, the more can the RTIs grow before the fastest NiCoFe0.5X is hit by the reverse shock. For large ratios the obstructive impact of the reverse shock is diminished and NiCoFe0.5X is permitted to be encompassed by the RTI at the He/H interface and thus to be carried deep into the H envelope with high velocities. Otherwise, if the timescale ratio is small, the reverse shock forms much more rapidly than the outermost NiCoFe0.5X is able to catch up, and therefore the reverse shock and the associated accumulation of dense He in its downstream region become a serious obstacle to the propagation of NiCoFe0.5X into the RT unstable region at the He/H interface. As a consequence, NiCoFe0.5X is severely slowed down and its mixing into the H envelope is weak.

The timescale in the numerator can be estimated as the time between reverse shock formation,  $t_{RS}$ , and the time when the SN shock passes a given interface

$$\Delta t_{\rm RS}^{\rm CO} = t_{\rm RS} - t_{\rm CO} \,. \tag{20}$$

$$\Delta t_{\rm RS}^{\rm He} = t_{\rm RS} - t_{\rm He} \,, \tag{21}$$

The travel time that is required by the fastest NiCoFe0.5X to reach the location of the reverse-shock formation is given by the distance to the reverse shock divided by the mass-weighted average of the fastest 4% of NiCoFe0.5X,  $v_{\text{NiCoFe0.5X}}^i$ , when the SN shock passes the respective interface (i = CO, He for the (C+O)/He and He/H interface, respectively). For example, for the C+O/He interface this distance is  $\Delta R_{\text{CO}} = R_{\text{RS}} - R_{\text{CO}/\text{He}}$ , and the time for the NiCoFe0.5X to hit the radius  $R_{\text{RS}}$  is expressed by the ratio  $\Delta R_{\text{CO}}/v_{\text{NiCoFe0.5X}}^{\text{CO}}$ .

Combining the timescale ratio,  $\Delta t_{\rm RS}^{\rm CO} \times \left(\Delta R_{\rm CO}/v_{\rm NiCoFe0.5X}^{\rm CO}\right)^{-1}$ , with the corresponding RT growth factor  $\log(\xi/\xi_0)^{\rm CO}$  and adding up the contributions from both the C+O/He and the He/H interfaces yields a dimensionless property that we denote by  $X_{\rm mix}$ :

$$X_{\text{mix}} \equiv \sum_{i=\text{CO.He}} \Delta t_{\text{RS}}^{i} \times \left(\frac{\Delta R_{i}}{v_{\text{NiCoFe0.5X}}^{i}}\right)^{-1} \times \log\left(\frac{\xi}{\xi_{0}}\right)^{i}.$$
 (22)

This quantity characterizes the impact of the growth of RTIs on the radial NiCoFe0.5X mixing in a considered 3D explosion model.<sup>2</sup>

<sup>&</sup>lt;sup>2</sup> We note that Utrobin et al. (2019, 2021) used the product of the growth factors  $\log(\xi/\xi_0)^{\text{He}} \times \log(\xi/\xi_0)^{\text{CO}}$  instead of their sum as we do here. However, the sum appears to be a natural choice based on the discussion around equation (18). Moreover, some of the RSG progenitors have very small growth factors at the (C+O)/He interface. For these models, the product would thus be unreasonably small, too. This problem did not occur in the explosion models considered in Utrobin et al. (2019, 2021), so the use of

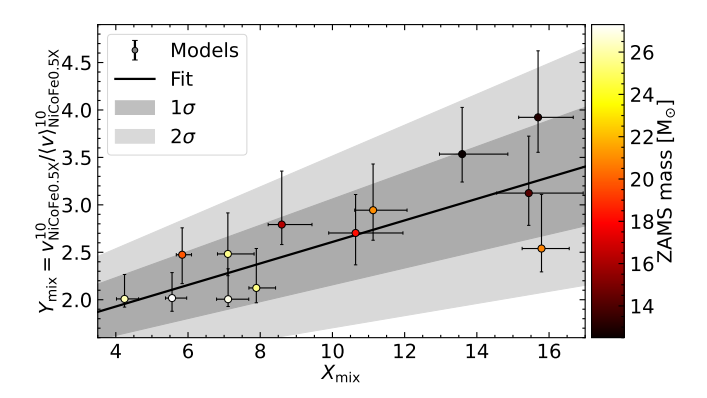


Figure 17. NiCoFe0.5X mixing parameter  $Y_{\rm mix}$  as defined in equation (23) versus characteristic RT growth parameter  $X_{\rm mix}$  as defined in equation (22) for our set of 3D explosion simulations of RSG progenitors (circles with colour coding corresponding to the ZAMS mass). The error bars reflect the uncertainty in velocity, which we estimate by considering two extreme cases for the limiting bulk mass, namely 93% and 99% of the total NiCoFe0.5X mass, respectively. The corresponding  $v_{\rm NiCoFe0.5X}^{10}$  are then calculated as the mass-weighted averages of the fastest 7% and 1% of the total NiCoFe0.5X mass. The black line denotes the least-square fit of the data points, and the shaded areas depict the  $1\sigma$  and  $2\sigma$  deviations.

Further following Utrobin et al. (2019, 2021), we estimate the computationally determined extent of NiCoFe0.5X mixing by the dimensionless ratio of the mass-weighted average velocity of the fastest 4% of NiCoFe0.5X to the mass-weighted velocity of the bulk of the remaining 96% of the mass of NiCoFe0.5X as obtained in our 3D SN explosion simulations. Different from the previous papers, we consider these velocities at  $t=10\,\mathrm{d}$  after core collapse, because at later times the energy input due to  $\beta$  decay can lead to significant late-time acceleration of the NiCoFe0.5X-rich plumes (Gabler et al. 2021). The relevant velocities are therefore denoted by  $v_{\mathrm{NiCoFe0.5X}}^{10}$  and  $\langle v \rangle_{\mathrm{NiCoFe0.5X}}^{10}$ , respectively, and their ratio defines our NiCoFe0.5X mixing parameter:

$$Y_{\text{mix}} \equiv \frac{v_{\text{NiCoFe0.5X}}^{10}}{\langle v \rangle_{\text{NiCoFe0.5X}}^{10}} \ . \tag{23}$$

As a velocity ratio, this quantity is not strongly dependent on the explosion energy.

We are now equipped with the relations that are suitable to quantify the extent of NiCoFe0.5X mixing in terms of the dependence of  $Y_{\rm mix}$  on  $X_{\rm mix}$ . Values of all quantities needed for this analysis can be found in Table 3. The results are shown in Fig. 17 for our set of RSG progenitors. We witness a linear correlation between the extent of NiCoFe0.5X mixing in the explosion ejecta and the characteristic RT growth parameter  $X_{\rm mix}$ :

$$Y_{\text{mix}} = 0.11 \times X_{\text{mix}} \,. \tag{24}$$

Fig. 17 reveals a clear separation between the different categories defined for our models, which justifies the the chosen grouping. The LM models possess the largest  $Y_{\rm mix} \gtrsim 3.0$  and  $X_{\rm mix} \gtrsim 13.5$ , the HM-LE models have  $2.4 \lesssim Y_{\rm mix} \lesssim 3.0$  and a wide spread of  $5.8 \lesssim X_{\rm mix} \lesssim 15.8$ , and the HM-HE are limited to  $Y_{\rm mix} \lesssim 2.5$  and

the product of the logarithms of the growth factors seems plausible for their case. Additionally, we refine their criterion by considering the radial distance between the shock formation position and the composition-shell interface in each term of the sum specifically instead of just using the radius  $R_{\rm RS}$ .

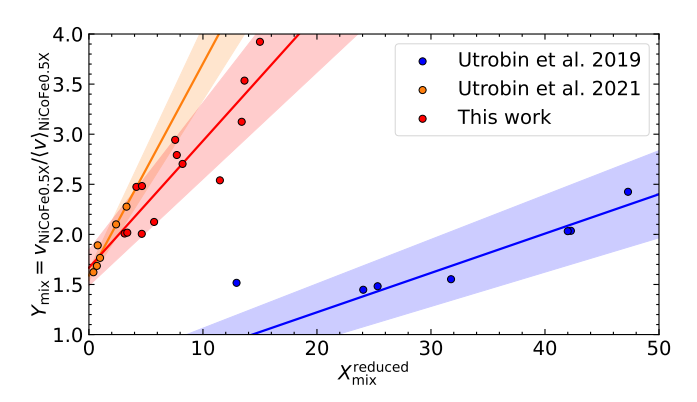


**Figure 18.** NiCoFe0.5X mixing parameter, defined as the ratio  $v_{\rm NiCoFe0.5X}/\langle v \rangle_{\rm NiCoFe0.5X}$  (measured at 10 d for our RSG explosions and at 150 d for the explosions of single-star BSG progenitors of Utrobin et al. 2019 and of binary-merger BSG progenitors of Utrobin et al. 2021), versus characteristic strength of RT mixing  $X_{\rm mix}^{\rm reduced}$  as defined in equation (25). The shaded bands indicate the  $1\,\sigma$  deviations from the least-square fits represented by the coloured solid lines.

 $X_{\rm mix} \lesssim 8.0$ . The separation in  $Y_{\rm mix}$  works perfectly well. However,  $X_{\rm mix}$  of SW20.8 lies within the corresponding values of the LM group. These deviations already indicate that the chosen parameters do not describe the properties of the different models perfectly well. The considerable deviation in  $X_{\rm mix}$  of this particular model comes from the much larger  $\Delta t_{\rm RS}^{\rm He}$  of this model compared to the other models in the HM-LE group. This is probably a consequence of the much lower explosion energy, causing a lower shock speed and thus a later formation time of the reverse shock. Nevertheless, despite its outlier role w.r.t. the value of  $X_{\rm mix}$ , also the data point of model SW20.8 is located close to the correlation line defined by equation (24).

In Fig. 18, we compare our results with those of Utrobin et al. (2021). Since not all information for their models is available to us to add them directly into our Fig. 17, we redefine the quantity plotted on the abscissa by introducing a simplified version of the characteristic RT growth parameter:

$$X_{\rm mix}^{\rm reduced} \equiv \frac{v_{\rm NiCoFe0.5X}^{\rm CO} \Delta t_{\rm RS}^{\rm CO}}{R_{\rm RS}} \times \left[ \log(\xi/\xi_0)^{\rm CO} + \log(\xi/\xi_0)^{\rm He} \right] \ . \eqno(25)$$

The values of the quantities needed to evaluate this expression could be obtained from Table 3 of Utrobin et al. (2021) and we re-evaluated our models accordingly. The form of equation (25) still differs from the product of RT growth factors considered by Utrobin et al. (2021) as explained in the discussion around equation (22). Moreover, we calculated our NiCoFe0.5X mixing parameter  $Y_{\rm mix}$  at 10 d, whereas Utrobin et al. (2021) used velocities at 150 d, which introduces another (minor) uncertainty in the comparison.

Our models cover a wider range of values,  $2.0 \lesssim Y_{\text{mix}} \lesssim 4.0$ , than the BSG explosions of Utrobin et al. (2019, 2021), which yield values up to  $Y_{\text{mix}} \lesssim 2.5$  only. The high values of  $Y_{\text{mix}}$  indicate very strong mixing in particular in our LM and HM-LE models. The 3D single-star explosions studied by Utrobin et al. (2019) (blue bullets in Fig. 18) and the 3D explosions of binary-merger progenitors investigated by Utrobin et al. (2021) (orange bullets) were based on proposed BSG stellar models for SN 1987A, and therefore quite massive. For progenitor masses  $\gtrsim 15\,\mathrm{M}_\odot$ , we obtain similarly reduced mixing in our RSG explosions, though there may be a tendency that NiCoFe0.5X mixing in explosions of RSGs is slightly more efficient than that occurring in SNe of BSGs of comparable masses. But also

24

all the generally weakly mixing BSG progenitors exceed a minimum value of  $Y_{\rm mix} \approx 1.45$ .

The characteristic mixing parameter  $X_{\rm mix}^{\rm reduced}$  reveals systematic differences between explosions of the different types of progenitors. While  $X_{\rm mix}^{\rm reduced} \lesssim 3.2$  for binary-merger progenitors (bBSGs), it adopts values in the interval  $3.1 \lesssim X_{\rm mix}^{\rm reduced} \lesssim 15$  for the RSGs, and  $X_{\rm mix}^{\rm reduced} \gtrsim 12.9$  for the single-star BSG progenitors (sBSGs). The basically non-overlapping ranges of values demonstrate that the structures of the different models are intrinsically different between the different types of CCSN progenitors.

The linear correlations indicated in Fig. 18,

$$Y_{\text{mix}} = a \times X_{\text{mix}}^{\text{reduced}}, \tag{26}$$

have slope parameters with values  $a_{\rm RSG} = 0.13$ ,  $a_{\rm sBSG} = 0.04$ , and  $a_{\rm bBSG} = 0.21$ , respectively. These differences in the correlations for the different types of progenitors are suggestive and may be linked to fundamental differences in the pre-collapse structures of the stars. However, it is presently unclear how much they depend on our simplistic way to characterize the extent of radial NiCoFe0.5X mixing in the 3D explosions due to the influence of the growth factors of RTIs at the composition-shell interfaces. It will have to be seen whether the differences between different types of progenitors will survive when a more detailed theory becomes available that is able to capture the connection between relevant structural properties and hydrodynamic effects in a more quantitative way (see also Utrobin et al. 2021).

Note that the exact value of  $a_{\rm RSG}$  obtained in our study may be affected by the chosen prescription of the dilute medium embedding the progenitor and the surrounding stellar wind that we had to assume for our 3D simulations with an Eulerian grid (see Section 2.3; in contrast to the 1D long-term models of Utrobin et al. 2019, 2021, which were computed with a Lagrangian radiation-hydrodynamics code). For more (less) massive winds, the deceleration of the ejecta in the exterior will be stronger (weaker), and in particular the fastest ejecta will become considerably slower (faster). This will reduce (increase)  $Y_{\rm mix}$ . However, this effect will be systematic for all models, for which reason our conclusions and the linear correlations obtained here should not be affected.

## 5 DEPENDENCE ON THE PROGENITOR

In the previous section, we have shown how the RTI growth factors calculated from the 1D explosion simulations as well as NiCoFe0.5X propagation velocities and the time of reverse-shock formation obtained in our 3D models can be used to characterize the mixing behaviour of <sup>56</sup>Ni in the 3D SN simulations. In the following, we aim to go one step further and connect the efficiency of <sup>56</sup>Ni mixing directly to the structure of the progenitor.

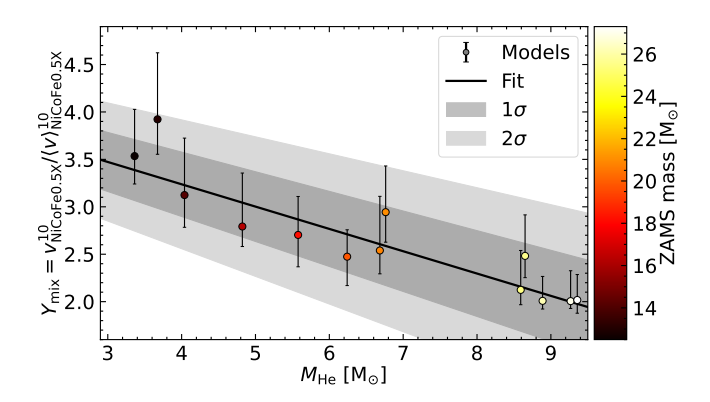


**Figure 19.** Dependence of the NiCoFe0.5X mixing in terms of  $Y_{\rm mix}$  (equation 23) on the He-core mass of the progenitor. The error bars are estimated by computing the velocities in  $Y_{\rm mix}$  with the assumption that the bulk of the NiCoFe0.5X ejecta contains 93% and 99% of the total NiCoFe0.5X mass. Colours of the circles indicate ZAMS masses according to the colour bar. The shaded areas depict the  $1\sigma$  and  $2\sigma$  deviations.

## 5.1 Dependence on the He-core mass

Utrobin et al. (2019) suggested that the extent of  $^{56}$ Ni mixing in their 3D BSG explosion simulations depends on the He-core mass. We show a corresponding plot in Fig. 19. The mixing parameter  $Y_{\rm mix}$  of our models is inversely proportional to  $M_{\rm He}^{\rm core}$  (equation 23). From the linear fit we performed, we obtain a good anti-correlation between the extent of mixing and the He-core mass with a coefficient of determination  $R_{\rm fit}^2 = 0.90$ . All models except one lie within a  $1\sigma$  band around the linear fit, as shown by the dark-grey-shaded area in Fig. 19. Without explicitly providing the plots, we also confirm previous findings that the He-core mass is better to predict the NiCoFe0.5X mixing efficiency than other progenitor properties such as the ZAMS mass or the preSN mass  $M_{\rm prog}$ . The models of our three classes, LM, HM-LE, and HM-HE, are well separated except model SW19.8, which we count to the HM-HE class despite its average He-core mass of  $6.12\,{\rm M}_{\odot}$  (Table 1).

## 5.2 Dependence on density structure

As we have seen, the He-core mass performs quite well as an indicator for the efficiency of the NiCoFe0.5X mixing in our RSG explosions. Here, we attempt to advance our understanding further by relating the mixing to progenitor properties that possess some physical relevance for the processes that determine the mixing.

In Section 4.1, we discussed the dependence of the RTI growth factors  $\xi$  on the function  $\rho r^3$ , which determines the propagation of the SN shock in the He shell and H envelope. In Fig. 6, we see that model SW13.1 is the only of the considered three representative cases that has a significant growth of RTI at the (C+O)/He-interface. It is also the only model with a pronounced maximum in the profile of  $\rho r^3$  in the He-shell. Actually, all LM models, showing the strongest mixing of all models, have such a maximum. To obtain this extremum in  $\rho r^3$ , the latter has to possess a positive density gradient before reaching the maximum. The positive gradient of  $\rho r^3$  is directly related to the deceleration of the shock wave before the maximum (Sedov 1959). Deceleration leads to a pile-up of material and, hence, to a positive pressure gradient within the exploding ejecta, while the density gradient stays negative in the same region. These are the discussed favourable conditions for the growth of RTIs.

In order to quantify how strong the gradient or how pronounced the

 $<sup>^3</sup>$  Note that in the set of sBSG models the case with the lowest value of  $X_{\rm mix}^{\rm reduced}$  is model N20 from Shigeyama & Nomoto (1990). This model did not result from a self-consistent stellar evolution computation but was artificially created by combining a preSN helium core of 6 M<sub>☉</sub> (Nomoto & Hashimoto 1988) with a hydrogen envelope computed independently by Saio et al. (1988). Both the He core and the H envelope were constructed to satisfy observational constraints from Sanduleak −69°202. For these reasons we did not take it into account in our linear fit.

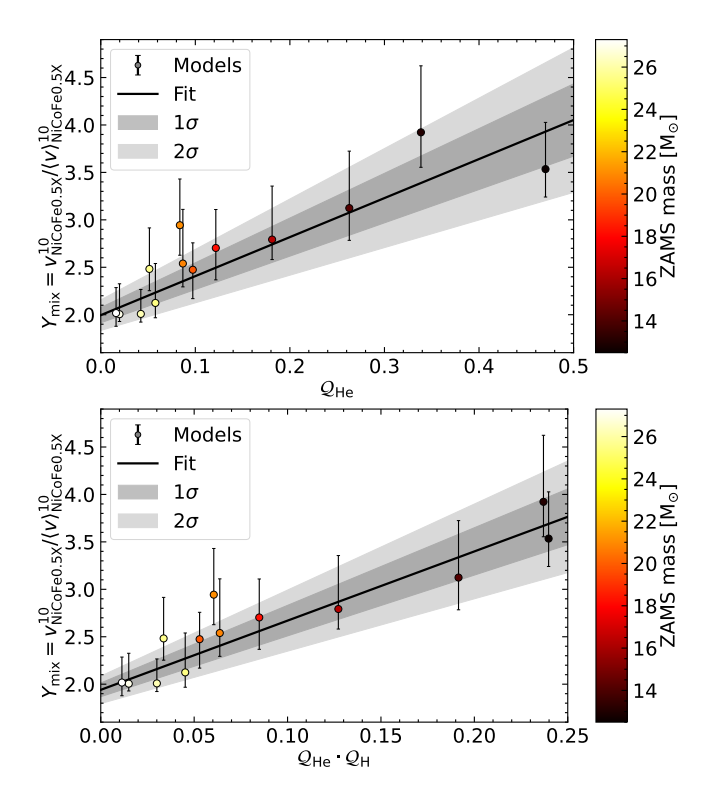


**Figure 20.** Dependence of the NiCoFe0.5X mixing measured by  $Y_{\rm mix}$  (equation 23) on the structural parameters  $Q_{\rm He}$  (top panel) and  $Q_{\rm He} \cdot Q_{\rm H}$  (bottom panel) of the RSG progenitors of our 3D SN models.  $Q_{\rm He}$  and  $Q_{\rm H}$  are computed according to equations (27) and (28), respectively. The error bars are estimated by varying  $Y_{\rm mix}$  under the assumption that the bulk of the NiCoFe0.5X ejecta contains 93% and 99% of the total NiCoFe0.5X mass. Colours of the circles indicate ZAMS masses as given by the colour bar. The shaded areas depict the 1 $\sigma$  and 2 $\sigma$  deviations.

maximum is, we define  $Q_{\rm He}$  to be the integral of  $\rho r^3$  in the He-shell of the pre-collapse star, normalized by the product of the thickness of the He-shell,  $d_{\rm He} = R_{\rm He/H} - R_{\rm CO/He}$ , and the value of  $\rho r^3$  at the (C+O)/He-shell interface,  $(\rho r^3)|_{\rm CO/He}$ :

$$Q_{\rm He} \equiv \frac{\int_{R_{\rm CO/He}}^{R_{\rm He/H}} \rho r^3 dr}{d_{\rm He} \times (\rho r^3) \Big|_{\rm CO/He}},$$
(27)

where  $R_{\rm CO/He}$  and  $R_{\rm He/H}$  are the radii of the (C+O)/He and He/H composition interfaces, respectively. The dimensionless ratio  $Q_{\rm He}$  quantifies the deviation of the function  $\rho r^3$  from a constant value of  $(\rho r^3)|_{\rm CO/He}$ , normalizing the area under the curve over the extent of the He shell. The larger  $Q_{\rm He}$  is, the higher is the maximum of  $\rho r^3$ , and the stronger the shock deceleration is expected to be. We also could have chosen properties such as the mean or the maximum gradient of  $\rho r^3$  as alternative measures. However,  $Q_{\rm He}$  has the advantage of being an integral quantity that captures the behaviour not only at a specific point, e.g., at a composition interface.

In the upper panel of Fig. 20, the extent of NiCoFe0.5X mixing in terms of  $Y_{\rm mix}$  is plotted as a function of  $Q_{\rm He}$ . There is a clear correlation between the degree of NiCoFe0.5X mixing and the structure of the progenitor star in the He shell. The linear fit has a slope of 4.15 and the values of all models, except that of the HM-LE model SW21.0, deviate from the correlation line by less than  $2\sigma$ .

So far we have only considered the He-shell structure. Analogue

to  $Q_{\rm He}$ , we define  $Q_{\rm H}$  in the H envelope as

$$Q_{\rm H} = \frac{\int_{R_{\rm He/H}}^{2R_{\rm He/H}} \rho r^3 dr}{d_{\rm H} \times (\rho r^3) \Big|_{2R_{\rm He/H}}},$$
 (28)

where we choose  $d_{\rm H}=2R_{\rm He/H}-R_{\rm He/H}=R_{\rm He/H}$ . Since the instability mainly depends on the change of the gradient close to the He/H interface, we do not integrate over the entire H envelope but set the upper integration boundary to  $r=2R_{\rm He/H}$ . Our results do not sensitively depend on the exact upper bound of the integral. In the denominator of equation (28) we take the value of  $\rho r^3$  also at  $r=2R_{\rm He/H}$ , in contrast to  $Q_{\rm He}$ , where we take it at the corresponding shell interface. With this definition both values for  $Q_{\rm He}$  and  $Q_{\rm H}$  are smaller than one. Otherwise both factors could (partially) cancel each other. The opposite behaviour is related to the different slope of  $\rho r^3$ , which, overall, is decreasing in the He shell and increasing in the H shell (see Fig. 7).

Using the product of  $Q_{\rm He}$  and  $Q_{\rm H}$  to characterize the pre-collapse stellar structure, we obtain a slightly improved correlation with  $Y_{\rm mix}$  in the lower panel of Fig. 20. The slope of the linear fit in this case is 7.28. When comparing the value of  $R_{\rm fit}^2=0.87$  for the coefficient of determination in the case of  $Q_{\rm He}$  to  $R_{\rm fit}^2=0.91$  when  $Q_{\rm He}\cdot Q_{\rm H}$  is used, we see that the inclusion of  $Q_{\rm H}$  improves the results, but the main trend is already captured by  $Q_{\rm He}$ .

In summary, the degree of NiCoFe0.5X mixing measured by the velocity ratio  $Y_{\text{mix}}$  of equation (23) exhibits a linear, negative correlation with the He-core mass (Fig. 19). In contrast, we find positive, linear correlations of  $Y_{\text{mix}}$  with  $Q_{\text{He}}$  as well as  $Q_{\text{He}} \cdot Q_{\text{H}}$  (Fig. 20). These results fortify our discussion of Section 4.1 that despite their lower explosion energies, the LM progenitors develop more intense NiCoFe0.5X mixing in 3D explosions than the investigated HM-LE and HM-HE explosions of RSG progenitors. There is a clear inverse ordering of the strength of NiCoFe0.5X mixing with the He-core mass, which increases with the ZAMS mass, whereas the explosion energy has only a secondary influence. The stronger NiCoFe0.5X mixing in the LM explosion models is explained by higher growth factors of RTI at the (C+O)/He interface due to a more pronounced local maximum of  $\rho r^3$  in the He shell of the LM progenitors (Figs. 6 and 7). The corresponding growth of RTI at the (C+O)/He interface fosters the transport of fast-moving NiCoFe0.5X from the initial asymmetries, which were created by the neutrino-heating mechanism in the first seconds, through the He shell into the ubiquitous RT unstable region near the He/H interface and thus into the H envelopes of the LM RSG explosions. In contrast, this NiCoFe0.5X mixing into the H envelope remains weak in our HM-HE explosion simulations for the highest progenitor masses. The ejecta of the HM-HE models undergo only one phase of RTI at the He/H interface and the reverse shock does not allow the NiCoFe0.5X to reach the unstable region. HM-LE models are intermediate. They have only one dominant RT phase but the reverse shock is not efficiently hindering the NiCoFe0.5X to participate in the RTI.

# 6 SUMMARY AND CONCLUSIONS

We performed long-term 3D simulations of CCSN explosions of 13 RSGs from core bounce until 10 days. The progenitors with ZAMS masses between 12.5 and 27.3  $M_{\odot}$  are a subset of the models presented by Woosley & Heger (2015) and Sukhbold & Woosley (2014), which have been exploded in 1D by Sukhbold et al. (2016). Our 3D explosions were initiated by neutrino heating using a parametric approach with neutrino luminosities and mean energies imposed at the

inner grid boundary such that we reproduced the explosion energies of the 1D SN simulations of Sukhbold et al. (2016). After 2.5 s, the explosion energies had effectively reached their terminal values in the range between 0.69 B and 1.73 B, and the corresponding <sup>56</sup>Ni yields were between  $0.059\,M_\odot$  and  $0.110\,M_\odot$ . Note that these  $^{56}Ni$ yields are our best estimates that include 50% of the mass of a socalled tracer nucleus produced in neutron-rich ( $Y_e < 0.49$ ) ejecta. Thus we account for uncertainties in the iron-group nucleosynthesis connected to our simplified neutrino transport, which tends to underestimate  $Y_e$  in the neutrino-heated ejecta. All values of the explosion energies, estimated <sup>56</sup>Ni masses, and of the NS properties (masses, kick velocities, and angular momenta) at 2.5 s are listed in Table 2. At 2.5 s we mapped our 3D explosion models onto a larger radial grid (continuing with the same angular grid) in order to carry the 3D simulations to much later times. Thus we could study the growth the RTIs at the composition-shell interfaces after the passage of the outward propagating SN shock. These hydrodynamic instabilities at the (C+O)/He and He/H shell boundaries are seeded by the initial explosion asymmetries connected to the neutrino-heating mechanism. They shape the final morphology of the heavy-element distribution in SN explosions and their remnants and determine the radial mixing of heavy elements from the innermost regions into the He shell and H envelope.

The mixing behaviour in 3D simulations is closely linked to RT growth factors as evaluated on the basis of 1D SN simulations with similar explosion energies. These growth factors depend on the radial profile of  $\rho r^3$  and typically become large at or near composition interfaces, where the radial derivative of  $\rho r^3$  changes its sign. In composition layers where  $\rho r^3$  has a positive gradient, the SN shock experiences a deceleration and favourable conditions for the growth of RTI develop in the post-shock region. While large growth factors at the He/H interface are ubiquitous, because  $\rho r^3$  generally increases in extended regions of the H envelopes of RSGs, the strength of RTI at the (C+O)/He interface depends on a local maximum of  $\rho r^3$  in the He layer. In our study we could identify three classes of RSG explosions, which revealed a systematic trend in the strength of <sup>56</sup>Ni mixing closely correlated with the progenitor mass: (a) Our lowest-mass (LM) progenitors with  $12 M_{\odot} \lesssim M_{\rm ZAMS} \lesssim 15 M_{\odot}$  and small C+O cores possess a pronounced maximum of  $\rho r^3$  in the He shell. Therefore they show large RT growth factors and strong RT mixing at both the (C+O)/He and He/H interfaces in our 3D explosion simulations. The fastest 4% of the <sup>56</sup>Ni are mixed deep into the H envelope in long-stretched RT plumes that are ejected with average velocities between 4000 km s<sup>-1</sup> and 5000 km s<sup>-1</sup>. (b) Our second group (HM-LE) of models is formed by progenitors with 15  $M_{\odot} \lesssim$  $M_{\rm ZAMS} \lesssim 21 \, M_{\odot}$  and more massive C+O cores. In the explosions of these stars the growth of RTI at the (C+O)/He interface is very weak due to only a flat maximum of  $\rho r^3$  and little shock deceleration in the He layer. But because of a wide region of high RT growth factors around the He/H interface the mixing of <sup>56</sup>Ni into the H envelope is still very efficient. The fastest 4% of the 56Ni is also ejected at the tips of very elongated RT fingers with mean velocities between roughly 3000 km s<sup>-1</sup> and 4000 km s<sup>-1</sup>. In both model classes, LM and HM-LE models, the reverse shock does not efficiently prohibit the inclusion of NiCoFe0.5X-rich ejecta in the RT growth. (c) Our third class (HM-HE) of models with  $M_{\rm ZAMS} \gtrsim 21 \, M_{\odot}$  and the most massive C+O cores does not possess any local maximum of  $\rho r^3$  in the He shell. It therefore lacks the growth of RTI at the (C+O)/He interface. As as consequence, the outermost <sup>56</sup>Ni resides far behind the reverse shock when the latter forms as the SN shock decelerates in the H envelope. This <sup>56</sup>Ni is further slowed down when it ultimately collides with the reverse shock and then gets stuck in the base of a dense He region that has built up below the H envelope. Since this He wall had time to accumulate a large mass before it was reached by the fastest  $^{56}\rm Ni$ , hardly any  $^{56}\rm Ni$  can be encompassed by the RTI at the He/H interface. The  $^{56}\rm Ni$  mixing into the H envelope remains very weak and the average velocities of the fastest 4% of the  $^{56}\rm Ni$  stay below  $\sim\!3000\,\rm km\,s^{-1}$ . Extended  $^{56}\rm Ni$ -rich fingers are therefore absent in such HM-HE explosions, and due to the strong compression by the reverse shock the overall morphology of the final  $^{56}\rm Ni$  distribution develops a less extreme asymmetry that in the LM and HM-LE explosions.

We conclude that the specific progenitor properties of the HM-HE models with very massive C+O cores and the absence of a local maximum of  $\rho r^3$  in the He shell prevent high <sup>56</sup>Ni velocities in the He layer and consequently in the H envelope, too. Despite their higher explosion energies, these models therefore exhibit much less efficient mixing of 56Ni and other heavy elements from the metal core into the outer layers than the other models, in particular also compared to the LM class with its lowest explosion energies. This implies that the explosion energy has a secondary influence on the metal mixing into RSG envelopes during SN explosions, at least within the range of values covered by our set of 3D SN models. In all of these models, however, independent of the class they belong to and despite the massive hydrogen envelope of the pre-collapse stars, the late-time morphology of the <sup>56</sup>Ni distribution reflects the spatial asymmetry of the <sup>56</sup>Ni that was imprinted by the neutrino-heating mechanism and the associated production of <sup>56</sup>Ni in neutrino-heated and shock-heated ejecta during the very first seconds of the explosion.

As described above, <sup>56</sup>Ni mixing depends on the growth factors of RTIs at the (C+O)/He and He/H composition-shell interfaces, the C+O core mass, and the reverse shock that typically forms below the He/H interface in the expanding ejecta due to the SN-shock deceleration in the H envelope. This leads to some fairly tight correlations between these explosion and progenitor properties on the one hand, and the extent of the radial  $^{56}$ Ni mixing measured by  $Y_{\text{mix}}$ of equation (23) (following Utrobin et al. 2019 and Utrobin et al. 2021, who used it for BSG explosions) on the other hand.  $Y_{\text{mix}}$  describes the spread of the velocity distribution of <sup>56</sup>Ni by means of the ratio of the average velocities of the fastest 4% and of the remaining 96% of the <sup>56</sup>Ni ejecta at the end of our 3D simulations (at 10 days). For example, we found that  $Y_{\text{mix}}$  increases roughly linearly with the characteristic RT growth parameter  $X_{\text{mix}}$  of equation (22), which accounts for the enhanced mixing due to large RTI growth factors as well as the obstructive impact of the interaction of fast <sup>56</sup>Ni with the reverse shock (Fig. 17). We thus generalized similar relations obtained by Utrobin et al. (2019) and Utrobin et al. (2021) for 3D explosions of single-star and binary-merger BSG progenitors of SN 1987A, to our set of RSG explosions (Fig. 18). Moreover, we found an inverse (linear) correlation of the  $^{56}$ Ni mixing ( $Y_{mix}$ ) with the mass of the He core in our RSGs (Fig. 19); such a relation was also reported by Utrobin et al. (2019) for their BSG explosions. This inverse correlation is not astonishing in view of the fact that <sup>56</sup>Ni mixing is reduced in our models with higher C+O core masses and therefore higher He core masses (both core masses are closely correlated, see Table 1 and Ertl et al. 2020). Finally, we quantified the well-known shock-decelerating and thus mixing-conducive influence of pronounced local maxima of  $\rho r^3$  in the He layer and H envelope of the pre-collapse RSGs by introducing dimensionless quantities  $Q_{\rm He}$  and  $Q_{\rm H}$  (equations 27 and 28, respectively) and verified positive linear correlations of the extent of the  $^{56}$ Ni mixing  $(Y_{mix})$  with  $Q_{He}$ and  $Q_{\text{He}} \cdot Q_{\text{H}}$  (Fig. 20). For all of these correlation relations of  $Y_{\text{mix}}$ with explosion and progenitor properties, we witnessed a systematic

ordering and to a large extent a clear separation of our three classes of lowest-mass, intermediate-mass, and highest-mass progenitors.

Because of the initiation of asymmetric explosions by the neutrinoheating mechanism and the preservation of significant shock asphericity during the expansion of the SN ejecta until shock breakout, we find that the breakout times of the SN shock in different directions can vary in individual RSG progenitors by up to nearly one day and by 0.1 days at least. The shortest breakout times (measured by the moment when the maximum shock radius reaches the stellar surface) are around 1.1 d and the longest breakout times are around 3 d, roughly correlated with the ZAMS masses and the radii of the progenitors. In contrast, however, we do not observe any systematic variation of the time spans  $\Delta t_{\rm sb} = t_{\rm sb,2} - t_{\rm sb,1}$  between the final and initial shock-breakout times with our three classes of explosion models, despite their substantially different mixing behaviour. This can be understood by two effects acting in opposite directions: On the one hand, the degree of shock deformation tends to be higher in models with strong <sup>56</sup>Ni mixing and with big RT plumes growing in the H envelopes, which means that the SN shocks in the LM models tend to be the most deformed ones. On the other hand, the greater radii of the HM-LE and HM-HE cases shift the shock breakout to later times and thus also stretch the intervals between initial and final shock-breakout times. However, despite similar absolute time spans  $\Delta t_{\rm sb}$ , the relative lengths of the delay,  $\Delta t_{\rm sb}\,t_{\rm sb,1}^{-1}$ , exhibit a trend of being largest in the more asymmetric models (see last column in Table 5).

Our results are of relevance for the description and interpretation of the shock breakout in RSGs and for corresponding conclusions on the progenitor radii drawn from measured shock-breakout bursts. They may also guide artificial prescriptions of <sup>56</sup>Ni mixing in 1D explosion simulations to improve the modelling of light curves, spectra and spectral-line profiles, and of the gamma-ray and X-ray emission, all of which are very sensitive to the distribution of radioactive material and to its decay-heating, which affects the rise time, peak brightness, peak duration and shape, and the tail of the SN light curves. Observations can therefore provide important information on the explosion asymmetries and the efficiency of mixing of heavy elements during the explosion. Our theoretical framework of connecting the extent of the metal mixing to structural properties (density profiles and masses) of the C+O cores and He cores of the progenitors could help understanding systematic trends in the characteristics of Type-IIP SNe. It might thus have a bearing on the use of Type-IIP SNe for determining the Hubble constant (Vogl et al. 2025). Moreover, our framework might offer new diagnostic possibilities to infer intrinsic progenitor properties at the pre-collapse stage from SN observations. Thus it might open new pathways to assess the ability of late-phase stellar evolution calculations to produce the conditions needed to explain the mixing of heavy elements detected in the SN ejecta.

In a follow-up paper, we will discuss the evolution of our models to even later times, when the  $\beta$ -decay heating by radioactive isotopes has a significant impact on the geometry of the expanding ejecta and their approach to a homologous state.

# **ACKNOWLEDGEMENTS**

BG and MG acknowledge the support through the Generalitat Valenciana via the grant CIDEGENT/2019/031, the grant PID2021-127495NB-I00 funded by MCIN/AEI/10.13039/501100011033 and by the European Union, and the Astrophysics and High Energy Physics programme of the Generalitat Valenciana ASFAE/2022/026

funded by MCIN and the European Union NextGenerationEU (PRTR-C17.I1). BG acknowledges support through the Generalitat Valenciana and the Fundo Social Europeo (FSE) via the grant BEFPI 2023 (CIBEFP/2022). HTJ is grateful for support by the German Research Foundation (DFG) through the Collaborative Research Centre "Neutrinos and Dark Matter in Astro- and Particle Physics (NDM)," Grant No. SFB-1258-283604770, and under Germany's Excellence Strategy through the Cluster of Excellence ORIGINS EXC-2094-390783311. The computations were carried out on Lluis Vives v2 cluster at the University of València.

#### DATA AVAILABILITY

The data underlying this paper will be shared upon reasonable request to the corresponding author via the Garching Core-Collapse Supernova Archive,

https://wwwmpa.mpa-garching.mpg.de/ccsnarchive.

#### REFERENCES

```
Abellán F. J., et al., 2017, ApJ, 842, L24
Alp D., et al., 2019, ApJ, 882, 22
Arcones A., Janka H. T., Scheck L., 2007, A&A, 467, 1227
Arnett W. D., 1966, Canadian Journal of Physics, 44, 2553
Arnett W. D., Bahcall J. N., Kirshner R. P., Woosley S. E., 1989a, ARA&A,
    27,629
Arnett D., Fryxell B., Müller E., 1989b, ApJ, 341, L63
Aschenbach B., Egger R., Trümper J., 1995, Nature, 373, 587
Bandiera R., 1984, A&A, 139, 368
Barbarino C., et al., 2017, MNRAS, 471, 2463
Benz W., Thielemann F.-K., 1990, ApJ, 348, L17
Bersten M. C., et al., 2018, Nature, 554, 497
Bethe H. A., 1990, Reviews of Modern Physics, 62, 801
Bethe H. A., Wilson J. R., 1985, ApJ, 295, 14
Blondin J. M., Mezzacappa A., 2006, ApJ, 642, 401
Blondin J. M., Mezzacappa A., DeMarino C., 2003, ApJ, 584, 971
Boccioli L., Vartanyan D., O'Connor E. P., Kasen D., 2025, MNRAS, 540,
Bollig R., Yadav N., Kresse D., Janka H.-T., Müller B., Heger A., 2021, ApJ,
    915, 28
Buchmann L., 1996, ApJ, 468, L127
Buellet A. C., Foglizzo T., Guilet J., Abdikamalov E., 2023, A&A, 674, A205
Buras R., Rampp M., Janka H. T., Kifonidis K., 2006, A&A, 447, 1049
Burrows A., Hayes J., Fryxell B. A., 1995, ApJ, 450, 830
Burrows A., Radice D., Vartanyan D., 2019, MNRAS, 485, 3153
Burrows A., Wang T., Vartanyan D., Coleman M. S. B., 2024a, ApJ, 963, 63
Burrows A., Wang T., Vartanyan D., 2024b, ApJ, 964, L16
Chevalier R. A., 1976, ApJ, 207, 872
Chiavassa A., Freytag B., Masseron T., Plez B., 2011, A&A, 535, A22
Chiavassa A., Kravchenko K., Goldberg J. A., 2024, Living Reviews in Com-
    putational Astrophysics, 10, 2
Cigan P., et al., 2019, ApJ, 886, 51
Colella P., Glaz H. M., 1985, Journal of Computational Physics, 59, 264
Colella P., Woodward P. R., 1984, Journal of Computational Physics, 54, 174
Coleman M. S. B., Burrows A., 2022, MNRAS, 517, 3938
Colgate S. A., White R. H., 1966, ApJ, 143, 626
Couch S. M., Wheeler J. C., Milosavljević M., 2009, ApJ, 696, 953
Couch S. M., Pooley D., Wheeler J. C., Milosavljević M., 2011, ApJ, 727,
    104
DeLaney T., et al., 2010, ApJ, 725, 2038
Dessart L., Hillier D. J., Audit E., 2017, A&A, 605, A83
```

Einfeldt B., 1988, SIAM Journal on Numerical Analysis, 25, 294

Ellinger C. I., Young P. A., Fryer C. L., Rockefeller G., 2012, ApJ, 755, 160

```
Ellinger C. I., Rockefeller G., Fryer C. L., Young P. A., Park S., 2013, arXiv
                                                                                Larsson J., et al., 2025, arXiv e-prints, arXiv:2508.03395
    e-prints, arXiv:1305.4137
                                                                               Lattimer J. M., Swesty D. F., 1991, Nuclear Phys. A, 535, 331
Ertl T., Janka H. T., Woosley S. E., Sukhbold T., Ugliano M., 2016, ApJ, 818,
                                                                               Lazendic J. S., Dewey D., Schulz N. S., Canizares C. R., 2006, ApJ, 651, 250
    124
                                                                               Lentz E. J., et al., 2015, ApJ, 807, L31
Ertl T., Woosley S. E., Sukhbold T., Janka H. T., 2020, ApJ, 890, 51
                                                                               Liou M.-S., 1996, Journal of Computational Physics, 129, 364
                                                                                Mayer M. G. F., Becker W., Predehl P., Sasaki M., Freyberg M., 2022, A&A,
Fernández R., 2010, ApJ, 725, 1563
Fesen R. A., 2001, ApJS, 133, 161
                                                                                Mayer M. G. F., Becker W., Predehl P., Sasaki M., 2023, A&A, 676, A68
Fesen R. A., Gunderson K. S., 1996, ApJ, 470, 967
Fesen R. A., et al., 2006, ApJ, 645, 283
                                                                                McCray R., 2017, in Alsabti A. W., Murdin P., eds, , Handbook of Supernovae.
Foglizzo T., 2002, A&A, 392, 353
                                                                                    Springer International Publishing AG, p. 2181, doi:10.1007/978-3-319-
Foglizzo T., Scheck L., Janka H. T., 2006, ApJ, 652, 1436
                                                                                    21846-5 96
                                                                               Melson T., Janka H.-T., Marek A., 2015a, ApJ, 801, L24
Foglizzo T., Galletti P., Scheck L., Janka H. T., 2007, ApJ, 654, 1006
Förster F., et al., 2018, Nature Astronomy, 2, 808
                                                                                Melson T., Janka H.-T., Bollig R., Hanke F., Marek A., Müller B., 2015b,
Fransson C., et al., 2024, Science, 383, 898
                                                                                    ApJ, 808, L42
Fryer C. L., Fontes C. J., Warsa J. S., Roming P. W. A., Coffing S. X., Wood
                                                                                Milisavljevic D., et al., 2024, ApJ, 965, L27
                                                                               Müller E., Steinmetz M., 1995, Computer Physics Communications, 89, 45
    S. R., 2020, ApJ, 898, 123
Fryxell B., Müller E., Arnett D., 1991, ApJ, 367, 619
                                                                                Müller E., Fryxell B., Arnett D., 1991, A&A, 251, 505
Gabler M., Wongwathanarat A., Janka H.-T., 2021, MNRAS, 502, 3264
                                                                                Müller B., Heger A., Liptai D., Cameron J. B., 2016, MNRAS, 460, 742
Garnavich P. M., Tucker B. E., Rest A., Shaya E. J., Olling R. P., Kasen D.,
                                                                                Müller B., Melson T., Heger A., Janka H.-T., 2017, MNRAS, 472, 491
    Villar A., 2016, ApJ, 820, 23
                                                                                Müller B., Gay D. W., Heger A., Tauris T. M., Sim S. A., 2018, MNRAS,
Gessner A., Janka H.-T., 2018, ApJ, 865, 61
                                                                                    479, 3675
                                                                                Müller B., et al., 2019, MNRAS, 484, 3307
Goldberg J. A., Bildsten L., Paxton B., 2019, ApJ, 879, 3
Goldberg J. A., Jiang Y.-F., Bildsten L., 2022, ApJ, 933, 164
                                                                                Nagataki S., Shimizu T. M., Sato K., 1998, ApJ, 495, 413
Greco E., et al., 2021, ApJ, 908, L45
                                                                                Nakamura K., Takiwaki T., Kuroda T., Kotake K., 2015, PASJ, 67, 107
Greco E., et al., 2022, ApJ, 931, 132
                                                                                Nakamura K., Takiwaki T., Kotake K., 2022, MNRAS, 514, 3941
Hachisu I., Matsuda T., Nomoto K., Shigeyama T., 1990, ApJ, 358, L57
                                                                                Nakamura K., Takiwaki T., Matsumoto J., Kotake K., 2025, MNRAS, 536,
Hachisu I., Matsuda T., Nomoto K., Shigeyama T., 1992, ApJ, 390, 230
                                                                                    280
Hachisu I., Matsuda T., Nomoto K., Shigeyama T., 1994, A&AS, 104, 341
                                                                                Nakar E., Poznanski D., Katz B., 2016, ApJ, 823, 127
Hammer N. J., Janka H. T., Müller E., 2010, ApJ, 714, 1371
                                                                                Nieuwenhuijzen H., de Jager C., 1990, A&A, 231, 134
Hattori F., Takabe H., Mima K., 1986, Physics of Fluids, 29, 1719
                                                                                Nomoto K., Hashimoto M., 1988, Phys. Rep., 163, 13
Herant M., Benz W., 1991, ApJ, 370, L81
                                                                                O'Connor E., Ott C. D., 2011, ApJ, 730, 70
Herant M., Benz W., 1992, ApJ, 387, 294
                                                                                Ohnishi N., Kotake K., Yamada S., 2006, ApJ, 641, 1018
Herant M., Woosley S. E., 1994, ApJ, 425, 814
                                                                                Ono M., Nagataki S., Ito H., Lee S.-H., Mao J., Hashimoto M.-a., Tolstov A.,
Holland-Ashford T., Lopez L. A., Auchettl K., Temim T., Ramirez-Ruiz E.,
                                                                                    2013, ApJ, 773, 161
    2017, ApJ, 844, 84
                                                                               Ono M., Nagataki S., Ferrand G., Takahashi K., Umeda H., Yoshida T.,
Huang F., et al., 2018, MNRAS, 475, 3959
                                                                                    Orlando S., Miceli M., 2020, ApJ, 888, 111
Hungerford A. L., Fryer C. L., Warren M. S., 2003, ApJ, 594, 390
                                                                                Ono M., Nozawa T., Nagataki S., Kozyreva A., Orlando S., Miceli M., Chen
Hungerford A. L., Fryer C. L., Rockefeller G., 2005, ApJ, 635, 487
                                                                                    K.-J., 2024, ApJS, 271, 33
Isensee K., Rudnick L., DeLaney T., Smith J. D., Rho J., Reach W. T., Kozasa
                                                                                Orlando S., Miceli M., Pumo M. L., Bocchino F., 2016, ApJ, 822, 22
    T., Gomez H., 2010, ApJ, 725, 2059
                                                                                Orlando S., et al., 2020, A&A, 636, A22
Iwamoto K., Young T. R., Nakasato N., Shigeyama T., Nomoto K., Hachisu
                                                                               Orlando S., Wongwathanarat A., Janka H. T., Miceli M., Ono M., Nagataki
    I., Saio H., 1997, ApJ, 477, 865
                                                                                    S., Bocchino F., Peres G., 2021, A&A, 645, A66
Janka H.-T., Kresse D., 2024, Ap&SS, 369, 80
                                                                                Orlando S., et al., 2022, A&A, 666, A2
Janka H. T., Müller E., 1995, ApJ, 448, L109
                                                                                Page D., Beznogov M. V., Garibay I., Lattimer J. M., Prakash M., Janka H.-T.,
Janka H. T., Müller E., 1996, A&A, 306, 167
                                                                                    2020, ApJ, 898, 125
Janka H.-T., Wongwathanarat A., Kramer M., 2022, ApJ, 926, 9
                                                                                Plewa T., Müller E., 1999, A&A, 342, 179
Joggerst C. C., Woosley S. E., Heger A., 2009, ApJ, 693, 1780
                                                                                Podsiadlowski P., 2017, in Alsabti A. W., Murdin P., eds, , Handbook of Super-
                                                                                    novae. Springer International Publishing AG, p. 635, doi:10.1007/978-3-
Joggerst C. C., Almgren A., Bell J., Heger A., Whalen D., Woosley S. E.,
    2010a, ApJ, 709, 11
                                                                                    319-21846-5_123
Joggerst C. C., Almgren A., Woosley S. E., 2010b, ApJ, 723, 353
                                                                                Powell J., Müller B., 2019, MNRAS, 487, 1178
Jones O. C., et al., 2023, ApJ, 958, 95
                                                                                Powell J., Müller B., 2020, MNRAS, 494, 4665
Kageyama A., Sato T., 2004, Geochemistry, Geophysics, Geosystems, 5,
                                                                                Rubin A., Gal-Yam A., 2017, ApJ, 848, 8
                                                                                Saio H., Nomoto K., Kato M., 1988, Nature, 334, 508
                                                                               Sandoval M. A., Hix W. R., Messer O. E. B., Lentz E. J., Harris J. A., 2021,
Kane J., Arnett D., Remington B. A., Glendinning S. G., Bazán G., Müller
    E., Fryxell B. A., Teyssier R., 2000, ApJ, 528, 989
                                                                                    ApJ, 921, 113
Katsuda S., et al., 2018, ApJ, 856, 18
                                                                                Scheck L., Kifonidis K., Janka H. T., Müller E., 2006, A&A, 457, 963
Kifonidis K., Plewa T., Janka H. T., Müller E., 2003, A&A, 408, 621
                                                                                Scheck L., Janka H. T., Foglizzo T., Kifonidis K., 2008, A&A, 477, 931
Kifonidis K., Plewa T., Scheck L., Janka H. T., Müller E., 2006, A&A, 453,
                                                                               Sedov L. I., 1959, Similarity and Dimensional Methods in Mechanics. Aca-
                                                                                    demic Press
                                                                                Shigeyama T., Nomoto K., 1990, ApJ, 360, 242
Kozyreva A., Nakar E., Waldman R., Blinnikov S., Baklanov P., 2020, MN-
    RAS, 494, 3927
                                                                                Singh A., et al., 2019, ApJ, 882, L15
                                                                               Sinnott B., Welch D. L., Rest A., Sutherland P. G., Bergmann M., 2013, ApJ,
Kozyreva A., Janka H.-T., Kresse D., Taubenberger S., Baklanov P., 2022,
    MNRAS, 514, 4173
Kuroda T., Kotake K., Takiwaki T., 2012, ApJ, 755, 11
                                                                                Soumagnac M. T., et al., 2019, ApJ, 872, 141
Larsson J., et al., 2016, ApJ, 833, 147
                                                                                Stockinger G., et al., 2020, MNRAS, 496, 2039
Larsson J., Sollerman J., Lyman J. D., Spyromilio J., Tenhu L., Fransson C.,
                                                                               Sukhbold T., Woosley S. E., 2014, ApJ, 783, 10
    Lundqvist P., 2021, ApJ, 922, 265
                                                                               Sukhbold T., Ertl T., Woosley S. E., Brown J. M., Janka H. T., 2016, ApJ,
```

821, 38

Larsson J., et al., 2023, ApJ, 949, L27

```
Takiwaki T., Kotake K., Suwa Y., 2014, ApJ, 786, 83
Timmes F. X., Swesty F. D., 2000, ApJS, 126, 501
Ugliano M., Janka H.-T., Marek A., Arcones A., 2012, ApJ, 757, 69
Utrobin V. P., Wongwathanarat A., Janka H. T., Müller E., 2015, A&A, 581,
Utrobin V. P., Wongwathanarat A., Janka H. T., Müller E., 2017, ApJ, 846,
Utrobin V. P., Wongwathanarat A., Janka H. T., Müller E., Ertl T., Woosley
    S. E., 2019, A&A, 624, A116
Utrobin V. P., Wongwathanarat A., Janka H. T., Müller E., Ertl T., Menon A.,
    Heger A., 2021, ApJ, 914, 4
Vartanyan D., Coleman M. S. B., Burrows A., 2022, MNRAS, 510, 4689
Vartanyan D., Tsang B. T. H., Kasen D., Burrows A., Wang T., Teryoshin L.,
    2025a, ApJ, 982, 9
Vartanyan D., Burrows A., Teryoshin L., Wang T., Kasen D., Tsang B.,
    Coleman M. S. B., 2025b, arXiv e-prints, arXiv:2509.16314
Vink J., 2012, A&ARv, 20, 49
Vink J., 2017, in Alsabti A. W., Murdin P., eds, , Handbook of Supernovae.
    Springer International Publishing AG, p. 2063, doi:10.1007/978-3-319-
    21846-5 92
Vogl C., et al., 2025, A&A, 702, A41
Wang T., Vartanyan D., Burrows A., Coleman M. S. B., 2022, MNRAS, 517,
    543
Weaver T. A., Zimmerman G. B., Woosley S. E., 1978, ApJ, 225, 1021
Wellstein S., Langer N., 1999, A&A, 350, 148
Wongwathanarat A., 2019, ApJ, 875, 118
Wongwathanarat A., Janka H.-T., Müller E., 2010, ApJ, 725, L106
Wongwathanarat A., Janka H.-T., Müller E., 2013, ApJ, 552, A126
Wongwathanarat A., Müller E., Janka H. T., 2015, A&A, 577, A48
Wongwathanarat A., Janka H.-T., Müller E., Pllumbi E., Wanajo S., 2017,
    ApJ, 842, 13
Woosley S. E., Heger A., 2015, ApJ, 810, 34
Woosley S. E., Heger A., Weaver T. A., 2002, Reviews of Modern Physics,
Xiang D., et al., 2019, ApJ, 871, 176
Yamada S., Sato K., 1990, ApJ, 358, L9
van Baal B. F. A., Jerkstrand A., Wongwathanarat A., Janka H.-T., 2023,
    MNRAS, 523, 954
van Baal B. F. A., Jerkstrand A., Wongwathanarat A., Janka H.-T., 2024,
    MNRAS, 532, 4106
```

This paper has been typeset from a TEX/LATEX file prepared by the author.